INFRARED SENSOR SYSTEMS FOR DRONE AND AVIATION BASED IMAGING APPLICATIONS

by

Patrick Leslie

_____

A Dissertation Submitted to the Faculty of the

JAMES C. WYANT COLLEGE OF OPTICAL SCIENCES

In Partial Fulfillment of the Requirements

For the Degree of

DOCTOR OF PHILOSOPHY

WITH A MAJOR IN OPTICAL SCIENCES

In the Graduate College

THE UNIVERSITY OF ARIZONA

2024

THE UNIVERSITY OF ARIZONA
GRADUATE COLLEGE

As members of the Dissertation Committee, we certify that we have read the dissertation prepared by Patrick Scott Leslie, titled *Infrared Sensor Systems for Drone and Aviation Based Imaging Applications* and recommend that it be accepted as fulfilling the dissertation requirement for the Degree of Doctor of Philosophy.

_____   Date: 3/21/24
[Committee Chair Name]

_____   Date: 3/21/24
[Committee Member Name]

_____   Date: 3/21/24
[Committee Member Name]

Final approval and acceptance of this dissertation is contingent upon the candidate's submission of the final copies of the dissertation to the Graduate College.

I hereby certify that I have read this dissertation prepared under my direction and recommend that it be accepted as fulfilling the dissertation requirement.

_____   Date: 3/21/24
[Committee Chair Name]
Dissertation Committee Chair
[Academic Department]

ACKNOWLEDGEMENTS

To start, I would like to thank Dr. Ronald Driggers for his continued support, guidance, inspiration, and trusted independence at the University of Arizona. Thank you for taking me in as a master's student and recognizing my potential as a doctoral student. It has been an honor to study under you. To Dr. Brady and Dr. Chalifoux, the time and effort as committee members dissertation will always be appreciated and I look forward to working with you both in future endeavors.

To my family, thank you for continuing to be there for me during these past four years. The constant love and support kept me going when things got tough. Mom, thank you for always putting a smile on my face with random calls and texts of love. Dad, thank you for commiserating about the misfortunes of graduate school and celebrating the triumphs. Steven, thank you for the goofy visits, the adventures, showing me how much more there is to life, and inspiring me to travel even when I shouldn't. Becca, your ability to keep my head level, give me guidance, and reassurance in my life decisions have been indispensable. Chad, our talks about life and visits that have reinvigorate me kept me refreshed and willing to keep going in life and in school. Morgan, my sweets, the serendipitous alignment of our lives came at the perfect moment in time. Our mesquite trees at the base of Picacho peak will grow tall with strong founding roots and ornamental poppy's will bloom all around us. Onyx, my little sweets, and Jasper, my tiny sweets, you keep the love in my heart, a smile on my face and the warmth on my lap.

To my friends and chosen family. The laughs, fun nights out, dance parties, adventures, coffee dates, brewery's, di games, pool parties, rooftop cigars & whiskey, hikes, bus adventures, volleyball games, game nights, lunches, disc golf games, road trips, camping trips, roller skating, pool basketball, regular basketball games, lazy days, concerts, card games, and long conversations will always be cherished and remembered.

To my colleagues from the Infrared Group. I have enjoyed my time working with you all. The camaraderie, support, and fun that our group has is unmatched by any other group that I have been apart of. I look forward to our continued friendships and collaborations for years to come.

To Casa Video and Espresso Art Café, thank you for housing me while this document was written.

LAND ACKNOWLEDGEMENT

The work contained in this dissertation was conducted on the land and territories of Indigenous peoples. Today, Arizona is home to 22 federally recognized tribes, and an unknown number of tribes which remain federally unrecognized. Tucson and the University of Arizona exist on the land of the Tohono O'odham and the Yaqui. In addition, field work in New Mexico took place on the land of the Comanche, Jicarilla Apache, Jumanos, Kiowa, Mescalero Apache, and Pueblos peoples.

As a person whose work has benefited both from the University of Arizona Land-Grant Institution and field work in the Southwest, I recognize that these efforts were done on land which was stolen from Indigenous peoples who have cared for and inhabited these spaces in perpetuity. It is my hope and must be our sincere and collective action to prioritize reflection on this history of displacement and wrongdoing, and the enduring legacy of Indigenous peoples – past, present, and future.

DEDICATION

to Onyx, my little sweets. From the tundra to the desert, you've reminded me what's important in life - the silliness, the snuggles, the chases, the owl, and the circles.

Meow meow meow, meow meow.

TABLE OF CONTENTS

LIST OF FIGURES

12

LIST OF TABLES

LIST OF SYMBOLS

μm	Microns
M	Emittance
λ	Wavelength
T	Temperature
K	Kelvin
C	Celsius
W	Watt
s	seconds
μs	microseconds
ms	milliseconds
min	minutes
h	hours
nm	nanometer
mm	millimeter
cm	centimeter
m	meter
km	kilometer
ε	Emissivity
c_1	Physical Constant 1. Equal to 3.7418x10^4 [W-μm^4/cm^2]
c_2	Physical Constant 2. Equal to 1.4388 x 10^4 [μm-K]
E	Irradiance
$\%Ref(\lambda)$	Percent Reflective
$\%Emit(\lambda)$	Percent Emissive
λ_{peak}	Peak wavelength
$\rho(\lambda)$	Reflectivity
$\tau(\lambda)$	Transmissivity
$\alpha(\lambda)$	Absorptance
$L(r,\lambda)$	Radiance

cyc/px	cycles per pixel
x	horizontal spatial units
y	vertical spatial units
z	elevation spatial units
ξ	frequency in the x-direction
η	frequency in the y-direction
$\mathcal{F}$	Fourier Transform
$i(x, y)$	spatial 2D image
$I(\xi, \eta)$	2D fourier transform of image
$PSD(\xi, \eta)$	2D power spectral density
$A(v)$	Averaged amplitude of 1D PSD
$\frac{d}{du}$	derivative with respect to u
$\Delta\mu$	difference between average target and average background signals
σ_{tgt}	standard deviation of the target
μ_{scene}	average background signal of the scene
A	area of a target
R	Range
V	V Number
V_{50}	V-50 number
d	detector pitch
f	focal length
$^{\circ}$	degrees
α	azimuthal angle with respect to the wire facet
L	length of the wire
θ	angle of face of the wire
A_{EFF}	effective wire area
I_{REF}	intensity of wire
sr	steradian
Σ	summation

L_{BBWire}	blackbody equivalent temperature of the wire
L_{ATM}	blackbody equivalent temperature of the atmosphere
I_{TOT}	total wire intensity
π	pi
β	specular BRDF contribution
P_{pixel}	power on a single detector
$A_{aperture}$	Area of aperture
N_{det}	Number of detectors
FOV_{TOT}	Total FOV for WAC systems
SW_{TOT}	Total ground covered for WAC systems
v	velocity
$L_{Hum}(r,\lambda,\rho,T)$	Radiance from a human
$L_{rh}(r,\lambda,\rho)$	reflective radiance from a human
$L_{eh}(r,\lambda,T)$	emitted radiance from a human
E_{solar}	Solar Irradiance
ρ_{surf}	Surface reflectivity
$CL(r)$	Concentration Length
$-\alpha(\lambda)$	Extinction Coefficient
$\tau_{smk}(r,\lambda)$	Smoke Transmission
$L_{rs}(r,\lambda)$	Reflected Smoke Radiance
$L_{es}(r,\lambda,T)$	Emitted Smoke Radiance
$L_{ap}(r,\lambda,\tau,\theta)$	Total Radiance on an aperture
$\rho_{Smk}(\lambda)$	Equivalent Reflectivity of smoke
RTBB	Room temperature blackbodies
HTBB	High Temperature blackbodies
C	Contrast
W	White target or hot blackbody
B	Black target of cold blackbody
A_{det}	Area of a detector

Ω_{sensor}	Sensors aperture solid angle
$I(T,\lambda)$	Intensity
N	electrons
N_{sat}	Number of well saturation electrons
t_{int}	integration time
h	plank's constant
c	speed of light
$\%WF$	percent well fill
C_{px}	Contrast on a per pixel bases
$\sigma_{C_{avg}}$	Standard Deviation of average contrast
C_{Spk}	Speckle Contrast equation

ACRONYMS

SWaP	Size Weight and Power
IR	Infrared
EO	Electro-optical
TTP	Targeting Task Performance
UV	Ultraviolet
VIS	Visible
NIR	Near-infrared
SWIR	Shortwave-infrared
eSWIR	extended shortwave infrared
MWIR	midwave infrared
LWIR	longwave infrared
SNR	Signal to noise ratio
HOT	High Operating Temperature
MCT	mercury, cadmium, telluride
sUAS	small unmanned aerial system
PoT	pixels on target
DVE	degraded visual environment
FOV	field of view
HFOV	horizontal field of view
VFOV	vertical field of view
NFOV	narrow field of view
NNFOV	narrow narrow field of view
WFOV	wide field of view
EFL	effective focal length
MODTRAN	Moderate Resolution Atmospheric Transmission model
BBEQ	blackbody equivalent
BRDF	Bidirectional Reflecitvty Distribution Function
MTF	Modulation Transfer Function

PSF	Point Spread Function
ROI	Region of Interest
ESF	Edge Spread Function
LSF	Line Spread Function
CTF	Contrast Threshold Function
CTF_{eye}	Contrast Threshold Function of the eye
CTF_{sys}	Contrast Threshold Function of the system
P(det)	Probability of detection
P(rec)	Probability of recognition
P(ID)	Probability of identification
P(task)	Probability of task
P(disc)	Probability of discrimination
NF	Noise Floor
C_{tgt}	Target Contrast
NETD	Noise equivalent temperature difference
F/#	F-number
OD	Optical Density
NVIPM	Night Vision Integrated Performance Model
IFOV	Instantaneous field of view
PSD	Power Spectral Density
UAV	unmanned aerial vehicle
IRST	infrared search and track
QE	Quantum efficiency
GSD	ground sample distance
Mrad	milliradians
ER	equivalent reflectivity
EMCCD	electron multiplying charge-coupled devices
UCIR	uncooled infrared
DPR	Device Pixel Ratio
LoS	Line of Sight

WAC	Wide Area Coverage
FoM	Figure of Merit
GSD_{Max}	Maximum GSD
SW	Swath Width
Alt	Altitude
CMOS	Complementary Metal-Oxide-Semiconductor
FAA	Federal Aviation Administration
BRSF	Bidirectional Scattering Distribution Function
CLAHE	Contrast Limited Adaptive Histogram Equalization
SITF	system intensity transfer function
STD	Standard Deviation
US	United States
AZ	Arizona
FL	Florida
TN	Tennessee

Abstract

Designing infrared system aids commercial and military users for a plethora of applications. As the size, weight, and power (SWaP) of broadband infrared imagers decreases, their utility is exploited for aerial vehicles. Airborne systems have greater mobility and enhance the capabilities of a user when obtaining imagery. The research presented here takes radiometrically produced theoretical models and applies ground-based design techniques to the air. Pilotage, targeting, mapping, and situational awareness are all examples of infrared imaging tasks with extensive design history. The research presented focuses on designing aerial systems in these categories.

A pilotage based infrared system is designed to compare the midwave and longwave infrared (IR) bands for high-voltage wires detection to avoid deadly crashes. A new targeting system implemented a novel multi-camera design approach rooted in the targeting task performance (TTP) metric to increase performance over large areas when flown on a drone platform. Calibrated imagery from the visible, near IR, shortwave IR, and extended shortwave IR are compared to find which has the highest scene contrast for mapping tasks. Lastly, a situational awareness system is designed to keep forest firefighters safe in extreme wildfire conditions by exploiting wavelength to maintain line of sight on personnel, while mapping the fire boundary in real time to avoid fatal accidents.

For the pilotage, targeting, mapping and situational awareness system designs above, the theoretical models produced are compared to laboratory and field measurements. The calibrated analysis presented provides techniques to avoid biased results and fairly compare the performance of each broadband sensor system. In each case, the theory and measurement results

prove that the design methods are valid to create aerial sensor systems. In each case, the sensor

performance is shown to meet the design requirements and a deployable system can be created

from these initial studies.

Chapter 1: Introduction to Infrared Systems and Airborne Platforms

Aviation systems have become an integral part of our daily lives. Aircrafts appear in many shapes in sizes, from recreational drones to advanced military fighter jets. Hobbyist and trained pilots alike utilize sensor systems to complete their missions successfully. Small quadcopter's visible sensor systems are designed to capture high resolution images from an aerial perspective. High-end emissive infrared sensors are designed to aid an Apache rotorcraft pilot for rigorous night-time flight capabilities [1]. The addition of sensor systems to any airborne platform gives the user an advantage over those without them. The design of these systems to meet performance specifications is no menial task and the obstacle of flying these imagers creates even more challenges. Nevertheless, the rapid development of airborne platforms alongside state-of-the-art infrared sensors generates endless opportunities to enhance both technologies.

The benefits of each imaging band are still being explored. The materials needed to create functional detectors have not been commercially developed in some imaging bands until recently. Ultraviolet (UV, < 0.4μm), visible (VIS, 0.4-0.7μm), near-infrared (NIR, 0.7-1.0μm), and longwave infrared (LWIR 8-14μm) staring arrays have been around since the mid to late-1900's [2]. This early feat has led to the quick advancement of these focal plane technologies and their applications. Imagers in these bands have become a ubiquitous part of our everyday lives, such as the high-resolution cameras in smart phones. More recently the shortwave infrared (SWIR, 1.0-1.7μm) and midwave infrared (MWIR 3-5μm) detectors have been proliferating in the field of infrared imaging, with recent developments significantly reducing the size, weight, and power (SWaP) of SWIR and MWIR imagers. In their early stages, the focal plane materials that were responsive in these bands needed to be cooled to very low temperatures to obtain good

signal to noise ratio (SNR) [2]. With modern sensors, SWIR detectors no longer need to be cooled [3], and High Operating Temperature (HOT) MWIR detectors require much less energy and power [4]. These advancements have increased research into SWIR and MWIR imagers, and to their deployment in lower SWaP applications such as airborne systems.

Very recently, the development of extended shortwave-infrared (eSWIR 2.0-2.5µm) focal plane technologies has vastly improved the imaging in this band. Certain sensors in the past have had a response in this band, such as MCT (mercury, cadmium, telluride) detectors, but they usually had poor SNR in the 2.0-2.5µm region. The development of Type-II Superlattice and newer MCT alloys has resulted in greatly increased detector responsivity in the eSWIR. This band, which has a great transmission window in the atmosphere, has now become worth studying [5,6]. Much like the other sensors systems, the SWaP of eSWIR systems has been coming down rapidly as well [7]. The imaging systems for all these bands can now be used in lightweight use cases such as small unmanned aerial system (sUAS) sensors. Drones are a low-cost, versatile platform capable of obtaining imagery from places not normally explored. They can be sent into dangerous situations, such as forest fires or combat zones, to obtain important data without putting people in harm's way. With these factors, every imaging band can now be flown on small platforms to gather data, allowing system engineers to choose the band with the best performance for the task at hand without worrying about payload constrictions.

When taking sensors to the air, traditional ground-based design methods need to be altered. Aviation sensor systems are designed for two very general categories, targeting and mapping. A targeting sensor is developed to detect, recognize, or identify an object of interest and the probability that these tasks are completed varies with range. Traditionally, these systems are designed to perform in a specific scenario. An example system would use their imagery to

recognize the difference between a truck and a tank with high probability. For targeting, a background with little variation or "clutter" helps the user find the objects that they are looking for. Conversely, mapping systems need scenes with good contrast, many objects, and enough resolution to help orient the user. Whether a person is looking at a live stream video stream or an algorithm is finding objects of interest within the imagery, both need to identify landmarks to align themselves in the physical world.

For both targeting and mapping systems, the performance increases with resolution, or more generally, the number of pixels on target (PoT) with area covered. Making broadband and large format focal plane sensors preferable over other systems. Some applications require finer spectral resolution to identify very specific objects such as minerals in the ground. In this case a hyperspectral sensor can be used [8]. Unfortunately, most lightweight hyperspectral sensors use one axis of a 2D focal plane for spatial measurements and the other axis for spectral content [8]. This limitation requires the sensor to scan over an area to obtain full 2D imagery and rigorous algorithms align the imagery just to present the data. Both the time delay of scanning and digital registration issues of creating a 2D image present even more problems for aerial imagery. Single narrow bandpass filters can be used over a 2D focal plane but depending on the light present, the SNR can limit the sensors performance. The spectral information contained in the broader spectral bands of VIS, NIR, SWIR, eSWIR, MWIR and LWIR are enough to perform a task with high probabilities of success in a timely manner. The cost and SWaP associated with the broadband systems are also generally much lower making them easier to integrate to small drone platforms.

For most targeting and mapping applications, any of the broad spectral bands will suffice. The choice of band, however, is dependent on its use. If the system needs to be flown at night,

the MWIR and LWIR allow the user to fly without active illumination. If the system is daytime use only, the spectral variations in the VIS, NIR, SWIR and eSWIR could provide better performance than the MWIR and LWIR. For the reflective bands, the differences in the VIS, NIR, SWIR and eSWIR give each a unique advantage. One example is the longer wavelength bands tend to penetrate good visibility and degraded visual environment (DVE) conditions better than the shorter ones [6]. With the eSWIR and SWIR still being newer to the aviation industry, the performance of these two compared to the VIS and NIR systems that are flown need to be compared for both targeting and mapping applications.

Another current debate between bands is using MWIR versus LWIR for pilotage applications. These systems are generally flown on military aircrafts making nighttime flights a significant portion of their operations. Pilotage is the use of a sensor system to aid a pilot in navigating an aircraft. The system design intersects somewhere in between targeting and mapping. The pilot needs to identify known structures in their surroundings to help them negotiate the terrain effectively. There is a trade-off for choosing a MWIR or LWIR for this system. The MWIR has higher reflectivity during daytime conditions giving objects more contrast and its shorter wavelengths keeps the system from approaching the diffraction limit for the same aperture size as the LWIR. The LWIR however has many more photons available due to Plank's curve [9] and cheaper and lighter uncooled systems can be used. These are just a few examples of the extensive study between these two bands for this application.

To design MWIR or LWIR pilotage systems, the targeting task performance (TTP) metric can be used [10]. This metric allows the direct comparison between the MWIR and LWIR systems in terms of scene contrast to quantify how well a pilot could navigate with these sensors. As one would expect, the higher the contrast, the easier navigation would be. For reliable

systems, even though the MWIR outperforms the LWIR in terms of scene contrast during the day, the LWIR maintains good contrast during nighttime, cloudy, and degraded visual environment conditions [11]. An option to obtain the best of both sensors is to choose MWIR and LWIR on a dual-band focal plane [12]. Then the benefits from both wavelengths can be utilized.

For pilotage systems a LWIR, MWIR or dual-band focal plane could potentially aid in one of the deadliest crashes for rotorcrafts. Commercial and military alike, due to their flight paths, are prone to colliding with high-voltage power lines. Unfortunately, even with the vast amount of readily available technology, this incident still occurs today [13,14]. The addition of one of these systems as a passive wire-detection system could greatly benefit both sectors. The difficulty in wire detection is not only the small diameter of the wire but its rapidly changing signal due to specular reflections of the metal wire and the differences in background path radiance in the MWIR and LWIR. While the TTP metric is acceptable as a pilotage metric, it is not capable of predicting this extreme situation of wire detection on its own. Another solution is needed to compare the MWIR and LWIR to see if a dual-band system would also increase the probability of wire detection to avoid deadly crashes.

The conventional method of the TTP is to use it for the targeting of specific objects of interest [15]. The TTP metric works for all the band previously mentioned. The three typical tiers of sensor design for targeting are detection, recognition, and identification. A detection task example would be finding a signature of something in a field that doesn't seem to belong. A recognition task would be discriminating that the detected signature is a truck instead of a tractor. Lastly, the identification task for this same example would being able to distinguish that the truck was a Ford Ranger instead of a Toyota Tacoma. The TTP metric gives a probability of each of these three tasks versus range and increases in difficulty from detection to identification. Each

infrared band has their own advantages and the probability versus range curve can be compared to create the best system for its targeting task.

Older targeting systems generally have both a detection and identification optical path. The wider field of view (FOV) detects objects of interest and when a detection is made, the optical path is switched to the smaller FOV so the object can be identified [16]. The original solution to switching optics was to put a narrower FOV sensor in a gimbal to quickly scan an area with finer resolution. This adds substantial time to the detection process just like switching between optics with two FOVs. With the SWaP and cost of sensors substantially decreasing, systems are no longer confined to a using a single sensor. The imagery from multiple, high-resolution systems can be stitched together to provide a large FOV for both tasks. By using these high-resolution multi-camera systems on drone platforms, targeting tasks can cover the areas of interest even faster. The TTP metric can be modified to use multi-camera systems from a drone platform. With this method, the probability of a targeting task increases in area per time over a single sensor. Similarly, as before, the performance of the different bands of the multi-camera systems can be compared to determine which has the best opportunities for completing daytime and or nighttime targeting tasks with multi-camera systems.

The comparison of the VIS, NIR, SWIR, eSWIR, MWIR and LWIR bands needs to be thoroughly studied for all applications. Based on the signals available within the scene one band might vastly outperform the others. Outside of clear-sky and ambient illumination conditions, the abnormal signals throughout a scene can greatly change what an imager sees [17]. A system that was not designed for all conditions but utilized in them can underperform and leave the user with no recognizable imagery. Situational awareness systems are similar to pilotage systems where they give a person more information about a scene that they can achieve on their own [18]. These

systems enhance mobility and safety of people, especially when experiencing DVE conditions. The infrared wavelengths can provide an advantage over VIS sensors and human vision, if designed properly.

One advantage that the longer infrared wavelengths have is the ability to see through particles in the air that the VIS cannot [19]. A DVE condition that is constantly affecting the U.S. and the world due to climate change is wildfire smoke. A benefit that the broad band longer infrared imagers provide is the ability to see through smoke particles [20]. For a situational awareness system, the ability to observe your surroundings while there is no visibility in the VIS band is a huge advantage. A system flown on an aerial platform could aid firefighters deployed to house fires or wildfires to keep them safe. While firefighters are entering burning homes or controlling the burn in the forest, the unpredictable conditions can quickly put them in danger. By monitoring the boundary of the hot spots of the fire in real-time, the information can be relayed to the firefighters to keep them safe. The mobility of a small drone in this environment would enhance the safety of a deployment without putting a person in harm's way. However, as mentioned before, just because the longer infrared wavelengths are not scattered by the smoke particles doesn't mean that other adverse signals do not arise. Cold smoke of this particle size does not pose a threat to longer infrared wavelengths, but hot temperatures of fire and smoke emit blackbody radiation and can adversely affect the performance of a situational awareness system.

For each case above, the low SWaP and cost of infrared sensors provides a new opportunity for novel systems to be created. Mapping, pilotage, targeting and situational awareness systems can be flown on sUAS or larger platforms to greatly improve the capabilities of each task. The design of airborne infrared sensor systems needs to consider both the aerial

platform as well as the complex airborne imaging tasks presented. By using ground-based design methods such as the TTP metric and modifying them for airborne platforms, innovative solutions can advance both technologies. The combination of infrared sensor systems and airborne platforms generates new opportunities to increase the safety and efficacy of those who use them.

Chapter 2: A General Background of Infrared Imaging

2.1) Definition of Infrared Bands and Their Typical Sources

In general, broadband imaging systems are categorized by different detector material responses and atmospheric windows. The main bands are ultraviolet (UV, < 0.4μm), visible (VIS, 0.4-0.7μm), near-infrared (NIR, 0.7-1.0μm), shortwave infrared (SWIR, 1.0-1.7μm), extended-shortwave infrared (eSWIR, 2.0-2.5μm), midwave infrared (MWIR, 3.0-5.0μm) and longwave infrared (LWIR, 8-14μm). An example of the atmospheric windows during good visibility conditions is provided by a standard Moderate Resolution Atmospheric Transmission (MODTRAN®) model (Figures 2.1 & 2.2) [1]. While some stronger absorption lines still exist in these regions, the transmission windows offer opportunities for remote sensing and imaging. Atmospheric transmission across a broad range of wavelengths allows for band-specific transmission and reflectivity characteristics to be exploited.
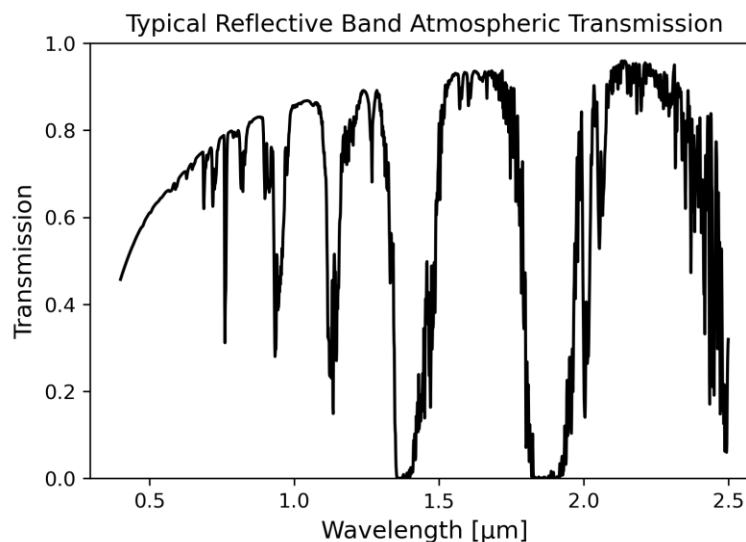
Figure 2.1: Atmospheric transmission containing the VIS, NIR, SWIR and eSWIR bands. MODTRAN6® U.S. Standard Atmosphere Transmission from 0.4-2.5μm for a 1Km horizonal path length.
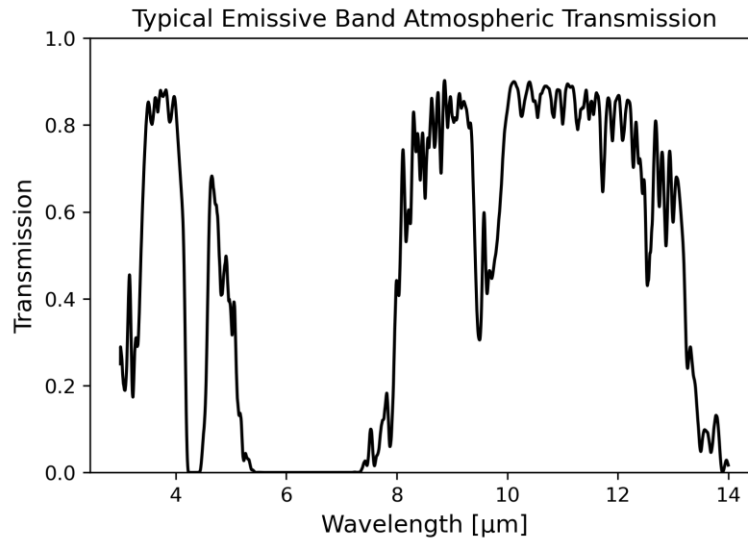
Figure 2.2: Atmospheric transmission containing the MWIR and LWIR bands. MODTRAN6® U.S. Standard Atmosphere Transmission from 3-14μm for a 1Km horizonal path length.

The VIS, NIR, SWIR and eSWIR are known as reflective bands and rely mostly on solar illumination reflected off objects for passive daytime imaging (Figure 2.3). The MWIR and LWIR are named emissive bands because most of their light comes from emitted blackbody radiation (Figure 2.4). For a daytime solar illuminated scene with clear skies, the average blackbody equivalent (BBEQ) temperature is approximately 300K. The divide of reflective and emissive bands is generally a good assumption under this condition. This assumption is referred to as ambient illumination throughout these studies. The spectral emittance of blackbody radiation is defined from Plank's blackbody radiation equation [2].

$$M(\lambda, T) = \varepsilon(\lambda) \frac{c_1}{\lambda^5} \frac{1}{[e^{\frac{c_2}{\lambda T}} - 1]} \tag{2.1}$$

Where M is spectral emittance [W/cm^2 – μm], λ is the wavelength [μm], T is the absolute temperature in Kelvin [K], $\varepsilon(\lambda)$ is spectral emissivity [unitless], $c_1 = 3.7418 \times 10^4$ [W-μm^4/cm^2],

and c_2 is [1.4388 x 10^4 μm-K]. c_1 and c_2 are composed of expressions involving physical

constants that have been simplified.
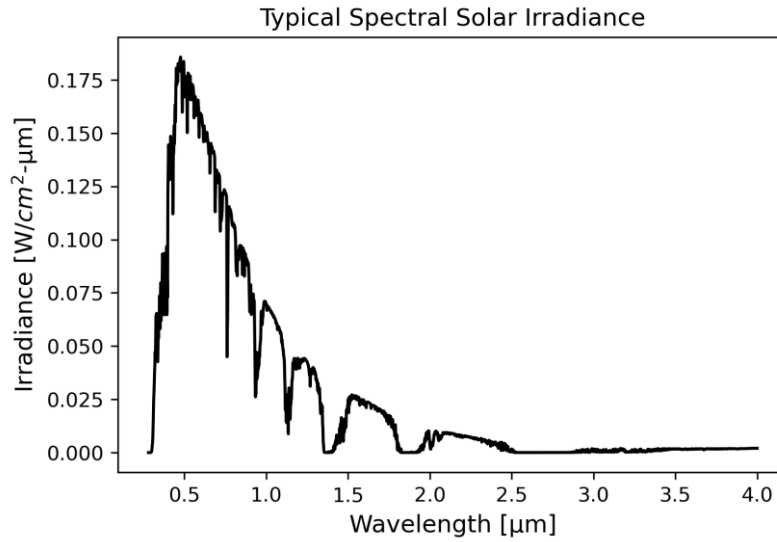
Figure 2.3: Solar Irradiance Curve typical for a desert type atmosphere. Plot data from MODTRAN6®.
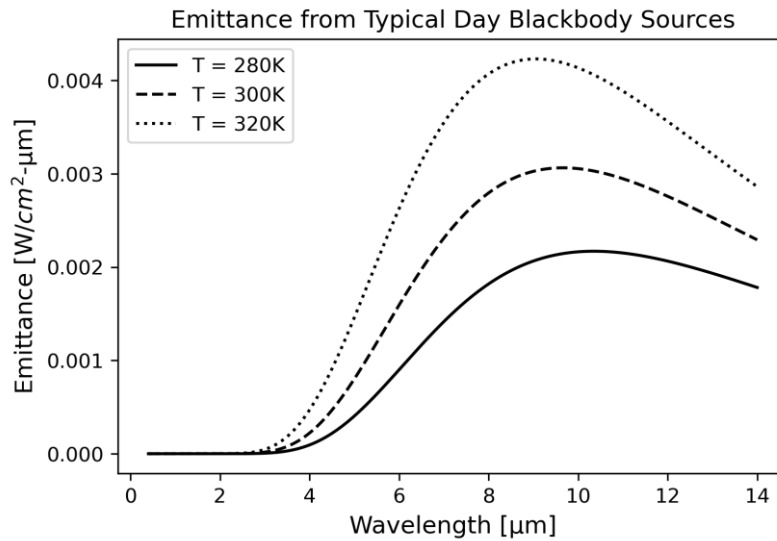
Figure 2.4: Spectral blackbody emittance typical for a span of object temperatures within an ambient scene. All

emissivity's are assumed as ε = 1.

For an ambient day as defined above, Figures 2.3 and 2.4 show that the solar illumination provided by the sun does not contribute much to the emissive bands and normal day blackbody emittance does not produce much light in the reflective bands. The ratio of light in each band compared to the total integrated irradiance and emittance from the curves in Figure 2.3 and 2.4 are shown in Table 2.1. The ratios are given by the equations,

$$\%Ref(\lambda) = \frac{\int_{\lambda_1}^{\lambda_2} E(\lambda)}{\int E(\lambda)} \cdot 100 \tag{2.2}$$

$$\%Emit(\lambda, T) = \frac{\int_{\lambda_1}^{\lambda_2} M(\lambda, 300K)}{\int M(\lambda, 300K)} \cdot 100 \tag{2.3}$$

Where *%Ref(λ)* is the percentage of reflected light, *E(λ)* is solar irradiance, $\int E(\lambda)$ is the total integrated irradiance from 0.4 to 14μm, λ_1 is the shorter wavelength cutoff in each band and λ_2 is the longer wavelength cut off in each band. For equation 2.3, *%Emit(λ)* is the percentage of emitted light for each spectral band at 300K and $\int M(\lambda, 300K)$ is the total integrated emittance from 0.4 to 14μm. These ratios give an idea of the total light available by solar illumination and blackbody radiation in each band.

Table 2.1: Ratio of reflective and emitted light for a daytime illuminated ambient scene at 300K. Ratios calculated may not total to 100% due to the bands not covering the entire 0.4-14μm spectrum. For example, MWIR stops at 5μm and the LWIR starts at 8μm leaving a 3μm gap.

	VIS	NIR	SWIR	eSWIR	MWIR	LWIR
%Ref(λ)	44	25	19	3	1	0
%Emit(λ)	0	0	0	0	2	73

As the temperature of an object increases, the blackbody radiation curve shifts towards shorter wavelengths. The wavelength corresponding to where the peak of this curve shifts is defined by Wien's Law [2].

$$\lambda_{peak} = \frac{2,897.8}{T} \qquad (2.4)$$

Where T is the objects physical temperatures [K] and λ_{peak} is the peak wavelength of blackbody emittance curve [μm]. An example of this phenomenon is when metal becomes so hot that it glows red. This serves as a reminder for when higher temperatures are encountered within a scene, the shifting spectral emittance needs to be accounted for in the traditionally reflective band imagery. For our 300K ambient scene assumption $\lambda_{peak} = 9.659 \mu m$. The peak of Plank's curve for these conditions resides in the LWIR detector regime. This is one reason that LWIR serves as a better band for nighttime pilotage.

2.2) Interactions of Infrared Light and Materials

For all bands, the varying signals from objects within a scene are due to the intrinsic properties of materials. Reflectivity, transmissivity, emissivity, and absorptance characterize how light interacts with an object. When light engages with a material, the ratio of these quantities dictates how it is transferred. The total energy in this interaction is conserved between these four values [3]. This is defined by the equation,

$$1 = \rho(\lambda) + \alpha(\lambda) + \tau(\lambda) \qquad (2.5)$$

Where $\rho(\lambda)$ is reflectivity, $\tau(\lambda)$ is transmissivity, and $a(\lambda)$ is absorptance. When an object is in thermal equilibrium,

$$\alpha(\lambda) = \varepsilon(\lambda) \qquad (2.6)$$

Where $\varepsilon(\lambda)$ is emissivity. This is a good assumption for imaging ambient scenes since they are not rapidly changing in temperature. For most targeting and mapping infrared imaging applications, $\tau(\lambda) = 0$, meaning the objects are opaque. Both of these assumptions bring equation 2.5 to,

$$1 = \rho(\lambda) + \varepsilon(\lambda) \qquad (2.7)$$

The ratio of a material's intrinsic properties now only relies on reflectivity and emissivity. With only two values, the amount of light that a sensor can receive is calculated from the ratio of light reflected from an object and emitted due to its temperature.

$\rho(\lambda)$ is a spectral quantity. The differences in reflectivity between the VIS, NIR, SWIR and eSWIR can be taken advantage of for passively illuminated mapping and targeting tasks. Passive in this case means utilizing the ambient solar illumination shown in Figure 2.3 as the light source instead of an active source such as a lamp or a laser. The spectral differences in reflectivity for each band result in different scene contrasts for the same image. For a targeting example, using the VIS sensor to find snakes in high grass is almost useless because they have approximately the same spectral reflectivity. If the passive imager utilizes the NIR band instead, the reflectivity of the vegetation increases and the snake's reflectivity remains low [4]. This causes the snake to lose its camouflage and the probability of finding the snake is much higher.

The proportion of light that is reflected off an object and its directionality is described by a bidirectional reflectivity distribution function (BRDF) [5]. The two extremes of materials BRDF, specular and Lambertian. A specular surface acts like a mirror where the direction of the light changes based on the surface geometry. The Lambertian limit reflects light from a surface

so that it can be viewed in any direction. Most objects within the FOV of an infrared imager can be modeled as a Lambertian surface. One exception is metals, which are a combination of both.

$\varepsilon(\lambda)$ is also spectral quantity. When $\varepsilon(\lambda) = 1$, the object is considered a perfect blackbody. Realistically most materials are graybodies or spectral emitters. In many cases, the assumption is made that an object is a gray body where all wavelengths within an imaging band have an equal emissivity. In the spectral emitter case, the emissivity changes with wavelength and will greatly influence the total integrated emitted radiation from the source in the different infrared bands (Figure 2.5). For Figure 2.5, all sources are assumed to have a temperature of 300K. If the graybodies and spectral emitters emissivity's are known, equation 2.7 then defines the materials reflectivity. This ratio, alongside BRDF, defines the quantity of emitted and reflected light that can be received by a sensor.
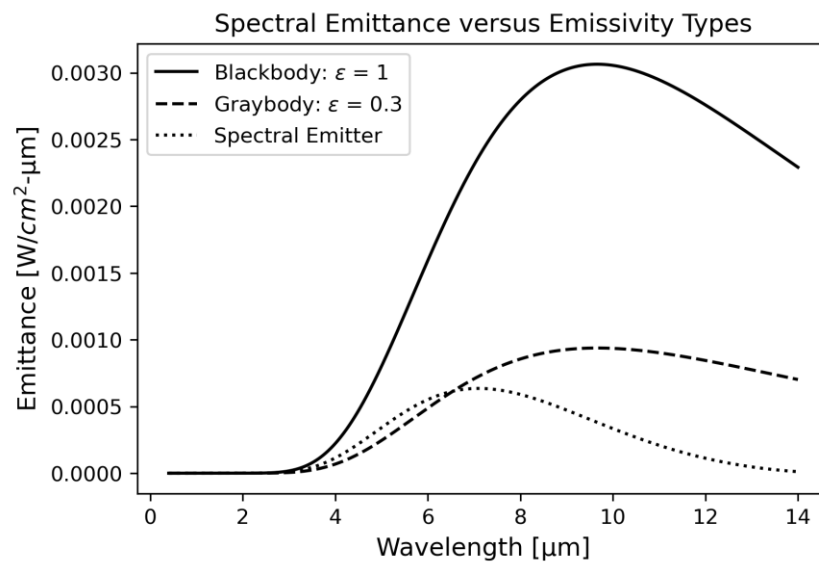
Figure 2.5: Example of emittance types for a blackbody, graybody and spectral emitted where the emissivity is high for shorter wavelengths and decreases for the higher wavelengths.

When imaging a metal material, the emissivity, reflectivity, and BRDF can change greatly based on both the imaging band and surface roughness. One band dependent BRDF example that is seen regularly is rough metals looking diffuse in the VIS and specular in the LWIR [6]. Both bands still have high reflectivity, but the rough metal can still act more closely to a mirror in the LWIR than the VIS. Metal signatures in the LWIR can give reflections with good contrast that need to be mitigated in imaging tasks [7]. For outdoor system designs, cold sky specular reflections off of metals in the LWIR need to be considered when looking at target signatures [8]. The high reflectivity of metal can either help identify objects within a sensors FOV or stretch an un-cooled microbolometers dynamic range too far and the contrast of the scene is reduced. For the application of aviation-based sensors, the metal's reflectivity in the LWIR is more likely to reflect the cold sky. This geometry can greatly change the dynamic range of the scene to incorporate the values of cold sky and warm ground instead of stretching the contrast based on the warm ground itself [9].

For both targeting and mapping, the surfaces modeled need to consider reflectivity, emissivity, and their specular versus Lambertian BRDF. If the signals of a scene are studied, the contrast of the important objects within the scene from these quantities can greatly benefit the design process. With the SWaP and cost of SWIR and eSWIR coming down greatly in cost their spectral differences can be explored for commercial and military applications. These bands cost much more than the VIS and NIR bands so the performance and contrast increases due to these spectral differences would need to greatly out way to cost differences to the cheaper sensors.

2.3) Reflected and Emitted Sources for High Temperature Environments

In the traditionally reflective bands (VIS, NIR, SWIR, eSWIR), objects at regular temperatures (300K) within the scene do not produce enough emitted light to be detected above the reflected solar radiance. Even a material like Vantablack that has a reflectivity of ~0.01 and an emissivity of ~0.99 does not emit enough light at 300K in the VIS, NIR, SWIR, and eSWIR to be detectable over the very low reflected signal (Figure 2.6-2.9).
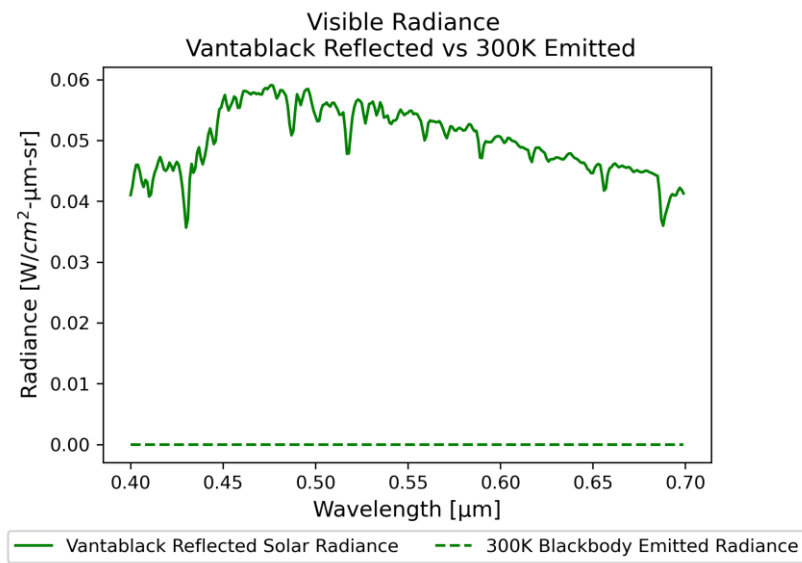
Figure 2.6: Visible solar reflected radiance from a Vantablack target versus the emitted radiance from a Vantablack target at 300K.
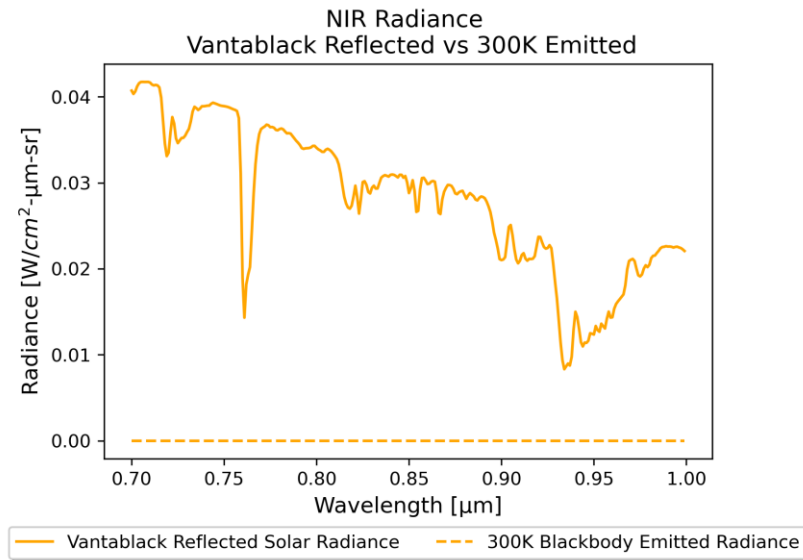
Figure 2.7: NIR solar reflected radiance from a Vantablack target versus the emitted radiance from a Vantablack
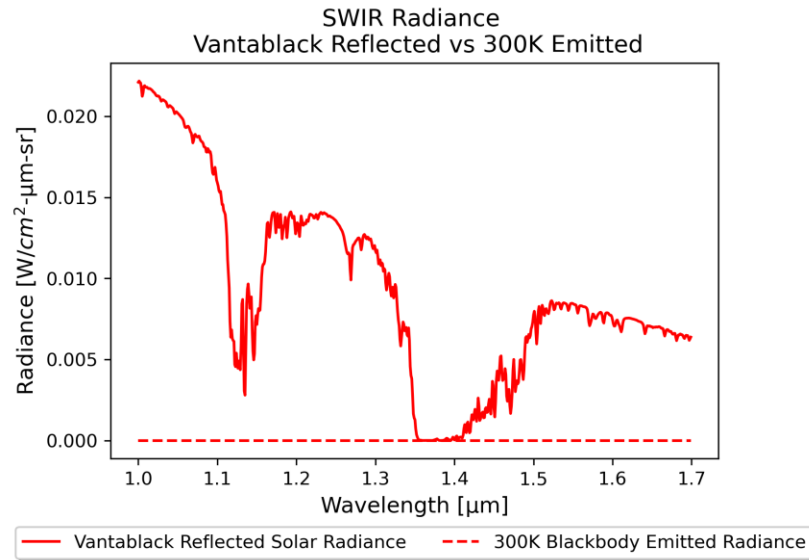
target at 300K.

Figure 2.8: SWIR solar reflected radiance from a Vantablack target versus the emitted radiance from a Vantablack
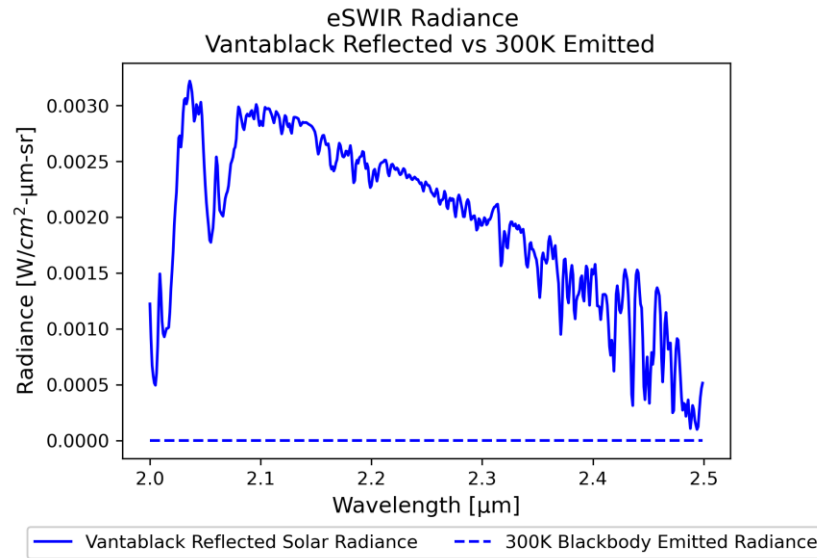
target at 300K.

Figure 2.9: eSWIR solar reflected radiance from a Vantablack target versus the emitted radiance from a Vantablack target at 300K.

The emitted Vantablack signal can become comprable to the reflected signal when it heats up, or when the illumination from the sun is reduced. For this example the assumption of good solar illumination during an ambient day is kept and the modeled Vantablack's temperature is increased. As is clearly seen in Figure 2.3 and illustrated in Table 2.1, the ratio of light in each of the bands for solar irradiance varies. This fact, combined with Plank's curve emitting more light at longer wavelengths for lower temperatures, creates a unique situation where the temperature at which the Vantablack emitted and reflected signal are equal is lower at longer wavelengths than shorter ones. The Vantablack temperature needs to be even higher to create an equal signal for the reflected and emitted light in the VIS, NIR and SWIR bands than the eSWIR (Figures 2.10-2.13). For this demonstration, a typical total solar irradiance of 1kW/m^2 is used [10].
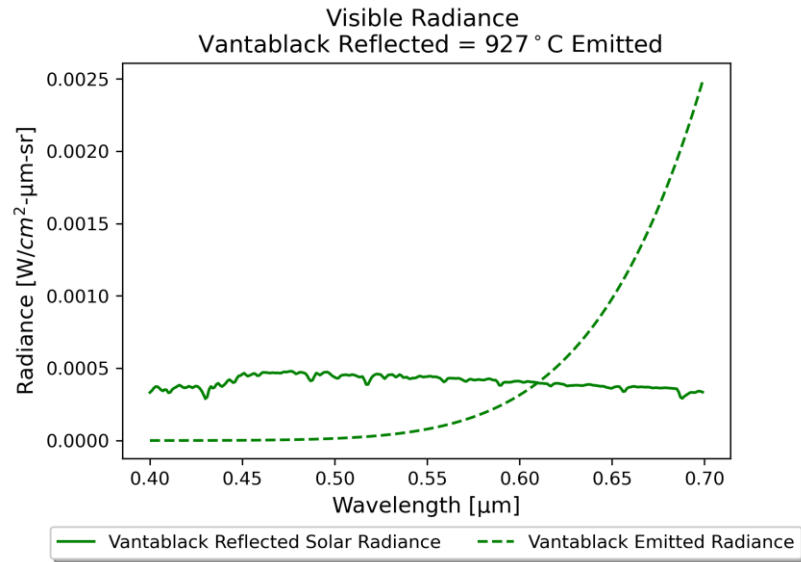
Figure 2.10: Visible emitted radiance from a Vantablack target when it is equal to the solar reflected radiance from a
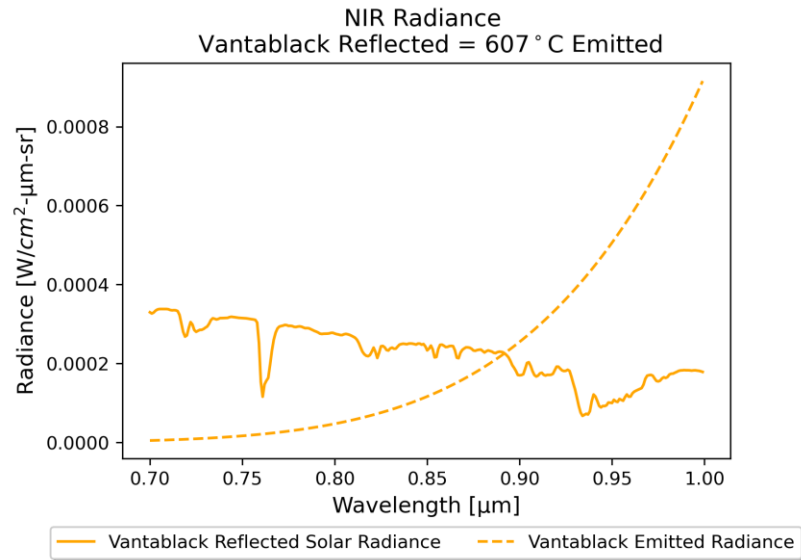
Vantablack target.

Figure 2.11: NIR emitted radiance from a Vantablack target when it is equal to the solar reflected radiance from a
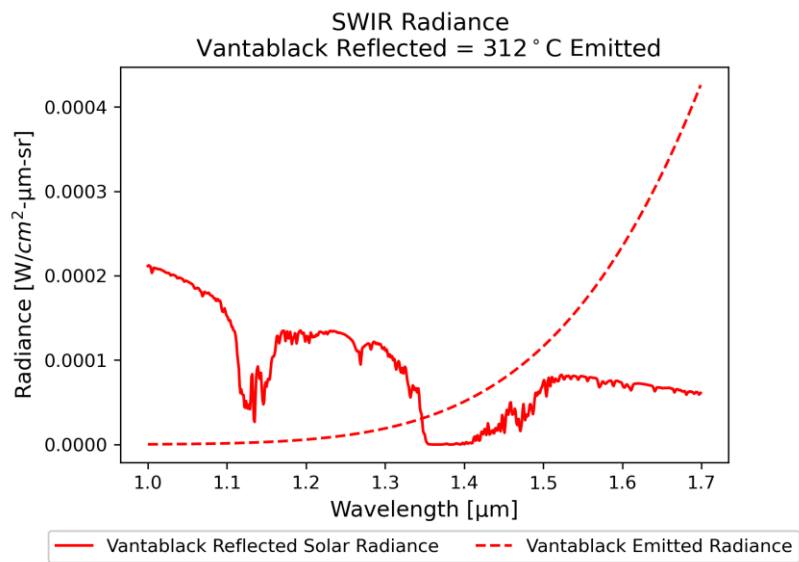
Vantablack target.

Figure 2.12: SWIR emitted radiance from a Vantablack target when it is equal to the solar reflected radiance from a Vantablack target.
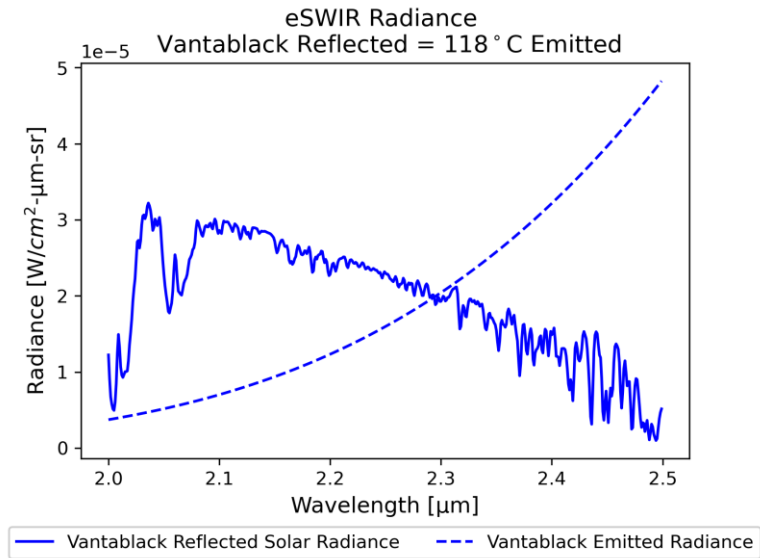
Figure 2.13: eSWIR emitted radiance from a Vantablack target when it is equal to the solar reflected radiance from a Vantablack target.

The VIS band needs a very hot and highly emissive source to have a signal comparable to a low reflectivity object for ambient illumination. Even intense situations such as a forest fire don't produce much visible emitted light outside of the active flames. On the other hand, the eSWIR is sensitive to lower temperatures and they need to be considered in the sensor design. If an eSWIR sensors was needed to help find minerals in a mine after a detonation, the scene might give false positivies based on the surround rocks emitted signal. On top of that, as soon as the solar illumination decreases, even lower temperatures need to be accounted for.

2.4) Modulation Transfer Functions

The modulation transfer function (MTF) of a sensor system defines how spatial frequencies pass through an imaging system [11]. All of the previously analyzed signals within a scene would be affected by the systems MTF. Even if there are large reflectivity differences between objects that give good contrast in the physical world, a sensor with a poor MTF might not output that same detail in the imagery. The blurring of good contrast signals due to the sensor system could render an image almost useless. Figure 2.14 shows an example of an imaging system measuring an ideal 4 bar target with a low reflectivity background and 4 high reflectivity targets. This imaging system modeled represents one that passes spatial frequencies well with some amount of "acceptable" blur. Figure 2.15 depicts a poor imaging system with an MTF that blurs the 4-bar target significantly. Due to the blurring of the system, the original image contrast is almost lost, and the strong original signals are not able to be used as effectively.
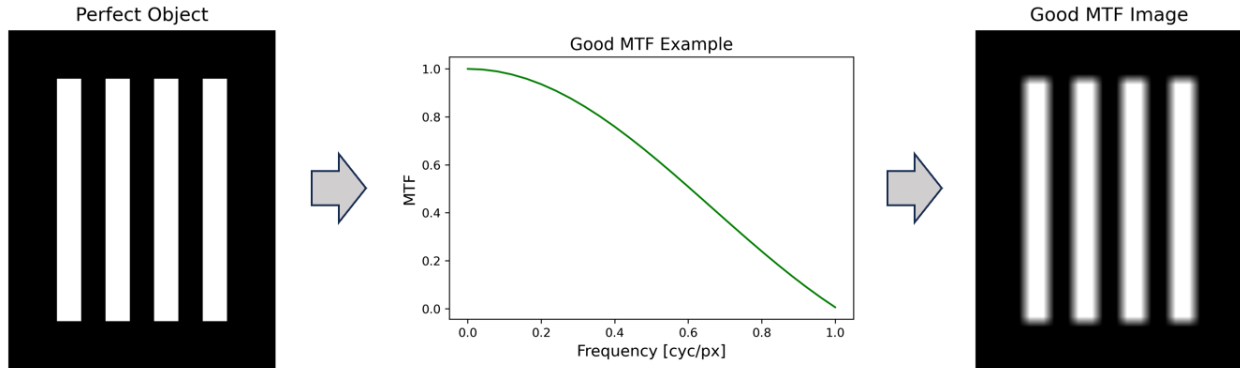
Figure 2.14: The MTF does degrade the image but the strong contrast between the 4 bars and the background is

maintained.
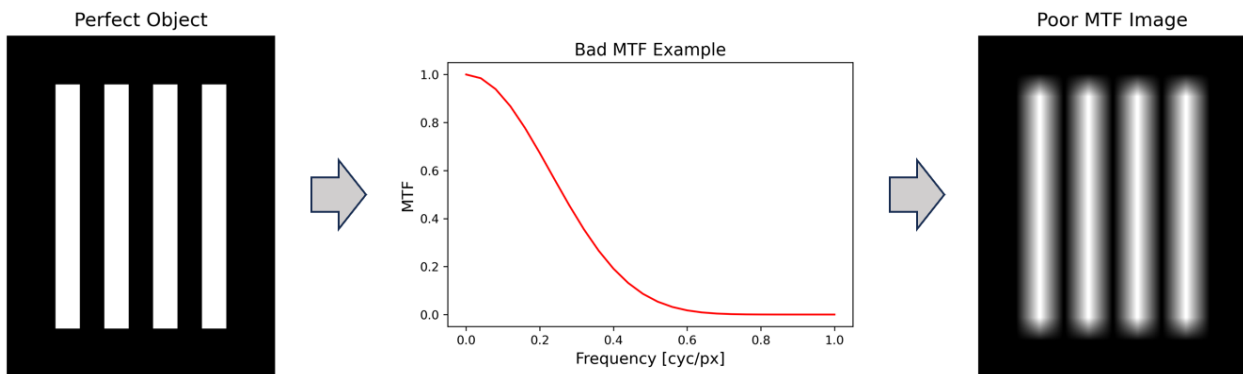
Figure 2.15: The MTF degrades the image a lot and the strong contrast is blurred significantly reducing the good

contrast signals.

Each of the components of a sensor and the environment add blur to the image. The lens, lens focus, detector, atmosphere, turbulence, vibrations, and dynamics of the imaging platform all add blur to the image. The nominal performance of a sensor system can be measured in the lab, but the effects of the environment and the platform need to be considered for its deployed

application. In the case of drone integrated sensors, the vibrations and in-flight drone dynamics can degrade the sensor significantly if not taken into account during the design process.

When designing a sensor system for a mapping or targeting tasks, the MTF directly relates to the performance of that sensor [12]. To measure the optimal MTF of an infrared sensor a tilted edge target method is generally used. Another method that can be used to measure the amount of blur in a system is the point spread function (PSF) [13]. To measure the PSF, a point source with a small spatial extent (as close to an impulse response as possible) is imaged through an optical system and the resulting spatial blur measured through the optical system is the PSF of the system. This method could be used as well for infrared systems but producing the amount of light needed to detect the PSF is difficult. To get around this obstacle in the infrared, the tilted edge method is used.

A tilted edge with a sharp edge is imaged with a bright side and a dark side. In the reflective bands, this can be created with a uniform black painted half moon target in front of an intregrateing sphere (Figure 2.16). The same effect can be created in the emissive bands with the same room temperature half moon target and a hot blackbody source. The resulting image contains a dark side and a light side with a sampled edge that transitions from light to dark. A region of interest (ROI) is drawn that only emcompasses the uniform white side, uniform black side an the transitions (Figue 2.16). The information contained within the ROI is used to calculate the MTF. The pixels gradient transition between light to dark contain information on how spatial frequencies are passed through the imaging system.
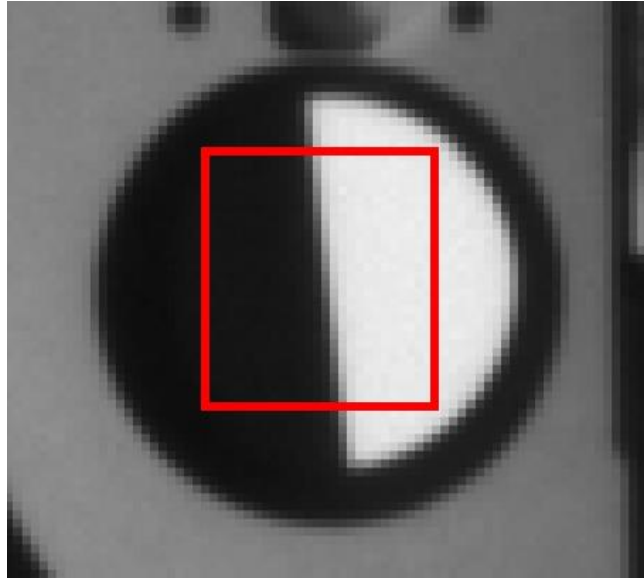
Figure 2.16: Image of a tilted edge created from a half moon target and an integrating sphere. The red ROI represents the data that would be analyzed to create the MTF

This 2D data is organized into a 1D data set that creates the edge spread function (ESF). The ESF showcases how quickly the transition from dark to light signal happens. The derivative of te ESF results in the line spread function (LSF). The line spread function in this case is synonymous with a 1D slice through the center of a PSF or a radially averaged PSF.

$$LSF(u) = ESF(u)\frac{d}{du} \qquad 2.8$$

To obtain the MTF, the Fourier Transform [14] of the LSF is taken.

$$MTF(\xi) = \mathcal{F}\{LSF(u)\} \qquad 2.9$$

The resulting laboratory MTF measurment represents the optimal performance of the designed sensor. Once this is known, the performance of the camera system when imaging of a scene can be modeled. The effects of the environmental factors can also be introduced to identify

the causes of blur outside of the optimal performance so they can be mitigated. For drone platforms the vibrations and flight dynamics can introduce signaficant blur so dampening systems or other interventions can be used to enhance performance.

2.5) Targeting Task Performance Metric

The MTF of a system is important to know when modeling the performance of a sensor system. For modeling targeting systems, the targeting task performance (TTP) metric is used to determine the probability of completing a task versus range [15]. The TTP model can also be used to model the performance of pilotage systems and could extrapolate to mapping applications as well [9]. A few of the major contributors that the TTP metric considers are the sensor sensitivity, sensor resolution, the area of the target of interest, the contrast of the target, the contrast threshold function of the eye (CTF_{eye}), noise, the range of the target and the degree of difficulty of discriminating the target. Three general levels of targeting scenarios are probability of detection (P(det)), probability of recognition (P(rec)), and probability of identification (P(ID)).

The first step to determining TTP is to calculate the system contrast threshold function (CTF_{sys}). The CTF_{sys} variables include the CTF_{eye}[16] the measured or modeled MTF of the system (MTF_{sys}) and the noise floor of the system $NF(\xi)$ [17]. The contrast of the eye needs to be considered because visual acuity directly corresponds to the ability to detect targets within the image displayed from the FOV of the sensor. The CTF_{eye} is modeled to account for the perceivable spatial frequencies as a function of luminance. As spatial frequencies increase, the visual acuity of the human eye can no longer perceive the high contrast between the low and

high display luminance. In the same manner, lower frequencies cannot be distinguished if the contrast is reduced. The finite region of spatial frequencies that a human can distinguish for a given display luminance is the CTF_{eye}.

The noise of both the eye and the system are also considered because high noise can cause false positives or degraded the contrast of an image.

$$CTF_{sys}(\xi) = \frac{CTF_{eye}(\xi)}{MTF_{sys}(\xi)} NF(\xi) \qquad 2.10$$

The CTF_{sys} shows the contrast available for a human to perform the task at hand as a function of spatial frequency, ξ. To Calculate the TTP, CTF_{sys} is compared to the contrast of a target that is being imaged, c_{tgt}.

The contrast of the target can be calculated from the signals available in the scene as described in the previous section.

$$c_{tgt} = \frac{\sqrt{(\Delta\mu)^2 + \sigma_{tgt}{}^2}}{2 \cdot \mu_{scene}} \qquad 2.11$$

The contrast is given by difference average signal between the target and the background ($\Delta\mu$), the standard deviation of the target signal (σ_{tgt}), and the average scene signals (μ_{scene}). The TTP value is found by,

$$TTP = \int_{\xi_{low}}^{\xi_{high}} \sqrt{\frac{c_{tgt}}{CTF_{sys}(\xi)}} d\xi \qquad 2.12$$

Where the ratio of the target contrast and system CTF is integrated with respect to the high and low spatial frequencies within the systems extent. The cycles on target with the current imaging system and target for a given range is now,

$$V = \frac{\sqrt{A}}{R} TTP \qquad 2.13$$

Where A is the area of the target and $\sqrt{A}$ is referred to the characteristic dimension of the target, and R is the range to the target. V is a function of range and is used to calculate the probability of completing a task. Using,

$$P(R) = \frac{\left(\frac{V(R)}{V_{50}}\right)^{1.5}}{1 + \left(\frac{V(R)}{V_{50}}\right)^{1.5}} \qquad (2.14)$$

the probability for a certain task is calculated for each range to the target. $V(R)$ is the V number found as a function of range, and V_{50} is a quantity that is found for when $P(R)$ is equal to 50%. V_{50} is a term that is found experimentally through perception testing and changes for each target and for each targeting task of detection, recognition, and identification.

In generally, for a target with a characteristic dimension of 3.1 meters (which corresponds to a vehicle the size of a truck), the P(det) $V_{50} = 2$, the P(rec) $V_{50} = 7.5$, and the P(ID) $V_{50} = 13$. The probability for each task versus range can now be given as a general performance calculation for any imagery with any target (Figure 2.17). The sensor and scene values used to calculate probabilities associated with Figure 2.17 are shown in table 2.2. A typical military specification P(task) = 80% as the cutoff performance for an imager. Figure 2.17 shows how well the targeting task can be completed versus range. These plots can be created for each of the imaging bands and under many different atmospheres and imaging environments to show their performance for any situation they encounter.
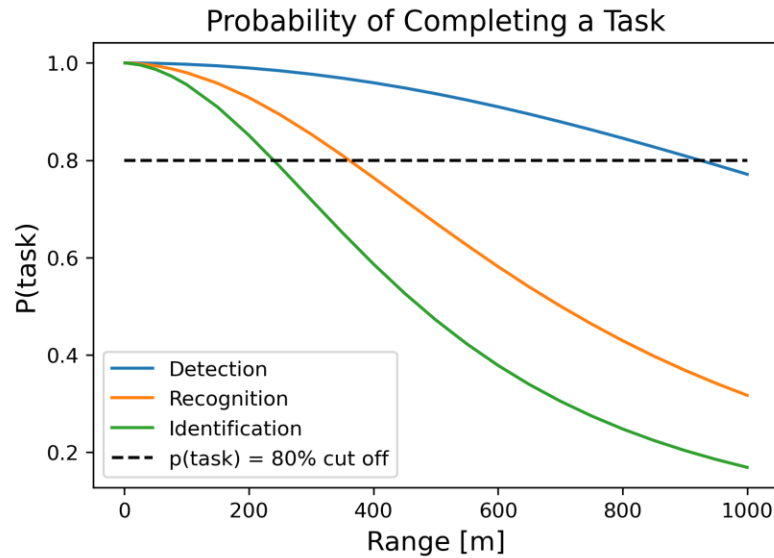
Figure 2.17: Probability of detecting, recognizing, and identifying a truck with a characteristic dimension of 3.1m versus range. The typical cut off for a sensor of P(task) = 80% is shown.

Table 2.2: Parameters used to create the probability curves in Figure 2.17.

Sensor Parameter	Value	Scene Parameters	Value
Sensor Band	8-14µm	Target Size	3.1m
Pixel Size	12µm	Target Delta T	3K
NETD	40mK	Scene Average Temp	300K
F/#	1	Target Average Temp	300K
Focal Length	18mm	P(det) V_{50}	2
Format	640 x 512	P(rec) V_{50}	7.5
Sensor Type	Uncooled µ-bolometer	P(ID) V_{50}	13

2.6) Degraded Visual Environments

The design of mapping and targeting systems is generally done with good atmospheric conditions in mind. The unfortunate reality is that a clear sky day is rare in many imaging cases. Particulates present in the atmosphere degrade the line of sight of a sensor through scattering. To

model the performance of a sensor all atmospheric effects should be accounted for. In the TTP section, the probabilities were calculated assuming a 23km visibility atmosphere. This corresponds to an atmosphere that is clear with good transmission where imagers can view long distances with minimal signal loss.

A degraded visual environment (DVE) scenario that will reduce the performance of a sensor is a 5km atmosphere [18]. This atmosphere corresponds to a smoggy city like Los Angelos where the path radiance of the atmosphere is very high. The reduction of performance decreases differently with wavelength. When modeling the 23km vs 5km atmospheres, the added particulates in the air will affect the shorter wavelengths over longer ones. The added particles in between the sensor and target scatter the signal more, reducing contrast and therefore performance. The atmosphere itself is one consideration that needs to be considered when designing infrared systems, especially for long ranges.

Alongside the general atmosphere, other constituents that reside within it need to be evaluated in the design. The presents of fog, rain, smoke, dust, haze, and other particulates need to be evaluated if they will be encountered during the sensor's deployment. All these obscurants affect the imaging bands differently. Similar to the atmosphere, as the wavelength of the imager increases, the better penetration the sensor has through these particulates. There are a few different ways to calculate the transmission reduction from to their scattering. Optical density (OD) is one way to calculate the loss of target signal through the obscurant [19]. A large OD causes a significant decrease in transmission and a low OD affects the signal minimally.

While OD offers an easy calculation to spectral transmission loss, it does not consider the concentration of the particles within the FOV of the sensor. A higher concentration of these particles would cause the OD to increase. Another option to calculate transmission loss is to use

a particles spectral extinction coefficient and the concentration length [20]. This method is consistent with sensor performance modeling software such as the night vision integrated performance model (NVIPM). The spectral extinction coefficient describes the amount of light that is lost for a given particle due to the wavelength [21]. This value is a specific characteristic of each particle type. Concentration length describes the total amount of an obscuration that is in the sensor's optical path [22].

These two values together provide a more complete understanding of the presence of particles and the transmission loss for each particle type, concentration, and wavelength. A plethora of obscurants and their effect on each imaging bands transmission can be modeled. The concentration that an imager can no longer view an object can be found in each band. The contrast of a scene or a target for the mapping and targeting cases can now be calculated along with the performance degradation due to obscurants in the atmosphere.

Chapter 3: Rural and Urban Scene Contrast from an Aviation Perspective

This chapter is an amended version of the original manuscript:

Patrick Leslie, Richard Col. Cavanaugh, Shane Jordan, Lindsey Wiley, Eddie Jacobs, Ronald Driggers, and Joseph Conroy, "Visible, NIR, SWIR, and eSWIR urban and rural scene contrast comparison," Appl. Opt. 63, 1839-1846 (2024)

3.1) Overview

The spectral information contained in the reflective imaging bands can be exploited for specific tasks. Whether targeting or mapping, the visible (VIS), near-infrared (NIR), shortwave infrared (SWIR), extended shortwave infrared (eSWIR) bands perform very differently for every application. For any imaging project, high contrast is very important for good imagery. High contrast leads to more recognizable features within a scene and easier identifiable objects. For mapping, good background scene contrast gives prominent features more detail and their locations can be easily identified. For targeting, low background scene contrast reduces clutter, making it easier to detect objects of interest. The VIS, NIR, SWIR and eSWIR bands are popular reflective bands to design daytime imaging systems for either task. Deciding on which band will have the best contrast for a specific task is one of the first things to study when designing an imaging system. By measuring urban and rural scenes in terms of equivalent reflectivity, a direct comparison of these four bands can show the utility they provide. The systems used to measure scene contrast are designed to have the same spatial resolution and field of view (FOV). With these instantaneous FOV (IFOV) matched systems, the variance and 1D power spectral densities (PSD) provide a quantitative comparison for the contrast between the four bands. The equivalent

reflectivity differences and resulting contrast measured between these four bands show that the eSWIR has the highest contrast in both urban and rural scenes.

3.2) Introduction and Background

Reflective infrared imaging bands have been receiving a lot of attention in recent years. The spectral information contained in the visible (VIS, $0.4 - 0.7\mu m$), near- infrared (NIR, $0.7 - 1.0\mu m$), shortwave infrared (SWIR, $1.0 - 1.7\mu m$), and extended shortwave infrared (eSWIR, $2.1 - 2.6\mu m$) provide useful information for different imaging tasks. These bands are defined by good atmospheric transmission windows and detector materials. The accessibility to sensors in these bands has dramatically increased due to the advancement of focal plane materials, leading to lower costs and lower SWaP (size, weight, and power). eSWIR is a newer band where detectors are still more expensive. All these sensors have proliferated on both military and commercial platforms to increase the performance of existing imaging systems. Alongside sensor improvements, the longevity of UAV (unnamed aerial vehicles) flights and increased payload capacities to carry these systems has brought infrared imaging into the air. Whether from the ground or air, these four imaging bands are rigorously being studied, to find the best performance in both ideal and degraded visual environments for a large range of applications.

From a commercial point of view, the infrared bands give great insight into the agricultural [1], forest [2], wildlife [3] and mining [4] communities. Both broadband and hyperspectral imaging in the infrared gives more information about plant health, wildlife management, geological surveying, and minerology than the VIS band can alone. From a military point of view, the longer wavelengths benefit in long range targeting [5], GPS-Denied

navigation [6,7], imaging through degraded visual environments [5], and situational awareness. In any case, the infrared imaging technologies are advancing sensing capabilities for all. The benefits that certain imaging bands have over the others are due to the reflective properties of the materials imaged, the illumination conditions, and the sensor performance. As an example, the eSWIR band excels at spectral geological mapping due to strong absorption features in hydroxyl and carbonate bearing minerals [4]. The NIR is best suited for identifying metals with multiple valence states such as cobalt, vanadium and titanium [8]. By using a sensor with the appropriate spectral range, the unique spectral responses and effective reflectivity of these various materials give higher contrast between the surrounding substances, allowing for more accurate detection and identification.

These research topics can be separated into two general categories, targeting and mapping. Targeting objects has extensive research on the military side but the theories behind these techniques carry over into any imaging task that is trying to detect, recognize or identify objects within the FOV (field of view) of a sensor [9]. For targeting, one benefit of the infrared bands is there can be a higher contrast difference between the object of interest and the background [10,3]. When the contrast between the object and background is high, the targets are very easily detected and the probability of completing the task is high. However, in some cases, the infrared bands not only increase the target contrast but other objects in the background of the scene as well. In this case, the cluttered background environment could cause false alarms and image recognition routines need to become more advanced to find the targets of interest [11,12,13]. For the targeting case, the ideal setting would have a higher contrast between the object of interest and the background, with the clutter's reflectivity in the scene being generally uniform.

Mapping tasks benefit greatly from having a very "cluttered" background or in other words, a scene that has a lot of contrast to easily recognize features within it. Utilizing infrared and visible band imagery together can increase the ability to detect objects within a scene [14]. When using a single infrared band for non-mapping tasks, such as infrared search and track (IRST) or targeting, lots of features with good contrast are needed to correlate the infrared images to visible databases to find where these objects are [15]. Along with the traditional meaning of mapping, the agricultural, forest fire, and mining communities benefit from the increased contrast and detail that the different infrared bands give. For forest fire mapping, the longer infrared wavelengths enhance boundary mapping of the fires due to the greater contrast over the VIS band that experiences smoke obscuration [16]. In cases like these, where the visible band performs poorly, the infrared band imagery can also be correlated to known visible databases to increase the accuracy of creating these boundary maps. Another example would be locating sections of a farm with poor crop health or locating precious minerals within a mine. For mapping, scenes having a lot of contrast is great for correlating the imagery to the visible band and recognizing prominent features within the scene for locating objects more accurately.

The use of VIS, NIR, SWIR and eSWIR for both targeting and mapping is becoming increasingly popular for various applications. As these bands proliferate in military and commercial systems, their unique spectral signatures can be further exploited. The choice of using one band over the other could be decided based on its extra utility. At this point, the direct comparison of the bands in terms of background scene contrast has not been explored. To understand the benefits of one band over another for targeting or mapping, the equivalent reflectivity of urban and rural backgrounds is studied. By calibrating these four bands from gray values to equivalent reflectivity, the physical properties of the scenes can be directly compared to

study scene contrast. With this study, the choice of implementing one band over another into an imaging system can be chosen based on these contrast results.

3.3) Camera System Design

Four sensors are used for this reflective band study. Three Allied Vision Alvium 1800 U-130 VSWIR's and one PhotonEtc Zephir 2.5. The Alvium sensors have an unfiltered spectral range of approximately 0.4μm to 1.7μm. A combination of various short pass and long pass filters are used to isolate the VIS (0.4 – 0.7μm), NIR (0.7 – 1.0μm) and SWIR (1.0 – 1.7μm) bands for the three Alvium sensors. The PhotonEtc sensor spectral response is also filtered to only sense in the eSWIR band (2.1 – 2.6μm). The QE's (quantum efficiency) and transmission losses from filters for each imager are shown in Figure 3.1. Each band has a great transmission window in the atmosphere for targeting, mapping, and other applications [5].
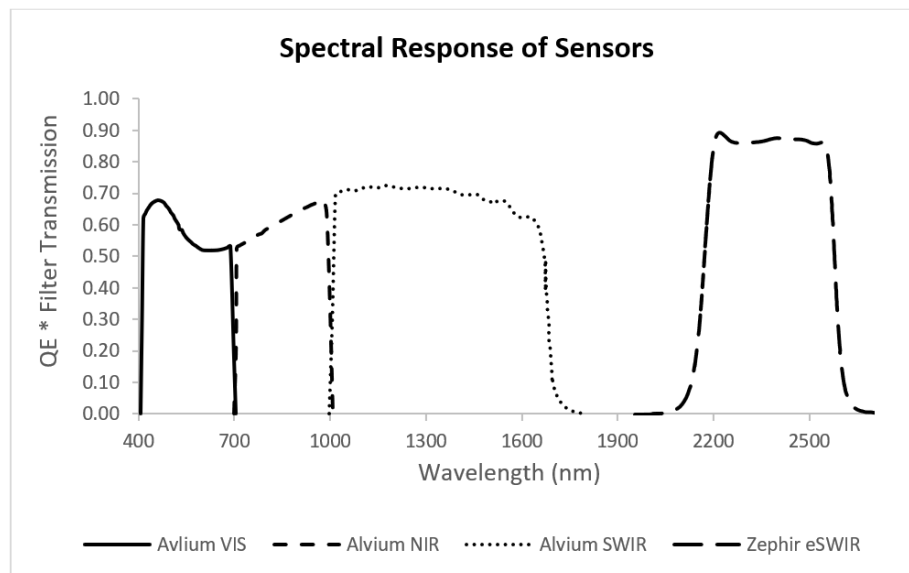
Figure 3.1: Spectral responses of the VIS, NIR, SWIR and eSWIR sensors along with their associated bandpass filters. The VIS, NIR and SWIR long-pass/short-pass filters were purchased from Thorlabs.

The VIS, NIR, SWIR, and eSWIR sensors are designed to be IFOV matched, resulting in the same spatial resolution on each scene (Table 3.1). For scenes closer to the sensor, the GSD [17] (ground sample distance) is approximately matched. An example of the GSD for a scene centered at 50m is given in Table 1. IFOV is defined in equation 3.1 and GSD is defined in equation 3.2.

$$IFOV = \frac{d}{f} \qquad \text{[mrad]} \qquad 3.1$$

$$GSD = IFOV * R \qquad \text{[cm]} \qquad 3.2$$

Where d is the detector pitch, f is the focal length of the lens, and R is the range at which the scene is sampled. It is assumed that the fill factor of the detector is 100% in the IFOV equation. These sensors are mounted on goniometers and rotation stages to align the four sensor's FOV as best as possible. The FOV's of the Alvium's are also digitally cropped to have the same format as the eSWIR. Registering the scenes to observe the same content and having the same spatial resolution due to IFOV matching allows for the direct comparison of scene equivalent reflectivity and contrast. By matching the four bands in this way, it also provides the sensors the opportunity to observe the same frequency content in each scene, which is also compared later. A description of the four sensors is given in Table 3.1. In this study, it is assumed that the pixels have 100% fill factor but fill factor may need to be considered for other sensor systems.

Table 3.1: Optical Design & characteristics of the sensor systems used to match IFOV & GSD as closely as possible with commercial optics.

Band	Sensor	Spectral Range (μm)	Format	Pixel Pitch (μm)	EFL (mm)	F/#	Fλ/d	HFOV (deg)	IFOV (mrad)	GSD @ 50m (cm)
VIS	Alvium	0.4 – 0.7	1296 x 1032	5	5.4	2.5	0.275	62	0.9259	4.62
NIR	Alvium	0.7 – 1.0	1296 x 1032	5	5.4	2.5	0.425	62	0.9259	4.62
SWIR	Alvium	1.0 – 1.7	1296 x 1032	5	5.4	2.5	0.675	62	0.9259	4.62
eSWIR	Zephir2.5	2.1 - 2.6	320 x 256	30	35	1.6	0.120	15.6	0.8571	4.29

Along with the characteristics of the sensors, the total sensor systems Modulation Transfer Function (MTF) is provided. The MTFs shown in Figure 3.2 were measured using the same configurations of sensors, lenses and filters as described in Table 3.1. The MTF's described how the spatial frequencies of a scene are passed through a sensor system. The MTF's were calculated from imagery taken from a tilted edge [18]. Referencing the MTFs when studying the 1D PSDs of the various scenes will be important. To prove the systems used are not diffraction limited, the Fλ/d metric is provided in Table 3.1 [19]. A Fλ/d > 2 describes a system that is diffraction limited. A value of less than 1 corresponds to a system that is detector limited. The values stated for each of the imaging bands show the sampling of each scene is not impeded by the diffraction limit.
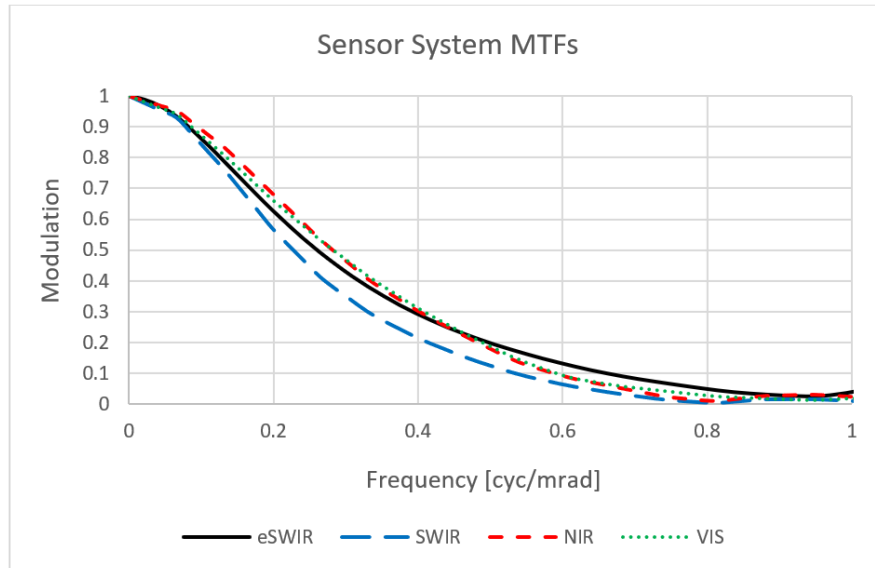
Figure 3.2: Measured MTFs for each of the sensors described in Table 3.1.

3.4) Calibration of Sensors

To compare measured scenes in the different bands, the sensors are calibrated to a comparable quantity. By converting the gray value outputs of the sensors to equivalent reflectivity (ER), a direct comparison of contrast in each of the bands is provided. Knowing the spectral reflectivity of the calibration paints allows this conversion to happen. Every material in an image has an ER that is different spectrally. A larger distribution of object's ER in the sensors FOV will correspond to more scene contrast in that band. ER normalizes the scene to a quantity that combines all the sensor's intrinsic properties to value that can be described on the same scale. Sensor variables such as QE response, spectral sensitivity, integration time, aperture size, and measured reflected solar radiance are now controlled. Without calibrating to ER, the scale of variance and amplitudes of the1D PSD analysis would be vastly different between bands.

Just before the scene measurements are obtained, a well resolved high reflectivity white and very low reflectivity black target is placed within the sensors FOV's. The two paints used to create this target are Edmunds Optics Pre-Mix White Reflectance Coating and Krylon Industrial Ultra Flat Black Acryli-Quik spray paint [20]. The spectral reflectance is known for both paints and the in-band averages for VIS, NIR, SWIR and eSWIR are used to convert gray values to equivalent reflectance (Figure 3.3, Table 3.2).
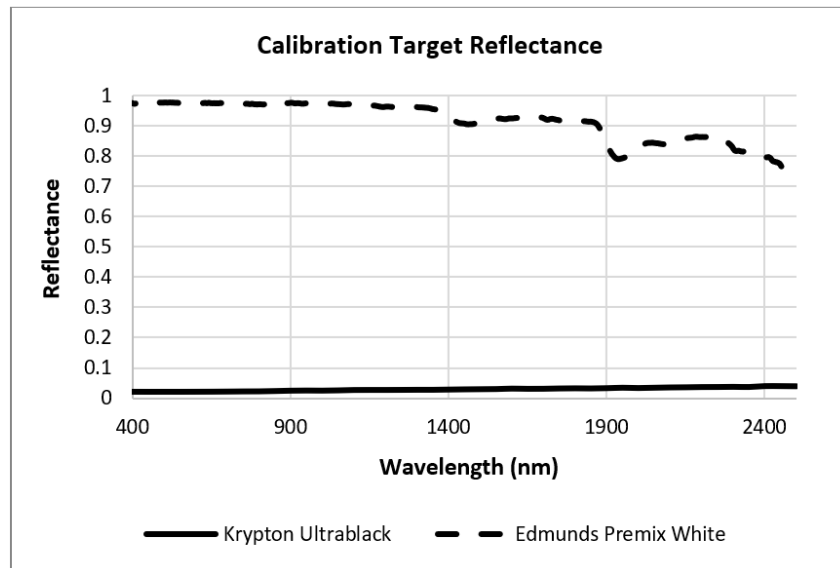
Figure 3.3: Measured spectral reflectance for the white and black calibration target.

Table 3.2: In Band Average reflectance of both the white and black paints for VIS, NIR, SWIR and eSWIR.

Paints	VIS	NIR	SWIR	eSWIR
Edmunds White	0.977139	0.974762	0.946551	0.827791
Krypton Black	0.021429	0.023807	0.028717	0.035753

The calibration target is oriented in the FOV so that it is directly illuminated by the sun. The calibration board is faced towards the sun and the center of the sensors FOV is aligned to the

board face without casting a shadow on the board. The calibration paints are Lambertian such that the illumination angle dependence is small. Each sensor is pointed at the target so that the black and white paints constrain the dynamic range for the scene. The integration time of the sensors are varied until the board is neither black nor white saturated. The integration time is also tuned so that each of the four sensors measures gray values on the white and black calibration paints correspond to approximately 10% and 90% of the sensor's total dynamic range. This is an important step to capture all equivalent reflectivities in the scene. Examples of the integration times used in the Urban data set are 400μs for VIS, 600μs for NIR, 800μs for SWIR, and 650μs for eSWIR. These integration times are varied throughout the day with the changing illumination conditions due to solar angle.

Once the dynamic range is set, the integration time and gain are held constant so that they do not change when viewing different scenes with potentially varying signals. Any non-linear histogram stretching is disabled in the sensors software's to have a constant response in gray values to the scene. A sequence of images is taken of the calibration board to convert the gray values on the white and black sections of the target to equivalent reflectivity. The sequence of calibration images contains many pixels on both the white and black sides of the calibration board. An ROI is drawn around each side of the board. The gray value averaged in time (from the image sequence) and space (from the ROI) are used for the gray value to ER conversion. This method minimized the temporal and spatial noise associated with each sensor. Using this two-point gray value to ER calibration, each of the gray values in between the calibration points are then converted to ER (Figure 3.4). This is made possible by using the linear fit of gray values mentioned earlier. Once all the scenes are converted to ER from gray values, a direct comparison of the various scenes can now be made.
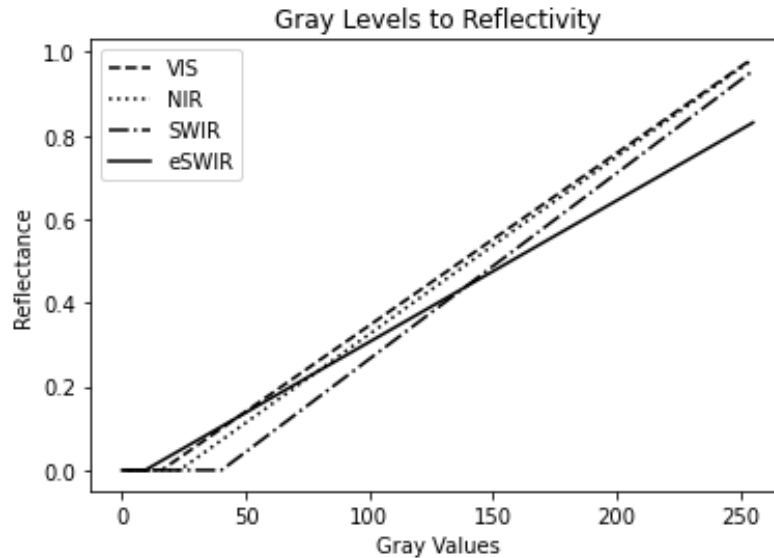
Figure 3.4: Example of one calibration curve used to convert the gray values observed by the Figures, supplementary materials, and tables.

3.5) Rural and Urban Scene Measurements

The test bed and calibration system designed above is taken to a variety of locations around Tucson, AZ to obtain both rural and urban scene reflectivity. The imagery is taken at various downward facing angles to obtain points of view, similar to a drone's perspective for both targeting and mapping applications. All data collection days have clear skies to avoid any changing illumination issues within scenes. Each data set is also taken near midday to avoid shadow effects and includes a variety looking angles. All imagery is oriented so the center of the FOV is much closer than 1km. This close path length minimizes path radiance and maximizes transmission in each band so their effect on imagery is negligible. For context, the transmission associated with a clear sky desert atmosphere at 500m is between 90% and 95% for each band. At each location, the sensors are calibrated using the methods described to accommodate

changing illumination throughout the day. 39 images are analyzed for each band with multiple scenes taken at each urban and rural location.

Urban imagery is taken around the University of Arizona in Tucson, AZ, from the top of parking garages. These scenes capture a combination of high-rise buildings and neighborhoods with streets, houses, and vehicles to encompass different urban environments. Rural scenes of desert, grassland and wooded forest are captured along Mt. Lemmon Hwy in Tucson, AZ. These locations and landscapes give a variety of realistic scenes to compare the reflectivity's between VIS, NIR, SWIR and eSWIR for terrain that an airborne system would encounter. Examples of the calibrated, IFOV matched and FOV matched scenes are shown in Figures 3.5 – 3.8. Figures 3.5 – 3.8 have been brightened to view them easier as some of the scenes mean reflectance was very low. The mean equivalent reflectivity and variance for each image is given later for reference.

The images show the great contrast associated with each calibrated sensor. At first glance, the eSWIR band shows higher contrast compared to the other bands in each of the urban and rural cases. For the rural scenes, the large reflectivity difference between the vegetation, rock, and grass, provides significant detail throughout the scene in the eSWIR, where the other reflective bands give lower contrast. In the Urban scene shown, all bands provide good detail for the various features but subtle differences such as the rooftops, sidewalks, and painted metal reflectivity's still stand out more in the eSWIR band.

Urban Scene Comparison
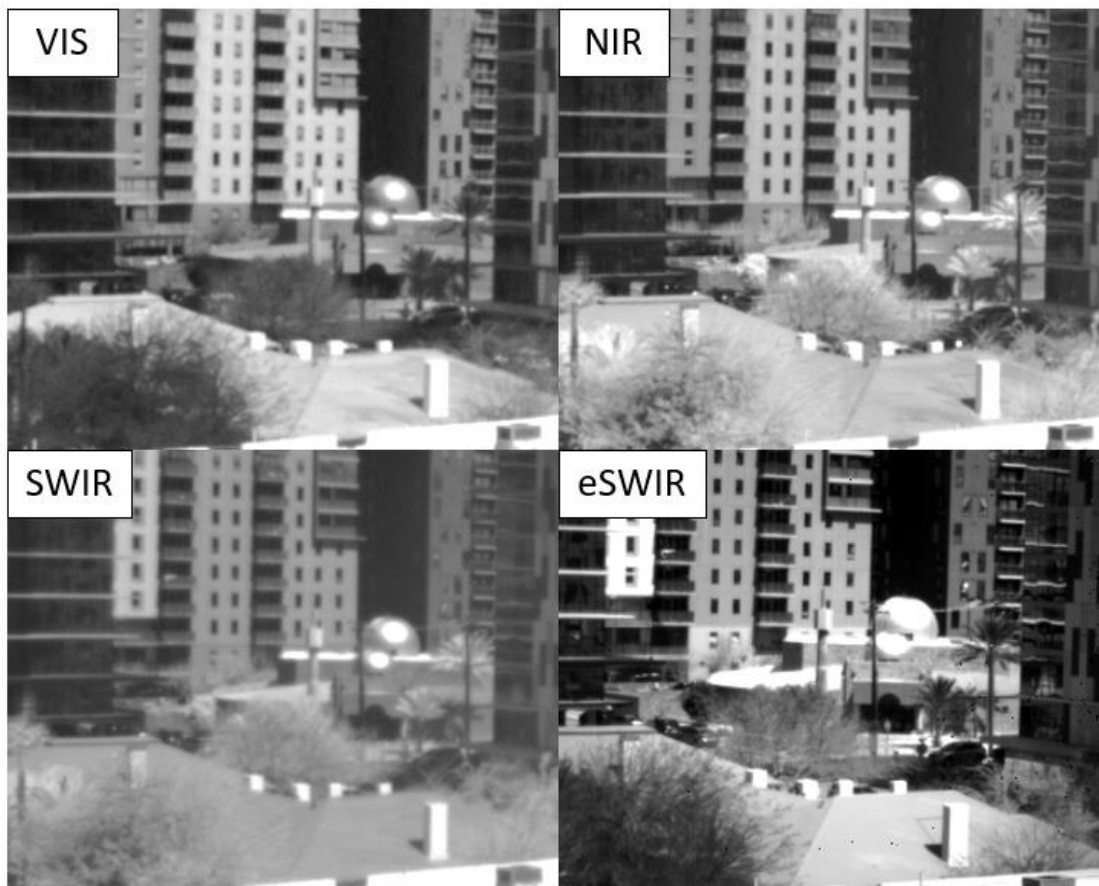
Figure 3.5: IFOV and FOV matched Urban Scene in the four imaging bands. Imagery captured at Latitude: 32.23325864878819, Longitude: -110.95873322447738, near 12:00pm on 3/27/23.

Rural Desert Scene Comparison
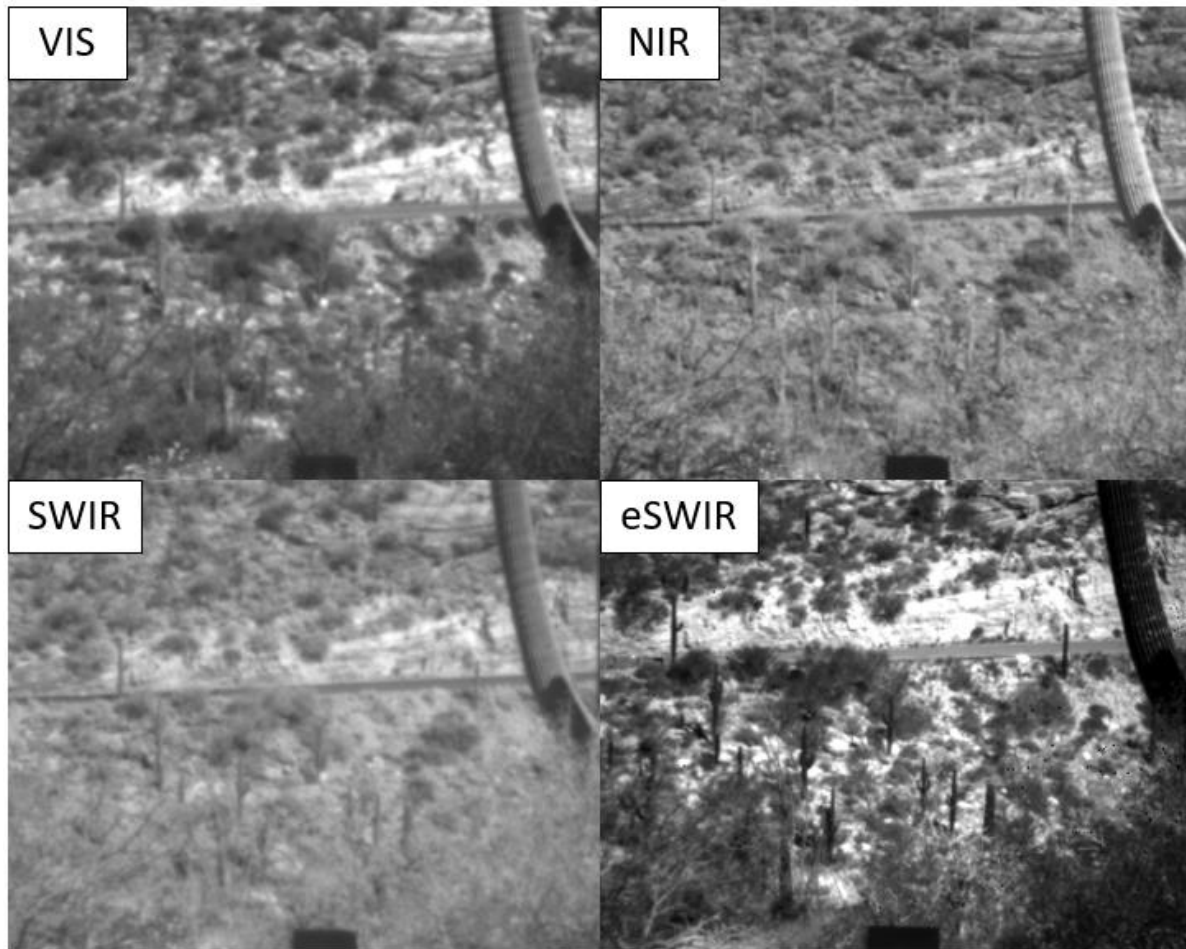
Figure 3.6: IFOV and FOV matched Rural Desert Scene in the four imaging bands. Imagery captured at Latitude: 32.309545796332124, Longitude: -110.72116135878584, near 9:30am on 3/28/23.

Rural Grassland Scene Comparison
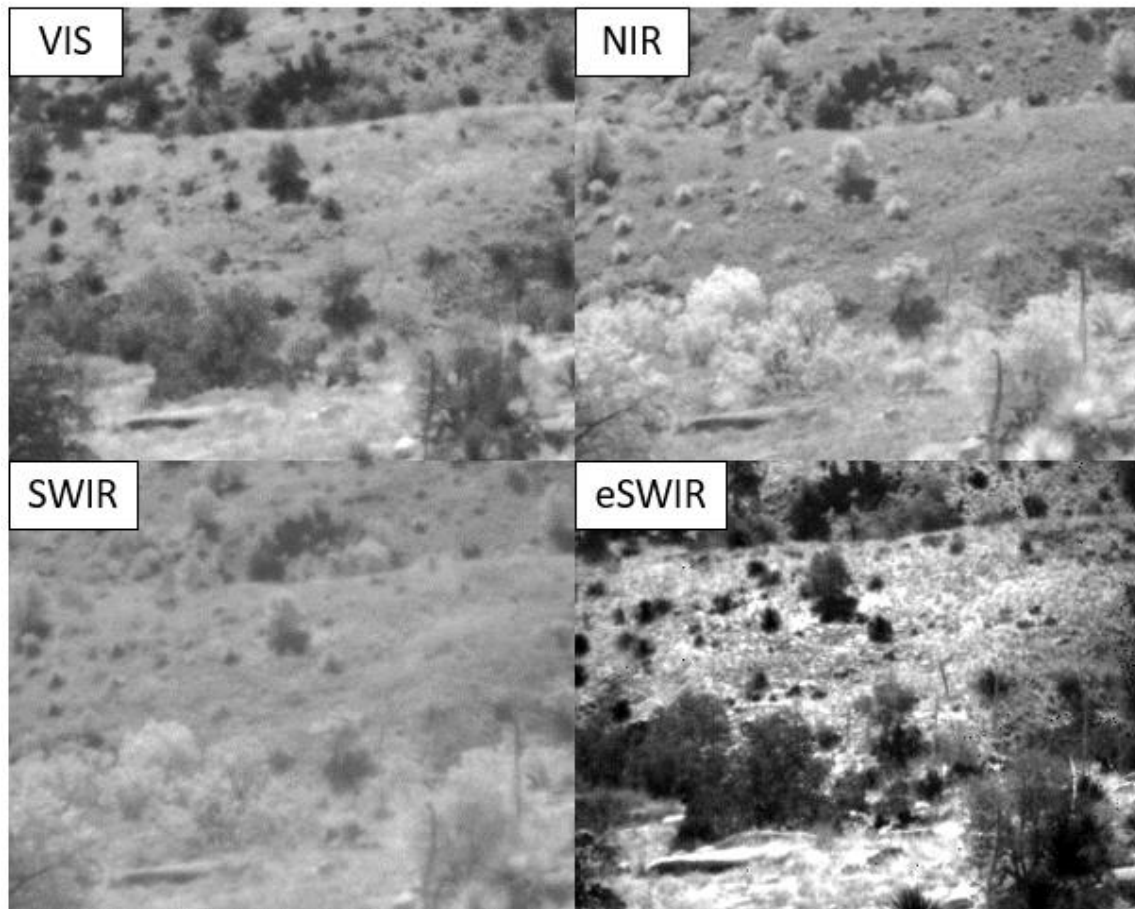
Figure 3.7: IFOV and FOV matched Rural Grassland Scene in the four imaging bands. Imagery captured at Latitude: 32.339416, Longitude: -110.709709, near 10:30am on 3/28/23.

Rural Wooded Forest Scene Comparison
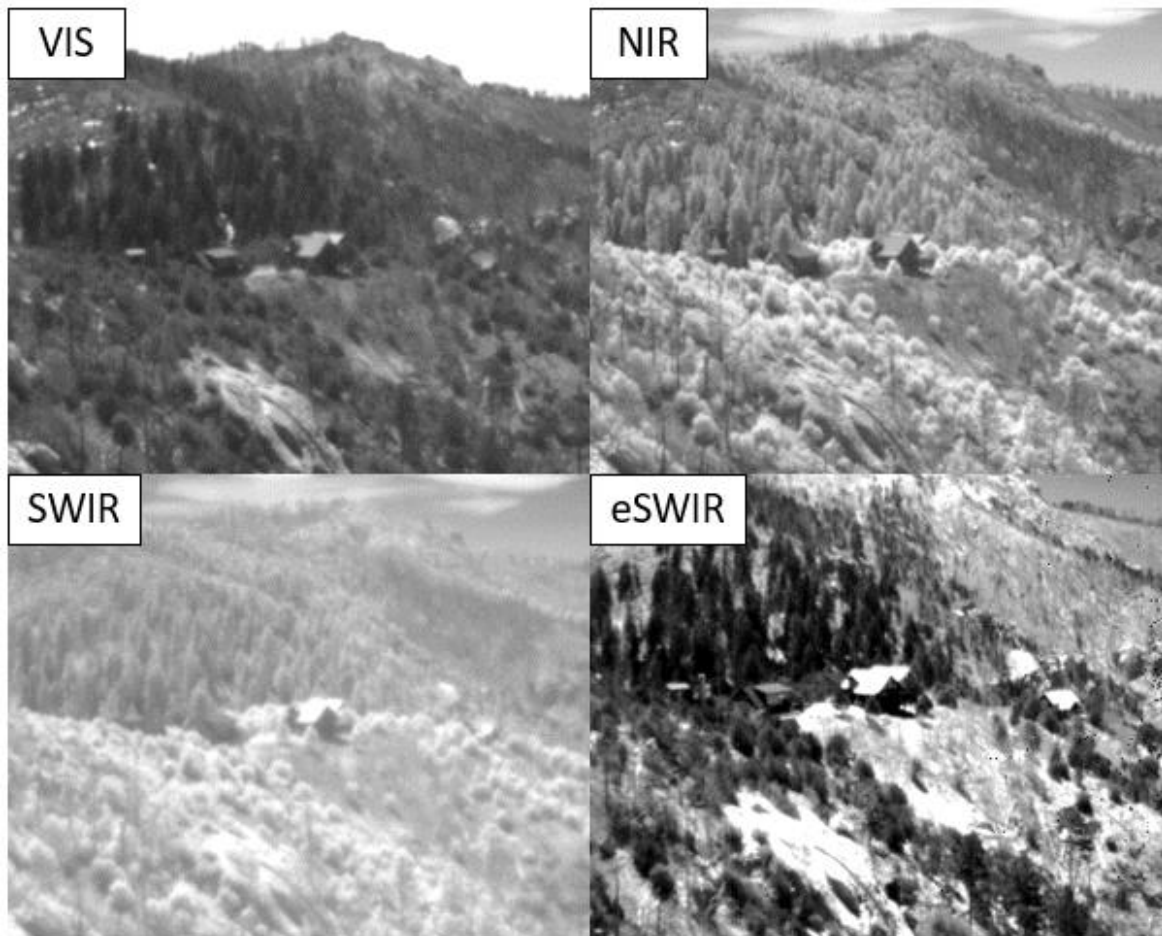
Figure 3.8: IFOV and FOV matched Rural Wooded Scene in the four imaging bands. Since this scene is further away (the cabin is approximately 500m), the GSD difference is more noticeable in the eSWIR. Imagery captured at Latitude: 32.4313828, Longitude: -110.7496712, near 12:00pm on 3/28/23.

3.6) Contrast Measurement Results

To compare the contrast of all 156 scenes, the scenes are analyzed and compared in two different ways. The calibrated scenes are compared in terms of ER to give a physical comparison instead of digital gray values. Any pixels that measure the sky are not included in the analysis. The variance of the reflectivity distribution for each scene is compared by band, to show which band

has the most contrast. The higher variance values correspond to a larger spread of ER in a scene, which in turn, corresponds to more contrast. The second method compares the 1D PSD of the various scenes by band, to quantify the amplitudes of the frequency content in each scene. The higher amplitudes for the same frequencies also correspond to higher contrast within a scene. The mean and variance for figures 3.5-3.8 are given in Table 3.3.

Table 3.3: Urban and Rural scene mean equivalent reflectivities and variance that correspond to Figures 3.5-3.8.

	VIS	NIR	SWIR	eSWIR
Urban Mean	0.1225	0.1668	0.1294	0.2210
Desert Mean	0.2148	0.4372	0.4401	0.2718
Grassland Mean	0.0327	0.1507	0.1251	0.3239
Forest Mean	0.0697	0.2046	0.2639	0.1423
Urban Variance	0.0207	0.0272	0.0216	0.0292
Desert Variance	0.0142	0.0170	0.0143	0.0329
Grassland Variance	0.0014	0.0061	0.0044	0.0365
Forest Variance	0.0024	0.0102	0.0081	0.0208

Four cases are considered for comparing VIS, NIR, SWIR and eSWIR bands. Urban, rural desert, rural grassland and rural forest scenes are compared for each band separately. With the qualitative comparison of eSWIR having more contrast than the other reflective bands, the variance of each eSWIR scene is plotted against the variance of VIS, NIR, and SWIR to show the difference between eSWIR and the other bands (Figure 3.9).

The center dotted line represents when the variance between the eSWIR and the VIS, NIR, or SWIR is equal. When the variance is favored for one specific band over another, the data will skew away from the center line. In every case, the data trends towards the eSWIR's higher variance over all the other bands. Therefore, eSWIR has more contrast in urban and rural scenes than VIS, NIR and SWIR. A ratio of the average variances for each scenario is taken to show the

contrast advantage that eSWIR has over the other bands (Table 3.4). The data in table 3.3 shows that in the urban case eSWIR gives a small advantage over the other bands and they are all comparable. For the more rural cases, eSWIR generally has a large advantage over VIS and in the grassland cases, a large advantage over all bands. This large difference is most likely to the grasslands having even reflectivity of vegetation and rocky terrain for the other bands, where the eSWIR reflectivity's of these materials are very different. Comparing the other bands shows the NIR outperforms both VIS and SWIR and SWIR generally has higher contrast than VIS.
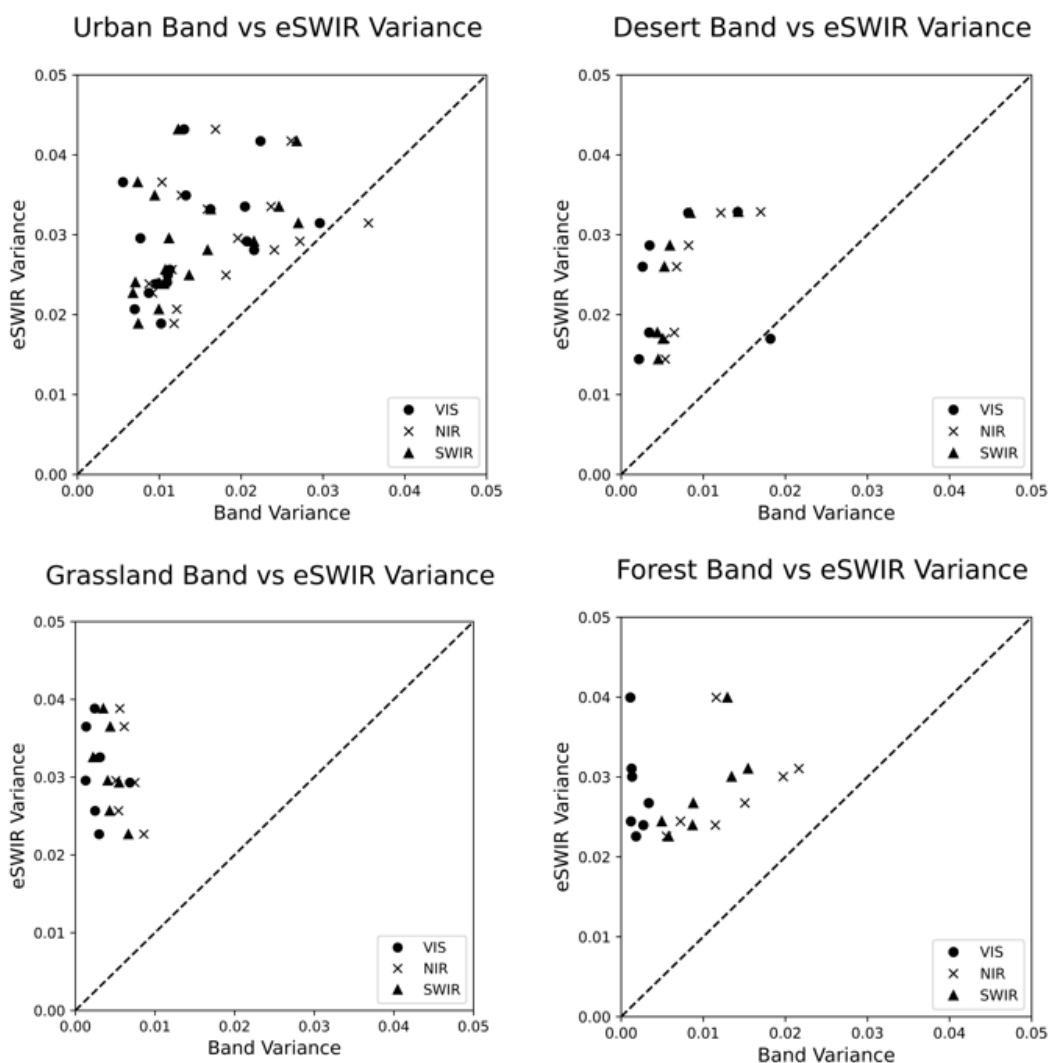
Figure 3.9: eSWIR variance plotted against the other band variances. An equivalent variance line is provided to show where the values would be equal. The seemingly outlier VIS point in the Desert analysis is due to a specular reflection within the FOV.

Table 3.4: Ratio of average variances, compared to other bands variance. All values being higher indicates that there is higher contrast in the eSWIR band for all scenarios.

Variance Ratio	Urban	Desert	Grassland	Wooded
eSWIR / VIS	1.85	3.25	10.51	15.60
eSWIR / NIR	1.51	2.76	5.24	2.15
eSWIR / SWIR	1.83	3.54	7.01	2.84
SWIR / VIS	1.02	0.92	1.50	5.50
SWIR / NIR	0.82	0.78	0.75	0.76
NIR / VIS	1.23	1.17	2.01	7.24

Along with the variance comparison, the 1D PSD of each scene is calculated. The 1D PSD is defined as

$$I(\xi,\eta) = \mathcal{F}[i(x,y)] \qquad \text{[cyc/px]} \qquad 3.3$$

$$PSD(\xi,\eta) = |I(\xi,\eta)|^2 \qquad \text{[cyc/px]} \qquad 3.4$$

Where $i(x,y)$ is the 2D image taken by the sensors with x and y representing spatial values, and $I(\xi,\eta)$ is the 2D Fourier Transform of the image, where ξ and η are spatial frequencies in the x and y respectively. To find the 1D *PSD*, the azimuthal average of the 2D *PSD* is used. The 1D PSD shows the frequency content in each scene and the amplitude shows the strength of these frequencies. Since the scenes are resolution and FOV matched, this comparison gives direct insight into how the contrast affects the exact same frequencies passing through the different band systems. The same calibrated images are used in this analysis as the last. For the 1D PSD, the higher the amplitude passing through the system corresponds to higher differential ER and therefore higher contrast. The 1D PSD's plotted on a log scale are provided in Figure 3.10 for the VIS, NIR, SWIR and eSWIR bands are compared from the scenes in Figure 3.5-3.8 above.
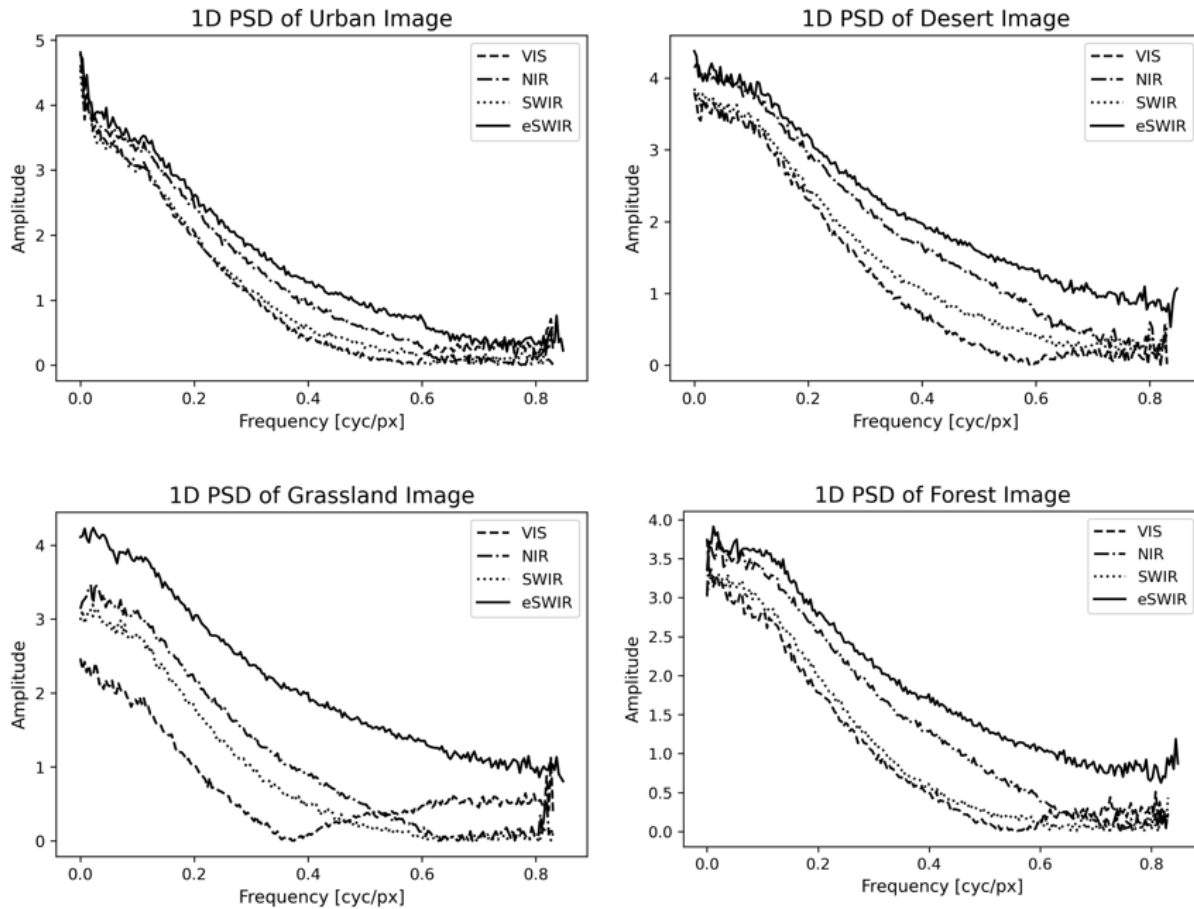
Figure 3.10: 1D PSD comparison for the four bands. The 1D PSD provided are calculated from Figures 3.5 –3.8. Amplitude is on a log scale.

Similar to the variance, the 1D PSD analysis shows that the eSWIR (in most cases) outperforms the other bands, meaning that eSWIR has more contrast than VIS, NIR, and SWIR. The same trends are seen in this analysis as well. The urban scenes have much closer amplitudes just like the variances ratio above and the grassland is much more favorable in the eSWIR over the other bands. A similar ratio comparison is shown in Table 3.5 as was done with the variances in Table 3.4. A single average 1D PSDs for each case (urban, desert, grassland, forest) is calculated, then integrated with respect to their amplitude which is a function of spatial frequency (equation 3.5).

$$\int A(v) \cdot dv \qquad [\text{cyc}^2/\text{px}^2] \qquad 3.5$$

Where A is the average amplitude of the 1D PSD's, a function of frequency v. The ratio

between eSWIR and the other bands from equation 3.5, again shows that eSWIR is favorable for

its frequency content within the imagery. We find the same trend that eSWIR is followed by NIR,

SWIR and VIS, in that order. At this point it is important to recall the MTFs of the four systems.

While the MTFs of the eSWIR, VIS and NIR and very well matched, the SWIR MTF's slightly

lower amplitude across all frequencies might influence its decreased PSD. However, based on

the variance and PSD amplitude, it would not be enough to overcome the NIR or eSWIR signals.

Table 3.5: Ratio of Integrated 1D PSD values. All values being over 1 means that the eSWIR is still the favorable band in terms of scene contrast.

1D PSD Ratio	Urban	Desert	Grassland	Wooded
eSWIR / VIS	1.94	2.67	5.16	2.96
eSWIR / NIR	1.40	1.50	1.90	1.38
eSWIR / SWIR	1.78	2.03	2.45	1.96
SWIR / VIS	1.09	1.31	2.11	1.51
SWIR / NIR	0.79	0.74	0.78	0.71
NIR / VIS	1.39	1.77	2.73	2.14

3.7) Discussion

The scene contrast study between VIS, NIR, SWIR and eSWIR shows that eSWIR is the

most favorable band in terms of ER contrast. For both the variance and 1D PSD comparisons, the

eSWIR band has a higher distribution of ER values, and higher amplitudes per frequency within

each scene. These analysis methods conclude that eSWIR has the highest contrast for the

reflective imaging bands. The next favorable band for contrast would be NIR, followed by SWIR

and then VIS. The NIR band in all cases has more contrast than the SWIR and VIS. The NIR could be used as a cheaper imaging option than eSWIR for lower cost platforms. The NIR contrast is not as great as eSWIR but the significant decrease in SWaP could but be a deciding factor to use a NIR sensor.

For mapping purposes, the eSWIR provides excellent scene contrast to identify objects of interest for correlating imagery to mapping databases. The detail between terrain features and buildings in the eSWIR provides greater opportunities for recognizing objects, especially in degraded visual environments. However, when targeting, the eSWIR's high contrast background could potentially be observed as clutter for automatic target recognition routines or human observers. The VIS and SWIR ER of vegetation is generally uniform, where the NIR and eSWIR show more variation between the plants. The SWIR band could potentially be favorable for targeting with its low background scene contrast and higher atmospheric transmission. If a low reflectivity target is placed in the generally higher reflectivity scenes of the SWIR, it would be easily identifiable with the uniform background.

A more in-depth quantification of the scene contrast can be calculated by measuring the spectral irradiance of the scenes, calibrating the scenes to reflectivity, and then calculating the photons per second that would be observed by the sensors. This method would be a useful comparison between the bands due to the lower irradiance on earth in normal daylight conditions in the longer wavelengths (Figure 3.11) [21].
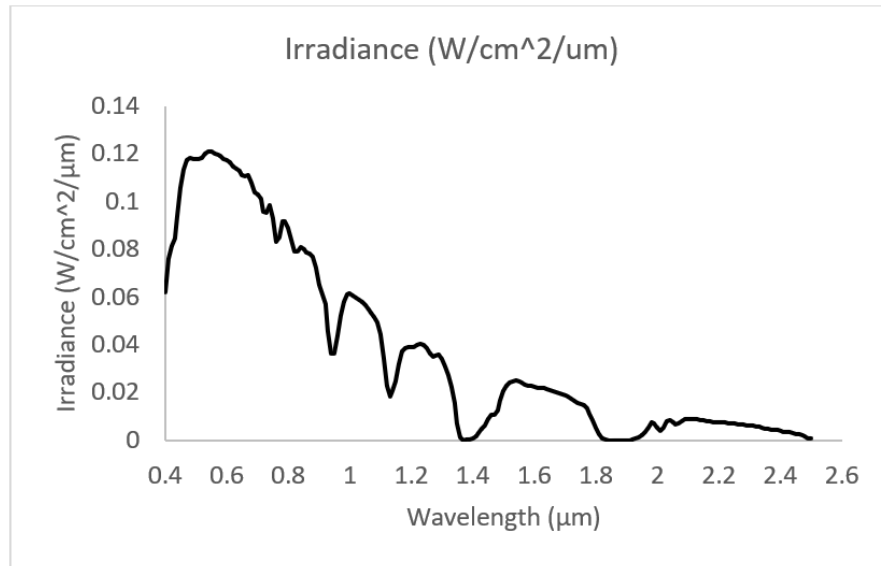
Figure 3.11: Spectral Solar Irradiance provided by MODTRAN 6. The atmosphere modelled was calculated with 23km visibility, Rural U.S. Standard Atmosphere.

During low light conditions, like days with full cloud cover, the extinction of light in the eSWIR is more noticeable than the other bands. This is because this band is already photon starved as seen in the solar irradiance curve. The decreased flux on a scene in the eSWIR compared to the other bands reduces the amount of light available for imaging. This could reduce the apparent contrast of the eSWIR more over the other bands during heavy cloud, dawn, or dusk conditions.

Other future work could include placing targets with known reflectance signatures within difference scenes with different average reflectivity and various amounts of clutter to show how the different bands perform. In a similar fashion, mapping imagery could be obtained in each of these four bands and compared to high resolution databases to find which band is able to identify the sensors position the best.

3.8) Conclusion

The equivalent reflectivity (ER) of urban and rural scenes is used to compare the contrast between VIS, NIR, SWIR and eSWIR. ER is a direct byproduct of the calibration process that normalizes each scene to a value that fairly analyzes these four bands. The VIS, NIR, SWIR and eSWIR sensors in this study are IFOV and FOV matched. This method allows the imagers to sample the same scene content as well as pass the same spatial frequencies through the sensor systems. The calibration procedure combined with the IFOV and FOV matched sensors gives each band the same opportunity for the rural and urban scene ER content to pass through the imaging system. The variance and 1D PSDs can now be used to calculate scene contrast from ER.

The calibrated scene variance and 1D PSDs conclude that the eSWIR band has the most contrast in all urban and rural cases. The eSWIR is then followed by NIR, SWIR and VIS in terms of scene contrast. For general mapping purposes, the eSWIR and NIR would be the more favorable bands to use with their higher contrast. However, this higher scene contrast could correlate to more background clutter for targeting purposes, negatively affecting performance. For targeting applications, SWIR and VIS provide more uniform backgrounds, potentially increasing the probability of detection, recognition, or identification of targets. In the same manner, this reduced VIS and SWIR contrast could decrease the detail for mapping purposes.

Chapter 4: Nighttime High Voltage Wire Avoidance for Pilotage Systems

This chapter is an amended version of the original manuscript:

Leslie, Patrick et al. "Mid-Wave and Long-Wave Infrared Signature Model and Measurement of Power Lines against Atmospheric Path Radiance." Optics express 30.1 (2022): 563-575. Print.

4.1) Overview

The signal to noise ratio and corresponding visibility of power cables as seen by military aircrafts is critical for crew safety. During low altitude operations, rotorcraft systems must be able to navigate these power lines during flight. Many of these military missions are flown at night which means the reflective bands including the visible, near infrared and short-wave infrared do not provide sufficient light. However, the emissive bands of the mid-wave infrared (MWIR) and long-wave infrared (LWIR) can be used to distinguish the location of these wires. LWIR sensors are typically used for pilotage applications. In both the LWIR and MWIR, the signal to noise depends on the wire emissivity and reflectivity as well as the ground and sky background path radiance. The signal to noise ratio is strongly dependent on the elevation of the viewing angle. In this paper, we model the signal to noise ratio as a function of elevation viewing angle using wire reflectivity and emissivity as well as MODTRAN calculations for path radiance. We also take MWIR and LWIR measurements to compare these two bands to the modelling results. We provide a summary of both model and measurements and make conclusions.

4.2) Introduction

The ability to see power cables for crew safety is vital. Out of all helicopter accidents, 5.5% of domestic accidents involved power lines between 1994 and 2002 [1]. From 1994 to 2018 there has been at least two wire strike accidents each year. While these percentages only show some of the accidents overall, the real cost involved are fatalities and damage. In the U.S. from 1994 to 2018, 33% of wire strike accidents resulted in at least one fatality and 34% of helicopters were completely destroyed with the rest sustaining heavy damage [2]. Shown with available data from 1994 to 2018, there were 214 wire strike accidents resulting in 124 fatalities due to helicopter wire strikes. Fatalities involving wires are much higher in comparison to other categories of crashes.

To combat the number of accidents and fatalities due to power lines two paths of technology developed. Wire Strike Protection Systems® are a passive technology that consist of a windshield deflector and an upper and lower wire cutter to avoid entanglement [2]. These systems are relatively low cost in comparison to active vision systems but can fail due to large diameter wires, slow speeds and if the wires do not contact the helicopter near the cutters. Vision systems on the other hand give the pilot an opportunity to detect the wire and evade it. During the day visible, near infrared and short-wave infrared sensors can assist pilots to visualize obstacles during flight. However, when flying at night only the emissive bands can aid in obstacle detection. FLIR and Lockheed-Martin both utilize the mid-wave infrared and the long-wave infrared in their electro-optical sensor systems for pilotage and targeting [3,4] These bands range from 3-5 μm and 8-14 μm respectively and are critical for identifying objects at night.

In this paper, a mathematical model is created to incorporate sky radiance, ground radiance, wire reflectivity, wire emissivity and temperature. From a radiometric point of view, this model is used to calculate the signal of the wire and the atmospheric path radiance in the MWIR and LWIR

resulting in a wire contrast radiance and contrast equivalent blackbody temperature (Figures 4.1a-4.1c). The model can predict for the two emissive bands (MWIR and LWIR) at which angle the wire is no longer be distinguishable from its background. The sky and ground radiance data for the model is provided by MODTRAN as well as experimental measurement data. The measurements taken are both of the average wire temperature and its background path radiance at each angle from 0 to 360° around the wire. The same data is taken in the LWIR and MWIR to determine the contrast of the wire to its background. Finally, the results provide for a comparison of wire contrast in the MWIR vs LWIR. The results also provide a deeper understanding of the zero contrast angles in the MWIR vs LWIR.

Figure 4.1. Power Lines in the LWIR. Figure 4.1a (left) shows the wires against a cold sky where the ground reflection makes the wires bright. Figure 4.1b (middle) shows where the wire radiance matches the sky path radiance (i.e., no contrast). Figure 4.1c (right) shows a look down where the wires are dark reflecting cold sky against a warmer ground background.

4.3) Background

Pilotage is an act of directing the movement of a vehicle by visual electronic observations of recognizable landmarks [5]. The electronics that make the visualization of the pilots' surroundings possible are mobility sensors. These sensors follow the pilot's line of sight and collect

more data from the environment than the pilot could naturally see, to make the best possible choices in operating the vehicle. One of the main uses for these sensors are nighttime operations of terrestrial or aerial vehicles to avoid objects that might not be visible by the pilot's unaided sight. Combat pilotage systems use image intensifiers and electron multiplying charge-coupled device (EMCCD) systems for low light imaging. MWIR or LWIR systems are used when there is negligible visible light. While MWIR systems have been used for pilotage, LWIR systems are much more common. The two LWIR systems used in pilotage are uncooled infrared (UCIR) and cryogenically cooled photon focal planes (e.g. either mercury-cadmium-telluride (MCT) or TypeII Superlattice). For high performance pilotage, cooled LWIR sensors are required.

For night pilotage, sensor materials that are sensitive to photons from the emissive bands were created for negligible visible light pilotage. The emissive bands collect photons from the radiation that is given off by an object's total energy. Current 3rd Generation FLIR Sensor Engines for US. Army systems incorporate both of these bands on a focal plane array [6]. The emission from these objects is determined by object emissivity and reflectivity, object temperature and ambient radiance. The implementation of these systems has proven to help in pilotage, especially at night, but metrics needed to be created to characterize how to determine if an object like a power line is even visible. The visibility depends not only on the performance of the sensor, but also the sensitivity and resolution of the sensor, the emissivity and reflectivity of the targets, like a wire, and also the background radiometry such as ground or sky radiance.

The Snellen ratio was created as a visual acuity test and is still used as a standard today for some tasks. This ratio tests the resolution of a person's vision and can interpret the limit of an individual's sight. With 20/20 being the average of all adults, most younger people, or those with good vision score around 20/16 to 20/12 with 20/12 corresponding to an angular resolution of 0.01

degrees or 0.6 arc minutes [7]. This acuity test can then be related to a displays device pixel ratio (DPR) to determine the upper limit of a sensor needed that will give no added benefit to the pilot. The relationship between visual acuity and contrast can also be measured with high contrast charts with a sinewave pattern [8]. The contrast threshold function (CTF) for human vision can also be used to determine a sensor CTF that is directly related to pilotage performance. This is a more recent metric associated with pilotage performance as developed by Vollmerhausen and Bui [9].

When creating pilotage systems, the resolution and signal to noise ratio of the camera and the display system must be able to create a clear image for the pilot to see. The camera and display that the observer uses to visualize objects both add blur to the overall system making it more difficult to distinguish the target. When imaging with the eye, the systems CTF becomes the CTF of the eye degraded by the blur and noise of this system. The noise of the signal is introduced by the photo-detection components and the blur of the signal comes from diffraction, aberrations, sensor array size, pixel pitch, the blur of the display and blur introduced by the eye itself. Other obscurants such as glare and weather conditions can also cause degradation of the contrast as well.

For target acquisition performance, the Target Task Performance (TTP) metric was created to quantify the quality of an image as a weighted integral over the spatial frequency of the ratio between signal and CTF. This metric can give a good representation of both well-sampled and under-sampled imagers and can predict the performance impact of frequency boost, colored noise, and other characteristics of modern images [9]. The TTP metric was later modified to provide estimates of pilotage performance. While the pilotage performance model relates the pilot's ability to maneuver the aircraft with various background contrast levels, it was never modified to predict the visibility of wires.

Pilotage is not the only industry that is interested in the visualization of power lines. Companies that build and manage the power lines use UAVs (unmanned aerial vehicle) for thermology to map potential system failures. These UAVs utilize automatic target detection software as well as both infrared and visible sensors to detect faults in wires, insulators, and other hardware [10]. Examples of these could be broken or rusted insulator chains, frayed or detached wires and rusted or broken attachment points. These faults can be identified from both the visual and infrared sensors on the UAV. The focus of the infrared sensors for power equipment thermology mapping is to detect spikes in temperatures of the power lines or other equipment which usually corresponds to a problem in the system.

4.4) Mathematical Model

The model that we develop is intended to implement measured and simulated atmospheres to predict the contrast between the average temperature of a wire and its background. The first step of the model is to match the field of view (FOV) and mainly the line of sight (LOS) of the scene in the LWIR and MWIR. At each angle from 0° (looking at the horizon) to 360°, the sky and ground radiance are measured, or simulated, and can be converted into equivalent black body temperature (Figure 4.2). These values are then used to both model the average temperature of the wire as well as the contrast of the wire to its background.
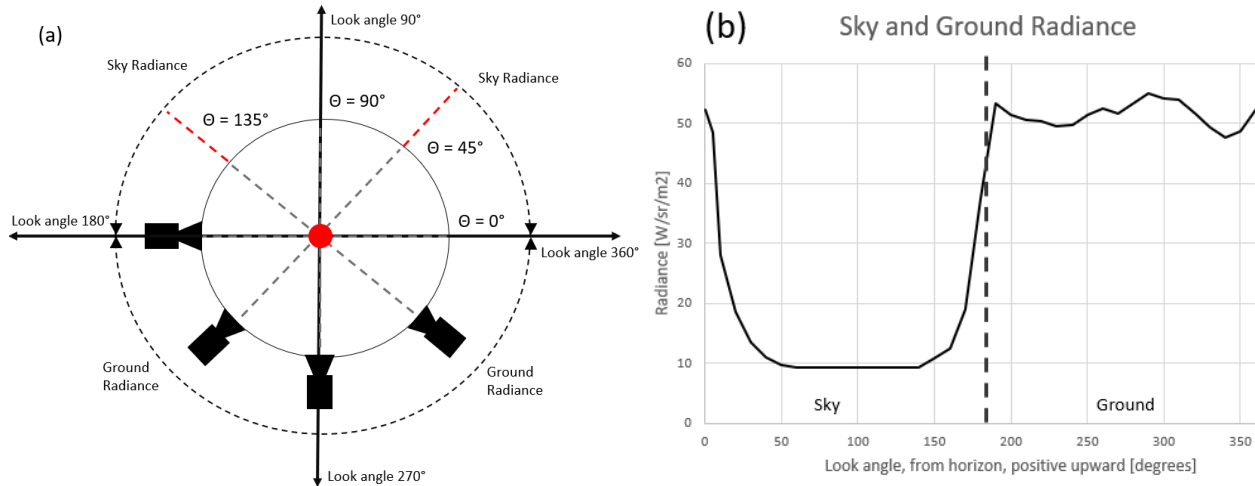
Figure 4.2: (a) Diagram of the orientation of the sensor when measuring the sky and ground radiance. As the sensor decreases in height around the center axis the angle increases. (b) LWIR sensor data of the sky radiance starting at the horizon and increasing in look angle. The dotted line in the middle is drawn at 180° Separating the sky radiance (left) and ground radiance (right). The measurements do not exceed 9.315 W/sr/m² (appx. -60°C) due to the limitations of the camera.

A multi-faceted surface shown in Figure 4.3, or "wire," is implemented in the center of the scene so that one pixel of the sensor can resolve the wire (i.e., a single detector angular subtense matches the dimension of diameter of the wire). Each facet of the wire reflects its corresponding sky or ground radiance for each angle around the wire. The radiance corresponding to the facet of each wire integrates resulting in an average wire temperature at each angle. The effective surface area of each facet of the wire as seen by the sensor is given as,

$$A_{EFF} = \text{Ldcos}(\alpha) \qquad [\text{m}^2] \qquad 4.1$$

where L is the length of the wire, d is the constant width of each facet that is sometimes limited by the azimuth detector angular subtense, dcos(α) is the width of a faceted segment from the point of view of the pixel and α is the angle at which that facet is tilted as seen by the sensor (Figure 4.3).
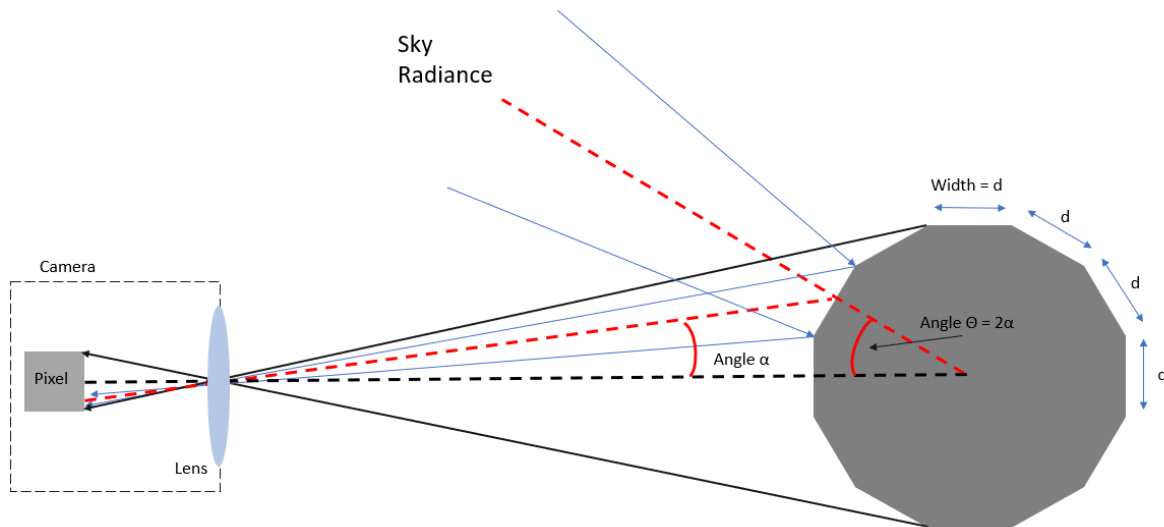
Figure 4.3: The faceted surface on the right is a simple representation of the modeled wire. The IFOV of the pixel is filled with the entire signal given by the wire. The area of each facet incorporated different portions of the sky and ground radiance that all average to give a single value on the detector. The angle that is reflected from the facet (θ) is two times the angle that the facet is to the direction of the sensor (α). Each of the facet faces are constant (d). Diffraction is ignored in the model.

The second step is to take the corresponding area radiance from the wire that is viewed by the sensor and integrate (sum) the intensity reflected from the wire. This integrates all of the wire facet radiances that are seen by the sensor and gives an overall intensity of the wire. This approach assuming a specular facet is provided by,

$$I_{REF} = \sum_{\alpha=\alpha_1}^{\alpha_n} \rho L_{ATM}(\theta = 2\alpha)Ldcos(\alpha) \qquad \text{[W/sr]} \qquad 4.2$$

$$I_{REF} = \sum_{\alpha} \rho L_{ATM}(2\alpha)Ldcos(\alpha) \qquad \text{[W/sr]} \qquad 4.3$$

where ρ is wire reflectivity, L_{ATM} is the radiance of the atmosphere [W/cm^2-sr], I_{REF} is the intensity [W/sr] and θ is the reflected atmosphere angle [deg]. The result of this summation is converted to

the average equivalent black body temperature that is reflected off the wire and viewed by the sensor at the different sensor angles. Next the emission (as opposed to reflection) from the wire at each facet needs to be incorporated. The intensity from emission is,

$$I_{EM} = \in L_{BBWire} Ldcos(\alpha) \qquad \text{[W/sr]} \qquad 4.4$$

where $\in$ is wire emissivity and L_{BBWire} is the equivalent black body temperature of the wire. The L_{BBWire} provides a Lambertian emissive. To find the total intensity of the wire the two equations are added.

$$I_{TOT} = \sum_\alpha \{\rho L_{ATM}(2\alpha) Ldcos(\alpha) + \in L_{BBWire} Ldcos(\alpha)\} \qquad \text{[W/sr]} \qquad 4.5$$

An assumption is made that the wire is a far distance from the detector that is collecting its signature on a single pixel. Then with small angle, α's (in radians) the facet can be written as $r_{WIRE}(d\alpha)$. The intensity is then given by

$$I_{TOT} = \sum_\alpha \{\rho L_{ATM}(2\alpha) Lcos(\alpha) r_{WIRE} d\alpha + \in L_{BBWire} Lcos(\alpha) r_{WIRE}(d\alpha)\} \quad \text{[W/sr]} \ 4.6$$

An integral is then created to summate the total intensity given by all facets of the wire,

$$I_{TOT} = \int_{\alpha=\frac{-\pi}{2}}^{\alpha=\frac{\pi}{2}} [\rho L_{ATM}(2\alpha) + \in L_{BBWire}] Lr_{WIRE}\cos(\alpha) d\alpha \qquad \text{[W/sr]} \ 4.7$$

Equation 4.7 assumes the reflected portion of the wire is specular. The reflected light is actually a condition of specular and Lambertian, or a bidirectional reflectance distribution function (BRDF) can be used. For the reflected component, $\rho L_{ATM}(2\alpha)$, a portion β is specular and a portion $(1-\beta)$ is Lambertian. So, the overall equation that includes reflection and emission as well as specular and Lambertian components of the reflected component is,

$$I_{TOT} = \int_{\frac{-\pi}{2}}^{\frac{\pi}{2}} \left\{ \rho \left[\beta L_{ATM}(2\alpha) + \frac{1-\beta}{2} \int_{2\alpha-\frac{\pi}{2}}^{2\alpha+\frac{\pi}{2}} \cos(\theta) L_{ATM}(\theta - 2\alpha) d\theta \right] + \in L_{BBWire} \right\} Lr_{WIRE}\cos(\alpha) d\alpha \ 4.8$$

The total intensity given fills the pixel of the sensor. The limit of the integral is spatially limited to a specified IFOV. This limit is given by the half of the wire the sensor can see from one side, which we limit as -π/2 to π/2. The power, in watts, on the IFOV of the detector is

$$P_{pixel} = I_{TOT} \frac{A_{sensor\ aperture}}{R^2} \qquad [\text{W}] \qquad 4.9$$

Where P is the power on the single pixel, A is the area of the sensor aperture [cm^2] and R is the distance from the sensor to the wire. This result is then graphed, comparing the average power on a pixel of the wire at each angle from 0-360° around the wire. Lastly the average equivalent blackbody temperature of the wire is subtracted from the equivalent blackbody temperature of the measured or simulated background at that same angle to compare the contrast of the two at each angle. Contrast can be provided in either radiance or equivalent blackbody temperature (which is a radiometric quantity).

4.5) Wire Measurements

A high voltage power line was cut at approximately one meter in length and used to take images for the average wire temperature data collection. The sensors used in this study were a FLIR T1020sc with a 28° FOV in the LWIR and a Telops M150 Spark with a 20° FOV in the MWIR. The measurements were taken after the sun had set to avoid any solar reflections that would be present in the 3-5µm range of our MWIR sensor. Solar loading of the atmosphere and reflections in that band does change the contrast of the wire as well as the path radiance of the sky and ground, particularly in the MWIR. To measure the wire at a constant distance and to avoid any thermal radiation from the sensor operator, an apparatus was made to hold the camera

at all 0 - 360° angles around the wire (Figure 4.4). By using an inclinometer on the arm of the apparatus that holds the sensor, each angle could be specifically set for increments of 10°. The length of the arm was made so the wire could be easily resolved by the camera as well as have sufficient background radiance data.

Figure 4.4: Apparatus which holds the either the LWIR sensor or MWIR sensor (pictured) which contains the wire in the middle of the rotational axis, an arm holding a sensor at a constant distance, an inclinometer on the arm and a large disc to clamp the arm in place.

Starting with the sensor looking at the horizon (0°) and decreasing the angle of the arm the bottom of the wire and the sky background radiance was measured first from angles 0 - 180°. This was followed by the top of the wire and the ground background radiance from 190 - 350°. To obtain the background path radiance, the equivalent blackbody temperature of the sky and ground

was taken at each of these angles in the middle of the FOV (next to the wire) for both the MWIR and LWIR sensors (Figure 4.5).
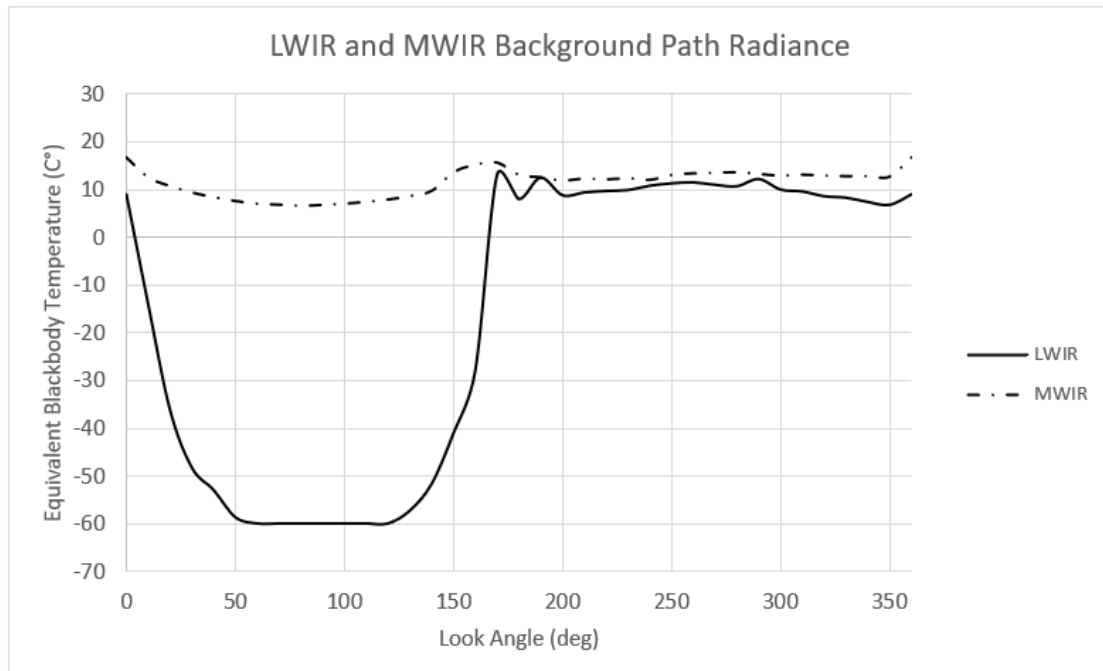
Figure 4.5: The measured sky and ground path radiance in both the MWIR and the LWIR. The LWIR equivalent blackbody temperature dramatically decreases as the sensor look angle increases towards the sky. The change in temperature for the MWIR cameras is much less. Again, the measurements do not exceed at -60C due to limitation of the LWIR camera.

At these same angles, the average wire equivalent temperature was recorded. The wire and background were clearly identified and integrated using the pixels on the wire and the background pixels near the wire. The integrated intensity of the wire was converted to a wire equivalent blackbody temperature for all angles from 0-360° in both the MWIR and the LWIR (Figure 4.6).

The increase in wire temperature while the camera was pointed towards the sky was due to the bottom of the wire reflecting the warm ground. Similarly, the decrease in temperature while

the camera was pointed towards the ground was due to the top of the wire reflecting the cold sky. The vast difference in fluctuation between the MWIR and the LWIR wire averages is attributed to their measured background. The steep difference in the background of the LWIR is easily seen from the wire averages from Figure 6 as well as the much smaller change in the MWIR from its background measurements. This fact results in a lower contrast between the background and the averaged wire signature for the MWIR than it does for the LWIR (Figure 4.7). By taking the differences between the background and the wire averages, the contrast between the two can be quantized. When the contrast is zero, the wire is indistinguishable from the background and as the angle increases or decreases from the axis, the contrast increases. In both cases the contrast reaches zero around the horizon but not at the same angle for the two bands.
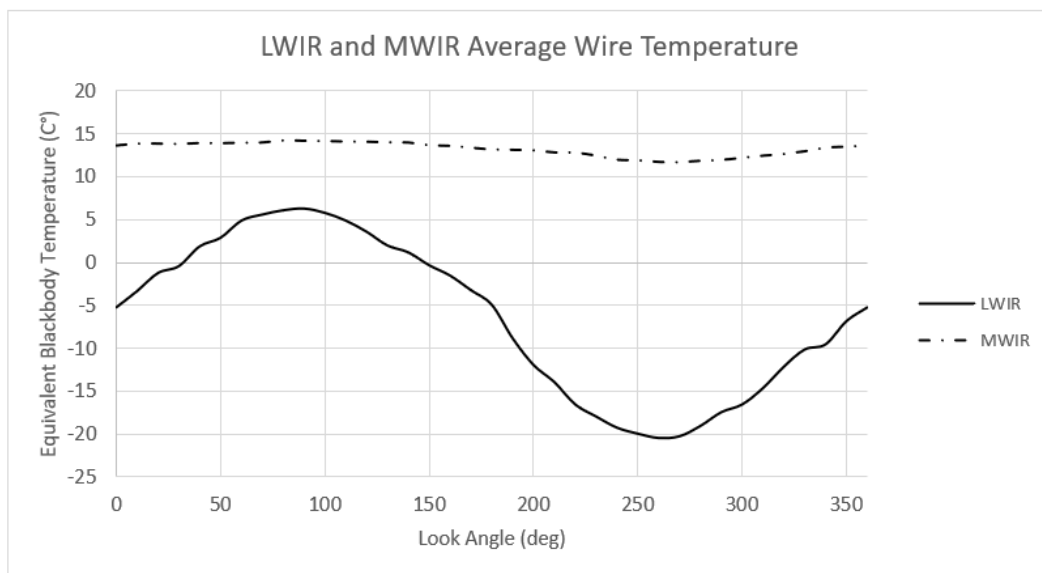
Figure 4.6: The LWIR and MWIR wire averages also have a large difference in their change in temperature. However, both of their positive and negative peaks happen when looking at the top and the bottom of the wire respectively (90° and 270°).
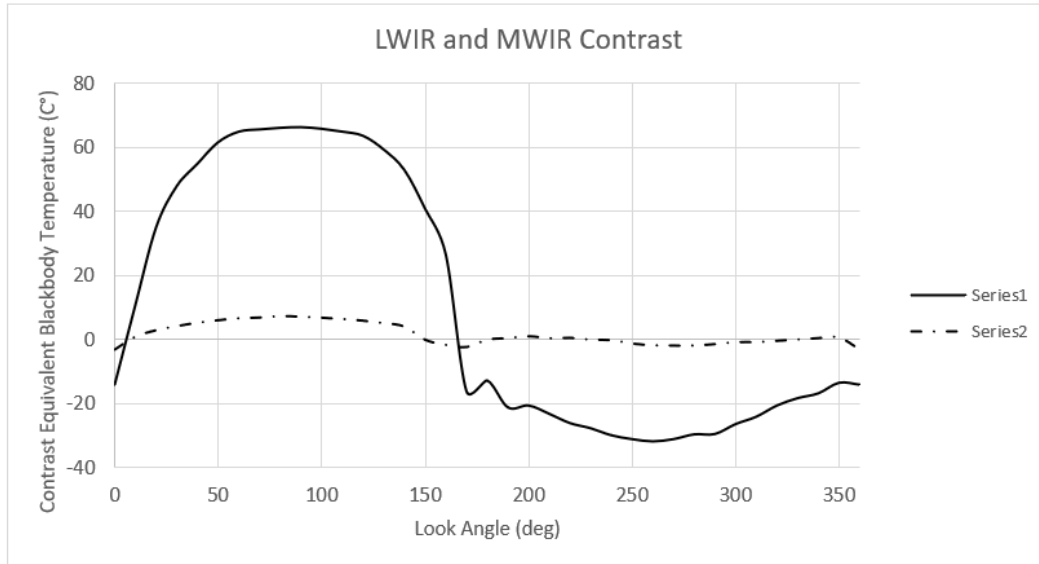
Figure 4.7: LWIR and MWIR contrast between the average wire temperature and the background temperature. The difference in these two values relate to the probability of identifying the wire in its scene and the greater the difference the more likelihood of detection.

4.6) Model Results with Measured Sky Radiance

To validate the simple model, the measured wire average temperature and background temperatures are linearly interpolated to two-degree increments. The limited radiance of the atmosphere in the LWIR was also interpolated to better match the average wire temperature. These temperatures are plotted with their corresponding angle from 0° to 360° to compare the modeled average wire temperature. The background temperatures of the atmosphere and ground are inserted into the model. Both the specular and Lambertian individual models are tested with varying emissivity to compare their results to the measured wire temperature (Figure 4.8).
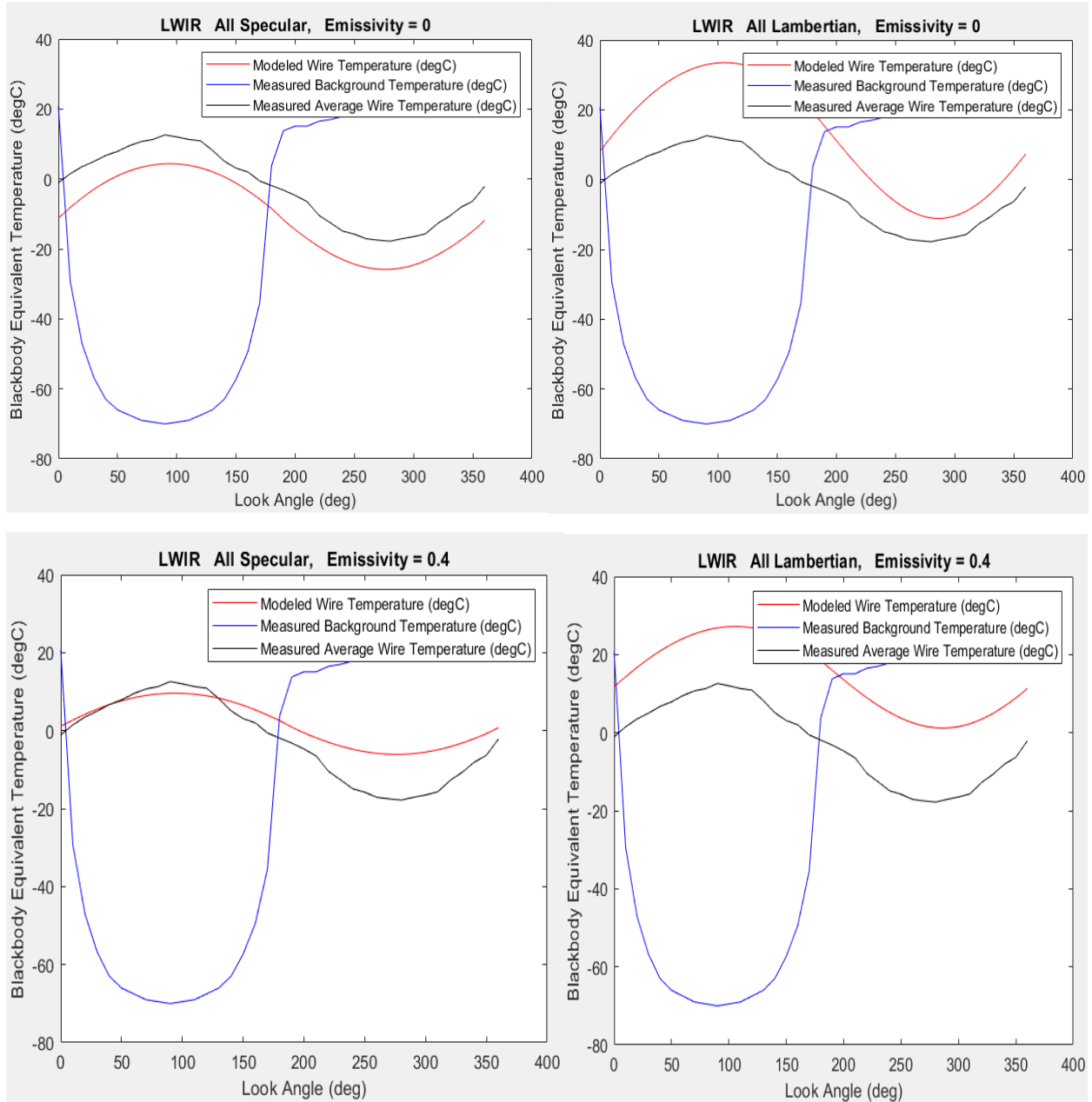
Figure 4.8: The four cases show the effects of the emissivity changes from 0 to 0.4. For these cases only specular or only Lambertian models were run with the respective emissivity's.

The specular model closely matches the amplitude of the measured wire, but its total average temperature is lower than the measured data. The increased emissivity causes a

reduction in the wires amplitude and increases the total wire average temperature. For the Lambertian model, the amplitude of the simulated wire temperature is larger compared to the wire temperature. Similarly, to the specular case, when the emissivity is increased the amplitude decreases but the average temperature is much higher.

By combining the specular and Lambertian models into one, the ratio of the Lambertian and specular model is linearly tuned by taking a percentage of each and adding the two cases together as described by equation 4.8. This phenomenon coincides with the bidirectional reflectance distribution function (BRDF) which characterizes materials through specular and diffuse reflectance measurements [11]. Most natural surfaces are neither 100% specular or Lambertian and generally are a combination of the two. There are different models to incorporate BRDF into measurements using complex functions but for this model a simple linear combination is used. In addition of the ratio of contribution from the two models, the emissivity is adjusted to match the amplitude of the measured wire average temperature.

In both the MWIR and LWIR cases the ratio and emissivity are tuned for two different measurements cases to ensure validity of the model and measurement (Figure 4.9). The emissivity's that allowed for the accurate validation of these models coincide with an emissivity of non-weathered aluminum. The measured emissivity's of unoxidized aluminum by thermal imager is around 0.1 [12]. The conductor used in the outer portion of high voltage power lines is aluminum with a steel core for strength [13].
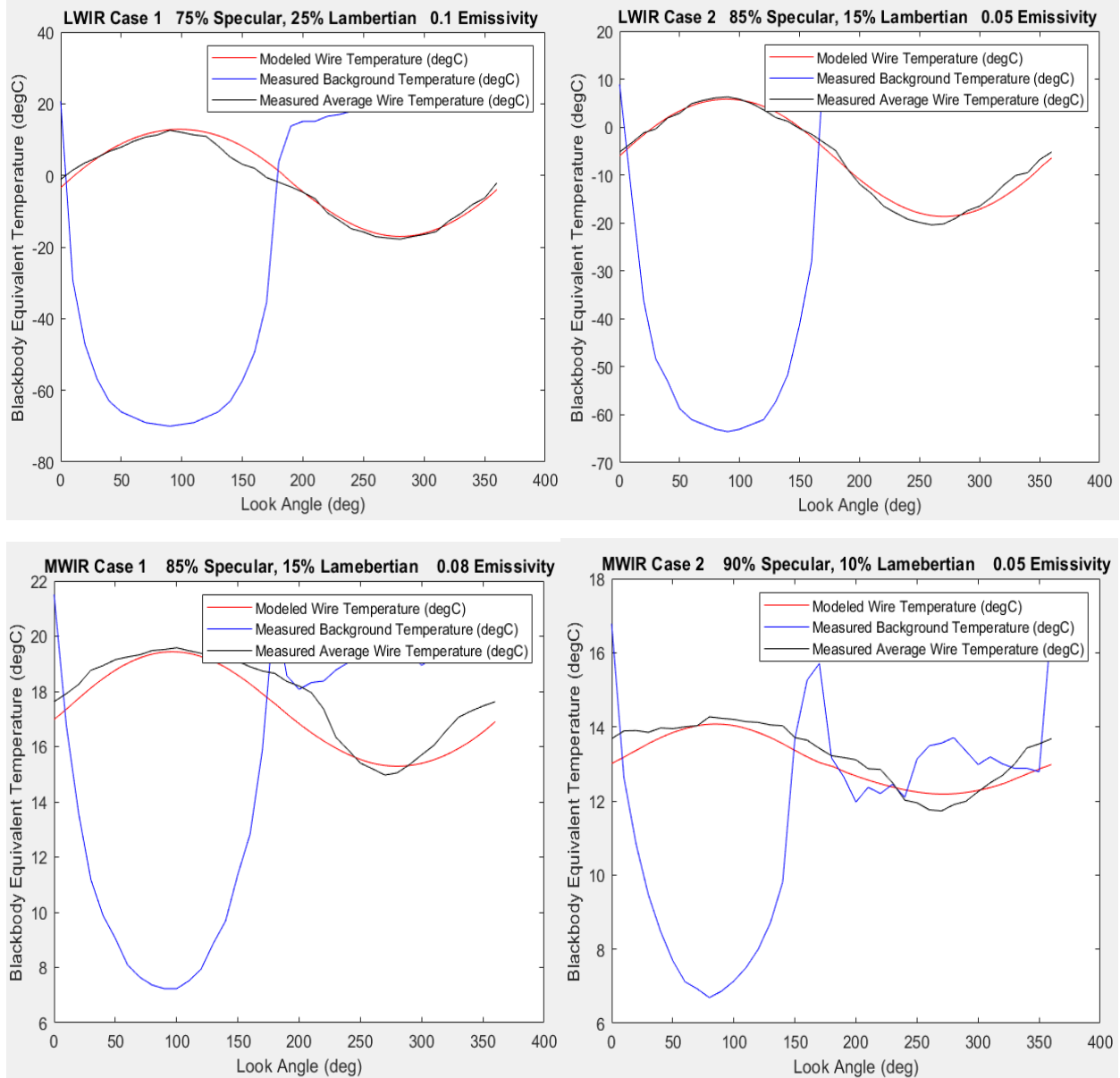
Figure 4.9: The measured and modeled wire average temperatures are plotted with their corresponding background temperatures. Case 1 and Case 2 measurements were taken on two different days after the sun had set to avoid large variation in the MWIR. The MWIR and LWIR data were taken at the same time during the measurements.

The BRDF model and emissivity of the aluminum wire for the LWIR accurately predicted the measured wire temperatures. Both the amplitude and average wire temperatures for all 360° were accurately predicted based on the combination model. The difference of emissivity's and the BRDF ratio between the two cases were reasonable and matched public data on wire surfaces. The model for the MWIR is harder to match due to its reflectivity and sensitivity. The wire measurements were taken at night to avoid major reflectivity readings that occur during the day in the MWIR but there can still be effects from the surroundings. The MWIR model does give a closely matched wire average temperature.

4.7) Modeled Results with Artic, US Standard, and Tropical Atmosphere

After the validation of the combined models with the LWIR and MWIR measurements, the model was used to predict the wire average temperatures in the MWIR and LWIR bands for other atmospheres. To avoid travelling all over the world to collect a variety of atmospheric data, MODTRAN generated atmospheres were used to generate the background path radiance used in the BRDF model. The model used the MODTRAN atmospheres to simulate the average wire temperature for all 360° and the contrast of the generated atmosphere and its associated wire. Six cases were modeled based on a few of the standard atmospheres that MODTRAN exports. U.S. Standard, Tropical and Artic path radiance were generated in both the LWIR and MWIR bands for a variety of concentration of aerosols and temperatures. The contrast of the MODTRAN background and the modeled wire temperatures were given for each band (Figure 4.10). An average ratio and emissivity for the BRDF model was used based on the two cases shown from Figure 4.9. The ratio for all cases was 80% specular and 20% Lambertian with an emissivity of 0.1.
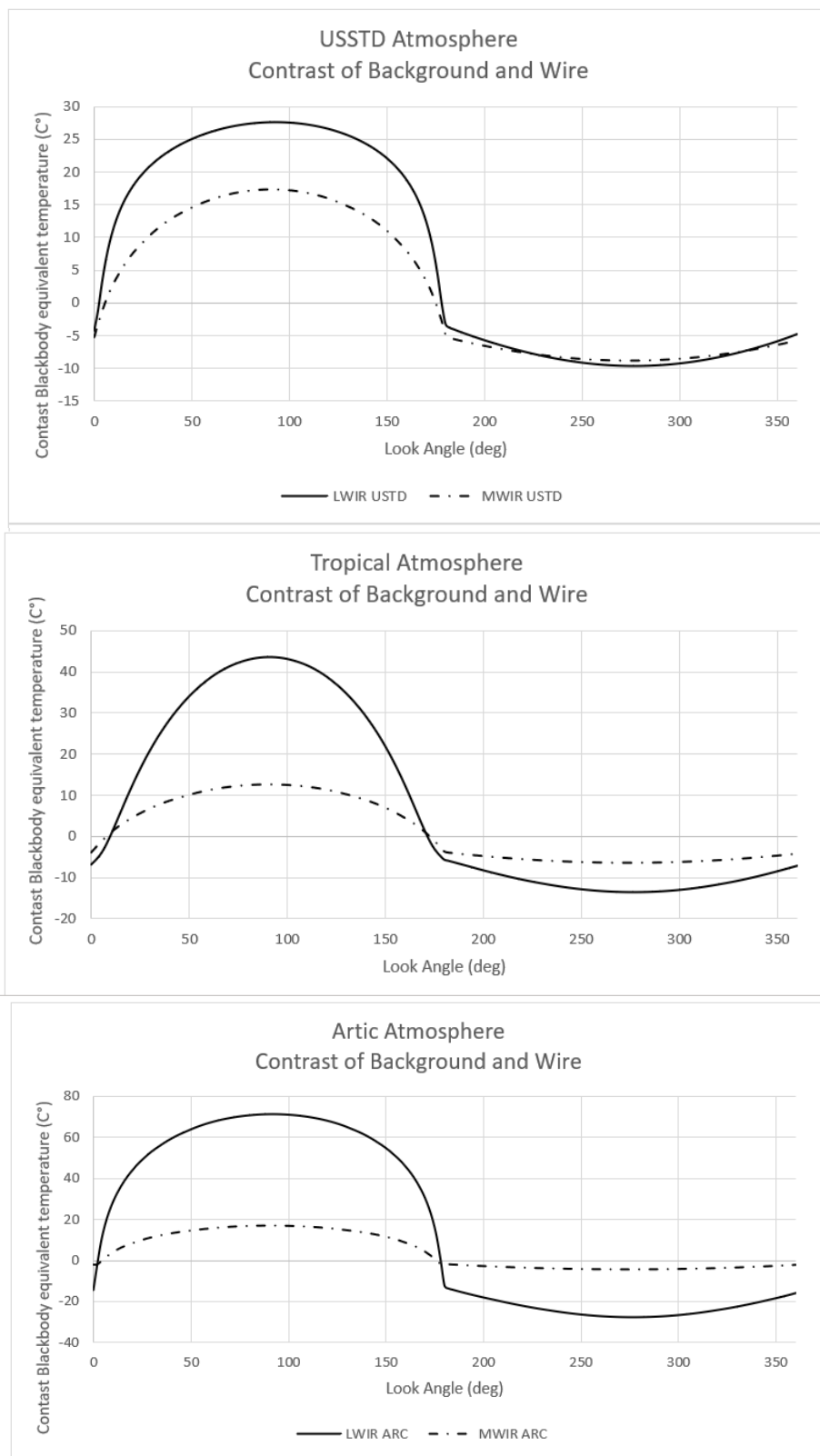
Figure 4.10: LWIR and MWIR contrast between the MODTRAN generated atmospheres and the simulated

average wire temperature given by the BRDF model.

The amount of contrast for each of the modeled atmospheres is significantly less in the MWIR than the LWIR. This was also seen in the measurements taken of the wire with the MWIR and LWIR sensors (Figure 4.7). Another important observation is that for each of the three atmospheres, the LWIR and MWIR contrast goes to zero at different look angles (Table 4.1). When the contrast is zero for one band, the temperature between the background and the wire in the other band is not and recorded in Table 4.1 as well. The lower of the two numbers would represent the minimum contrast that a dual band pilotage system for wire detection would have on the wire at all times in that environment.

Table 4.1: The angle at which the contrast in both the LWIR and MWIR goes to zero is seen to be different for every case in the modeled and measured atmospheres. The amount of contrast that the other band sees when the other is at zero is recorded and shown as well. The lowest contrast that would be always seen by a dual band wire detection system would be -0.67°C.

Atmosphere	Zero Contrast Angle LWIR (Degrees in Angle)	Zero Contrast Angle MWIR (Degrees in Angle)	MWIR Contrast when LWIR equals zero (Degrees in Temp)	LWIR Contrast when MWIR equals zero (Degrees in Temp)
US Standard	4.6 & 175.4	5.5 & 174.5	-0.75°C	-5.83°C
Tropical	9.5 & 171.5	8.0 & 172.0	-0.67°C	-1.7°C
Artic	2.3 & 176.7	4.4 & 175.6	-2.4°C	11°C

4.8) Discussion

For high power voltage line detection, the larger the contrast between the wire and the background, the higher probability there is for detection. For the MWIR and LWIR sensors, the LWIR provides significantly more contrast in all scenarios measured and modeled as seen in

Figures 4.7 and 4.9. The performance of the two bands is compared by the contrast in the LWIR vs the contrast in the MWIR for all modeled and measured scenarios (Figure 4.11). When the x-axis is crossed, this is when the contrast in the LWIR is zero and when the y-axis is cross this is when the MWIR is zero. Figure 4.11 also shows well again that there is no atmosphere in this paper where the contrast is zero at the same time. Figure 4.11 shows a 2 to 4 times higher contrast in the LWIR versus the MWIR depending on the atmospheric conditions. Also seen, is that when the MWIR sensor is looking down from above, the contrast of the ground and the wire can be zero at various angles besides just at the horizon, where the LWIR only has the two crossing points coinciding with the horizon.
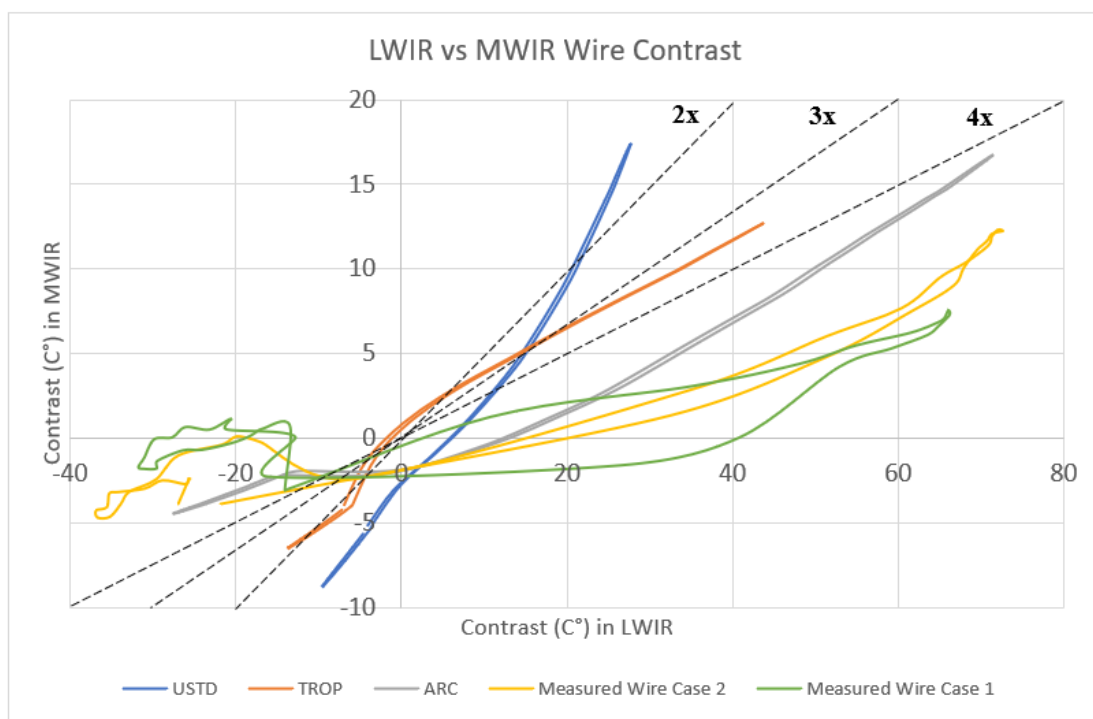
Figure 4.11: This graph plots LWIR contrast vs MWIR contrast to show the two to four times better performance given by the LWIR. MODTRAN atmospheres are very symmetric showing a small gap where the measured atmospheres have different contrast giving different crossing points.

4.9) Conclusion

Single band wire detection in pilotage is most effective with a LWIR sensor. The contrast that is achieved can be four times higher than that of the MWIR. The fact that in the MWIR the contrast when looking down at the wire could also be zero depending on your background would make the MWIR an unreliable band for a single band pilotage system.

The contrast angle in the MWIR and LWIR is zero when viewing the wire near the horizon angle for all modelled and measured cases. Since the contrast for each band does not reach zero at the same angle, a dual band wire detection system could be beneficial for wire visibility. Based on Table 1, there could be at least a half a degree of contrast for a dual band imager and increase the probability of never losing sight of them. Future work will determine how much contrast is needed to implement two bands on the same detection system and if the small contrast gain is enough to warrant the extra cost of the dual band sensor.

Future work for wire detection systems is to introduce new environmental factors and real-world scenarios. New environmental factors will include cloud cover and the effects on path radiance, contrast, and average wire temperature. Daytime wire detection will also be studied as a separate case due to the reflectivity in the MWIR, solar loading of the sky and sun position. Other effects to study, that a pilotage system would encounter in the real world, are the phasing effects of the wire sagging between the wire poles and when the wire becomes resolved versus unresolved due to distance.

Chapter 5: Drone Integrated Multicamera Systems for Wide Area Coverage Search

This chapter is an amended version of the original manuscript:

Leslie, Patrick et al. "Visible, SWIR, and LWIR Drone Wide Area Coverage Sensor Systems." Optical engineering 63.2 (2024): Optical engineering, 2024-02, Vol.63 (2). Print.

5.1) Overview

Small Unmanned Aerial Systems (sUAS) provide a versatile platform for covering large areas quickly. By adding sensors to drones, imagery of large areas can be taken for a variety of applications. Traditionally, single fixed staring systems or gimballed sensors are used to take this imagery. Both options require a compromise between field of view (FOV), resolution, scanning speed, and flight path to properly perform the desired task. If more than one sensor is integrated onto the drone, a wide FOV can be covered without a scanning gimbal and obtain higher resolution than a traditional wide FOV staring system. Presented is a multi-camera design approach based on a constraining ground sample distance (GSD) for a wide area coverage (WAC) system. This design approach can be used for any imaging bands. A figure of merit (*FoM*) is derived to quantify and compare the performance of the WAC systems in the visible (0.4-0.7um), short wave infrared (1.0-1.7um) and longwave infrared (8-14um) for both good and bad visibility conditions. The performance of three optimized and fabricated WAC systems are compared and tested through the *FoM* and flight testing.

5.2) Introduction

Aerial photography from drones is a convenient way to map an area or detect / discriminate objects from a distant vantage point. With cheap commercial drones and their visible sensors, imagery of an area is readily obtainable. Some commercially available drones even have small gimbals to allow for quick scanning of areas to increase the versatility of the sensor in flight. However, the quality of the image is directly related to altitude of the drone and the distance of the objects from it. To image a large area quickly, both high resolution and a large FOV are needed. To optimize the tradeoff between resolution and FOV for a single sensor, gimbals or multiple cameras[1] can be used to increase the total FOV of the platform, while maintaining high resolution images. The advantage to using multiple cameras over a gimbal is that there are no moving parts, and the optics can be changed for each camera to increase the resolution of images at further distances.

Using sUAS for quick, wide area coverage (WAC) mapping is becoming increasingly popular[2]. Implementing multi-camera systems for target detection and recognition purposes can have a large benefit over gimbal systems[3]. The probability of recognizing an object is calculated by using the targeting task performance (TTP) metric[4]. The probability of recognition (P(rec)) increases as the number of pixels on target increases. Similarly, P(rec) decreases as range increases from the sensor. For very wide FOV systems, P(rec) decreases rapidly with range, making gimbal scanning during WAC search for targets more difficult. Using multi-camera systems with a variety of focal length optics maintains a high P(rec) for targets at long ranges. By optimizing the design process for these multi-camera systems for target discrimination, the modeling of these systems becomes easy. These systems can be designed for a variety of wavelengths using the same process. The benefits of different wavelengths can be exploited to

increase the performance of these systems. As an example, one benefit of the longer infrared wavelengths over visible is a smaller decrease in P(rec) when degraded visual environments (DVE) are present in a scene.

5.3) WAC Optimization Process

Our first step to understanding multicamera design and creating WAC systems is to combine three equations. The final derived equation calculates the FOV of a sensor, based on the sensor format, aircraft altitude, and ground sample distance (GSD).[5] As each sensor is added to the overall system, the previous sensor's FOV needs to be considered. Connecting these equations uses the GSD as a limiting resolution for the imaging system. The GSD for a system is found by determining how many pixels on a certain target an observer needs to discriminate or recognize it. A limiting GSD_{Max} for targeting can be determined from a few metrics, including NIIRS rating[6], Johnson's Criteria[7] or a V50 number[4]. Whichever metric is used to determine GSD_{Max} should also be used in the Figure of Merit (*FoM*) analysis later. Throughout this paper, only V50 related values are used.

Using Figure 5.1 as a guide, the first equation provides a link between the resolution requirements of the system and the instantaneous field of view (IFOV) of the system.

$$GSD_{Max} = IFOV_1 \cdot R_1 \qquad \text{[cm]} \qquad 5.1$$

GSD_{Max} is the determined limiting GSD of the system and R_1 is the range associated with that GSD.
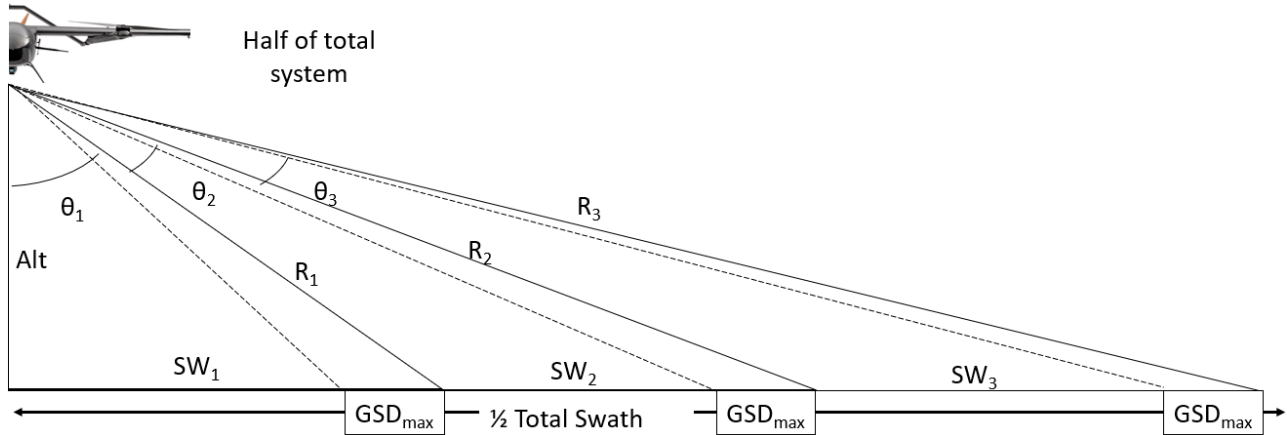
Figure 5.1: Variables associated with the creation of a 6 camera WAC system.

R_1 and GSD_{Max} for this optimization process are found in the Night Vision Integrated

Performance Model (NV-IPM) at a P(rec) = 80%, for a target with a characteristic dimension of

3.1m. The values of P(rec) = 80% and a 3.1m target are typical specifications for using the

Targeting Task Performance (TTP) metric[4] to recognize vehicles for military applications.

The next equation relates the altitude of the aircraft to the range and FOV of the sensor.

$$Alt = R_1 \cdot cos\theta_1 \qquad\qquad \text{[cm]} \qquad 5.2$$

Alt is the operation altitude of the aircraft and θ_1 is the FOV of the first sensor. In this geometry,

it is assumed that the closer edge of the FOV creates a right angle with the ground (See Figure

5.1 for context of θ_1). If there are an odd number of sensors being used for the WAC

optimization process, the first FOV is halved to create the correct geometry.

The last equation ties the previous two equations together, relating the IFOV of the sensor

system to the number of detectors in the focal plane array and the FOV.

$$IFOV_1 = \frac{\theta_1}{N_{det}} \qquad\qquad \text{[mrad]} \qquad 5.3$$

The only new variable introduced here is N_{det} which is the number of detectors in the focal plane array in the cross-flight path direction. These three equations can now be manipulated to create an optimization equation for creating WAC systems.

For the first sensor, in an even number of camera system, the FOV of the first lens is found by the constraining GSD, operating altitude, and format of the detector.

$$\frac{\theta_1}{cos\theta_1} = \frac{GSD_{max} \cdot N_{det}}{Alt} \qquad 5.4$$

The right-hand side of the equation results in a constant that is the same for every FOV calculated in the multi-camera system. To solve for θ_1, an iterative computational method is used. A range of values are inserted for θ_1 until it exactly matches the calculated constant. A graphical representation of this is shown in Figure 5.2. After the FOV is found, the correct focal length lens can be chosen for the first sensor.
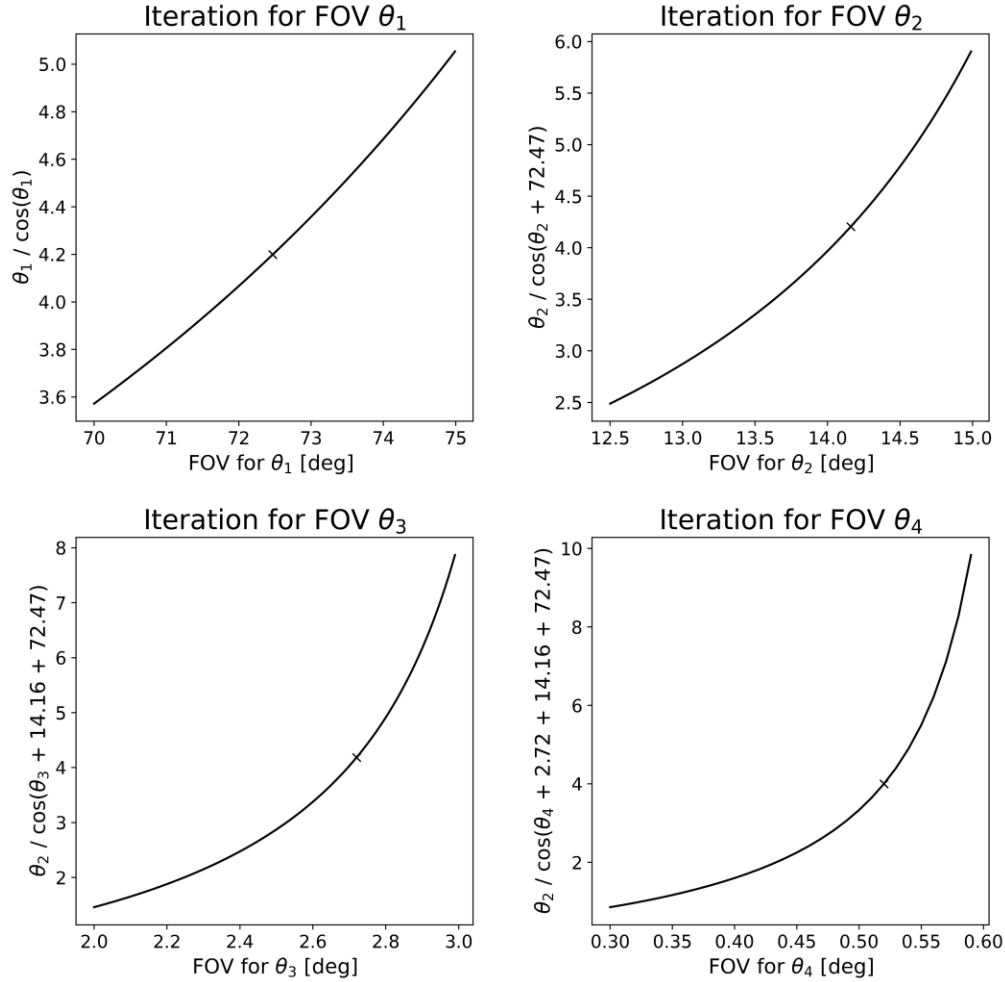
Figure 5.2: Example of the iterative method used to find the FOV for each sensor system. A *GSD* of 0.25m, N_{det} = 2048 and *Alt* = 121.9m result in a constant of 4.20016. The four resulting FOV's are 72.47°, 14.16°, 2.72° and 0.52°.

For each sequential sensor that is added to the system, the previous FOVs need to be accounted for in the cosine term. This maintains the correct geometry for the WAC design.

$$\frac{\theta_n}{\cos\left(\sum_{k=1}^{n}\theta_k\right)} = \frac{GSD_{max} \cdot N_{det}}{Alt} \qquad 5.5$$

In this case *n* is the current sensor FOV being calculated, and *k* is the first sensor FOV. For each sensor added, the iterative method used needs to take all previous FOV's into account (Figure 5.1

& 5.2). After all the desired cameras are added, equations 5.6 and 5.7 define the total system

FOV and swath width on the ground of the WAC system designed. The definition of swath width

for WAC systems is the total on-axis distance of the ground that is imaged under the drone

platform.

$$FOV_{tot} = 2 \cdot \sum_{k}^{n} \theta_k \qquad \text{[deg]} \qquad 5.6$$

$$SW_{tot} = 2 \cdot Alt \cdot \tan\left(\sum_{k}^{n} \theta_k\right) \qquad \text{[m]} \qquad 5.7$$

This process is simplified into a flow chart in Figure 5.3 that depicts the optimized WAC design

process. A comparison of optimized VIS, SWIR and LWIR 8 camera WAC systems is used in

this paper to show the different performance of the bands using this method.
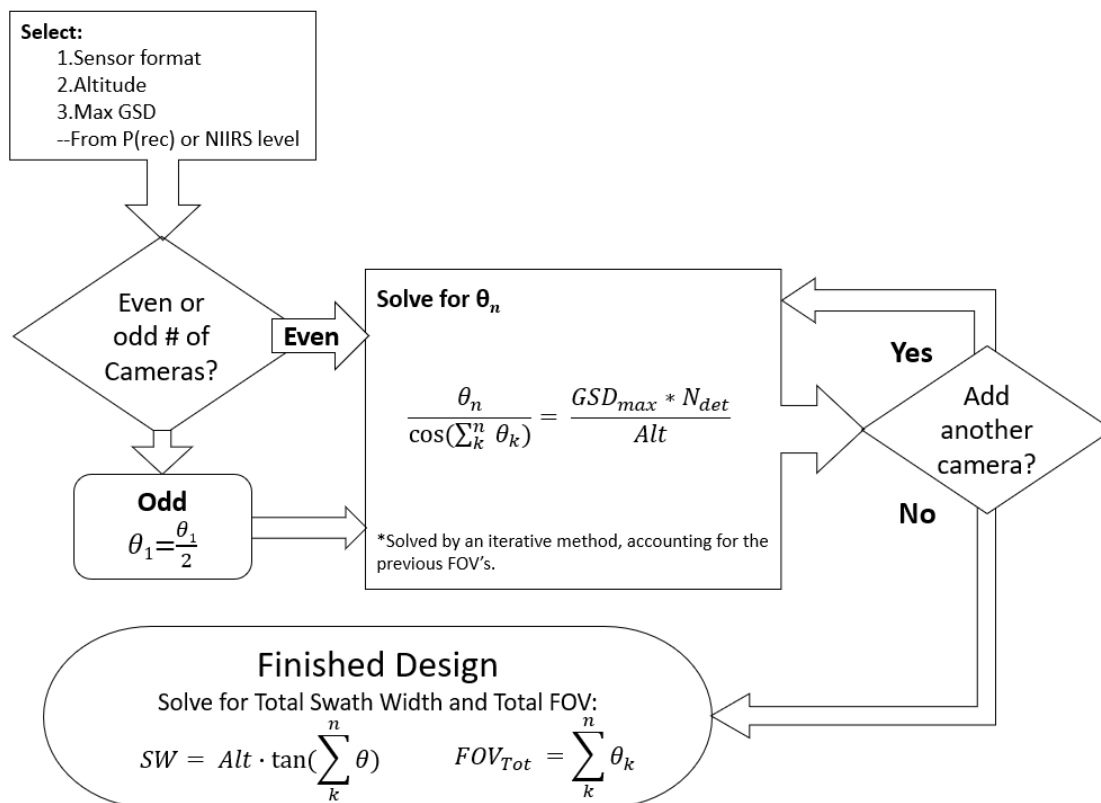
Figure 5.3: Flow chart of the WAC optimization process

5.4) Figure of Merit (FoM) Definition

Comparing single camera system performance is standard practice for system design. Modeling softwares, such as NVIPM, are used to calculate the probabilities of detection, recognition, and identification versus range for many scenarios. A direct comparison of multicamera systems for WAC has not been made yet. To do this, a figure of merit (*FoM*) is created to directly compare all camera performance in their respective orientations with a certain aircraft velocity. The cut off P(rec) = 80% is used again since it is a typical specification for military systems. Depending on the application and performance required of the system, another probability cut off can be used. The sensor system performance for each FOV is calculated with the TTP metric[4] and is also used to calculate the *FoM* values.

$$FoM = \int_{-\infty}^{\infty} P(rec)|_{P(rec)>0.8} \cdot v \, dx \qquad [\text{km}^2/\text{h}] \qquad 5.8$$

In the *FoM,* the P(rec) is the probability of recognition for a given target as a function of range. If a WAC system is being designed for probability of detection or identification, these values can replace P(rec). The *FoM* takes the integral of all probabilities in all multi-camera's FOVs that are greater than P(rec) = 80% with respect to *dx* in meters. It then multiplies this value by the velocity at which the aircraft is flying, *v*. The probability curves for each sensor are created in NVIPM in their respective bands. The *FoM* can then directly compare the performance of each WAC system, even for different bands, with a single value. The *FoM* is an area coverage rate at which targets can be discriminated against with a specified cut-off probability.

5.5) An Optimized FoM Comparison

The *FoM* is used to compare the performance of three 8-camera WAC systems designed in the VIS, SWIR and LWIR. These theoretical systems are used to compare the imaging bands directly to show the utility of the *FoM*. The theoretical systems designed are not limited by the availability of focal planes, lenses or cost. For single camera systems, the longer wavelengths perform better through longer atmospheric paths and degraded visual environments. To show that the *FoM* will have the same outcome, three identical systems that essentially only differ by wavelength are created and analyzed.

Typical sensor parameters are used in NVIPM to create realistic models of the VIS, SWIR and LWIR WAC systems. The base cameras used for the analysis are a FLIR Boson 640, Allied Vision Alvium VSWIR 1800 U-130 and a FLIR Blackfly CMOS sensor. The three parameters that were set equal to compare each band were the format sizes, F/# and limiting GSD_{Max}. Each model focal plane has 2048x2048 pixels and each lens is set to F/1 to achieve the same light collecting capabilities while avoiding diffraction limited cases. The limiting GSD for each system was set to 25cm to ensure the same area covered in each WAC FOV. The round 25cm GSD value is chosen because it is close to the GSD needed to recognize targets around 3.1m for these theoretical systems in each band.

Formatting the focal plane to be equal allows for realistic pixel pitches to be used for the reflective and emissive band sensors. The IFOV of the system is matched with different focal length lenses so the FOVs and GSDs will then be closely matched for a direct system comparison. A pixel pitch of 5 microns is used for the SWIR and VIS while a pixel pitch of 12 microns is used for the LWIR. Each WAC camera system is modeled as an 8-camera system to cover as much swath below the operation altitude as possible. Table 1 shows sensor and lens

details for comparing the system performances. While these apertures at F/1 are unrealizable, especially in the LWIR, they are used strictly for performance comparison of the bands.

Table 5.1: Information used to model the camera systems in NVIPM to compare the band performance of the same system.

		VIS	SWIR	LWIR
Format	[HxV]	2048 x 2048	2048 x 2048	2048 x 2048
PxPitch	[um]	5	5	12
System F/#		1	1	1
Limiting GSD	[cm]	25	25	25
Camera 1 FOV	[deg]	72.47	72.47	72.43
Camera 2 FOV	[deg]	14.16	14.16	14.18
Camera 3 FOV	[deg]	2.72	2.72	2.74
Camera 4 FOV	[deg]	0.52	0.52	0.53
Tot. 8 Cam. FOV	[deg]	179.74	179.74	179.75
Camera 1 FL	[mm]	7	7	16.78
Camera 2 FL	[mm]	41	41	98.8
Camera 3 FL	[mm]	213.75	213.75	514.5
Camera 4 FL	[mm]	1111.1	1111.1	2667

Each of the systems are modeled in NVIPM and the performance from the near side of each FOV to its further edge is calculated. Figure 5.3 shows the on-axis probability of recognition for each system. The ideal case of 23km visibility is used to create and optimize these systems. For the same systems, the 5km visibility performance cases show the degradation differences in the three bands. Using these probabilities, a *FoM* for each band in the 23km and 5km atmospheres are calculated. A velocity of 17.9 m/s or 40 mph is used. This velocity is the cruise speed of drones available for WAC system type payloads. Table 5.2 shows the *FoM's* for the different bands and how they compare in the two environments.

Table 5.2: Results of using the *FoM* for all bands in 23km and 5km visibility. Calculated is also the total swath width covered within the 25cm GSD requirement for each FOV. *The swath width for SWIR is constraint for 23km as the tangent function goes to infinity at 90 degrees.

	8 VIS	8 SWIR	8 LWIR
23km FoM [km²/h]	2,572.1	4,048.9	4,181.5
23km Total Swath[m]	18,769	30,000*	27,699.7
23km Total FOV [deg]	179.75	179.75	179.75
5km FoM [km²/h]	522.75	1,817.6	3,556.8
5km Total Swath [m]	3,848.1	13,394.5	22,949.7
5km Total FOV [deg]	176.4	178.9	179.4

The *FoM* of these optimized systems show that in both the 23km case and the 5km case, the atmosphere favors the longer wavelengths. The longer wavelengths have better transmission through the atmosphere and much less path radiance, especially in the DVE case. In the 5km visibility case, the VIS performance is around a fifth of optimal conditions while the SWIR is about a half. The ground coverage due to this degradation reduces in the same manner, increasing the number of passes a drone would have to cover an area to find a target. This analysis shows that the *FoM* works as expected, predicting better performance for longer wavelengths in similarly designed systems.
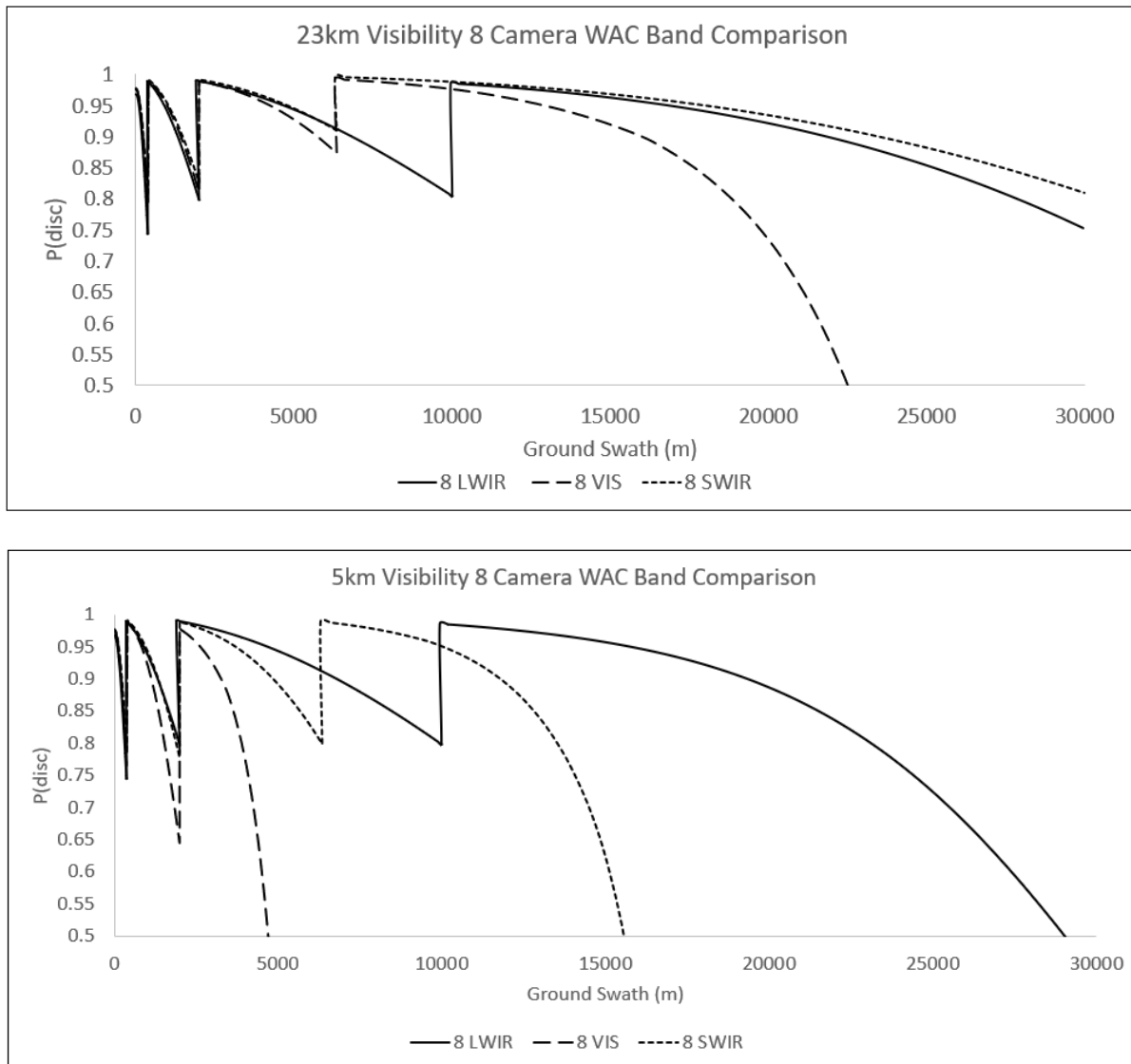
Figure 5.3: On axis probabilities for 23km and 5km visibility conditions for the 8 camera LWIR, SWIR and VIS systems. The jump from low probability to high probability occurs when the next FOV takes over.

5.6) Fabricated WAC Systems

Using the optimization process a VIS, SWIR and LWIR system are designed to fly at an altitude of 121.9 meters (400ft or the FAA operational limit under Part 107). At this altitude the P(disc) = 80% range corresponds to approximately 25cm GSD but now varies per wavelength.

The number of cameras used to fabricate each system mostly depends on the costs associated with the different bands. Due to limited focal plane formats and lens availability, the WAC camera systems were optimized to off-the-shelf sensors and lenses.

Three designs are made and fabricated including a 6-camera VIS system, a 4-camera SWIR system, and a 4-camera LWIR system (Figure 5.4). The specifications of these systems can be found in Table 5.3 which includes the sensors, lenses, FOVs, swath widths and total system coverage within the limiting GSD. Only half of each system is shown since each side of the drone has the same set of cameras and orientations. The on-axis probability of detection is plotted for each camera system in Figure 5.5. Again, where the first system drops to P(disc) ~ 80% is where the next FOV system takes over and a jump in probability is observed.

Table 5.3: Breakdown of the sensors and optics used for the fabricated WAC systems. Their modeled ground covered is also included to show their area coverage performance.

6 Visible System			
Sensors	Allied Vision Alvium 511m	FLIR BFS-U3-31S4M	FLIR BFS-U3-31S4M
Format [HxV]	2464 x 2064	2048 x 1536	2048 x 1536
PxPitch [um]	2.74	3.45	3.45
Hoz. FOV [deg]	73.75	11.53	5.39
EFL [mm]	4.5	35	75
F/#	1.8	2.0	3.9
Hoz. Ground Swath [m]	415	1,050	3,026
Swath in GSD limit [m]	9,008 (both sides)		
4 SWIR System			
Sensors	Allied Vision Alvium 1800 U130	Allied Vision Alvium 1800 U130	-
Format [HxV]	1296 x 1032	1296 x 1032	-
PxPitch [um]	5	5	-
Hoz. FOV [deg]	61.9	21.0	-
EFL [mm]	5.4	17.5	-
F/#	2.5	2.5	-
Hoz. Ground Swath [m]	227	745	-
Swath in GSD limit [m]	1,944 (both sides)		

4 LWIR System			
Sensors	FLIR Boson640	FLIR Boson640	-
Format [HxV]	640 x 512	640 x 512	-
PxPitch [um]	12	12	-
Hoz. FOV [deg]	47.6	24.1	-
EFL [mm]	8.7	18	-
F/#	1	1	-
Hoz. Ground Swath [m]	132	234	-
Swath in GSD limit [m]	732 (both sides)		

Figure 5.4: WAC systems in their custom housings attached to an Event38 E400 VTOL drone. The 6-Camera visible is on the left, the 4-camera SWIR is in the center and the 4-camera LWIR is on the right.

The visible system covers more area for two reasons. The first is that 6 cameras are used over the other 4 camera systems. The reason that the first camera in the visible system images more ground than the total SWIR and LWIR systems coverage is due to its larger focal plane format and smaller pixels.

Another noticeable artifact of off the shelf formats and lenses, is that due to their availability, the P(disc) ≥ 80% cut off for GSD cannot always be met. In the first LWIR's case, the best option was to dip just below the 80% cut off with the larger FOV lens, rather than only covering half the amount of ground under the aircraft. In the case of the second VIS camera, there was a large gap between the available 25mm and 35mm lenses for that format. Instead of

losing resolution due to the 25mm lens, a 35mm lens was the best compromise for this system. Based on all surveyed options for lenses and sensors, these are the best optimized systems that are created with the budget for using available lenses and sensors for these systems.
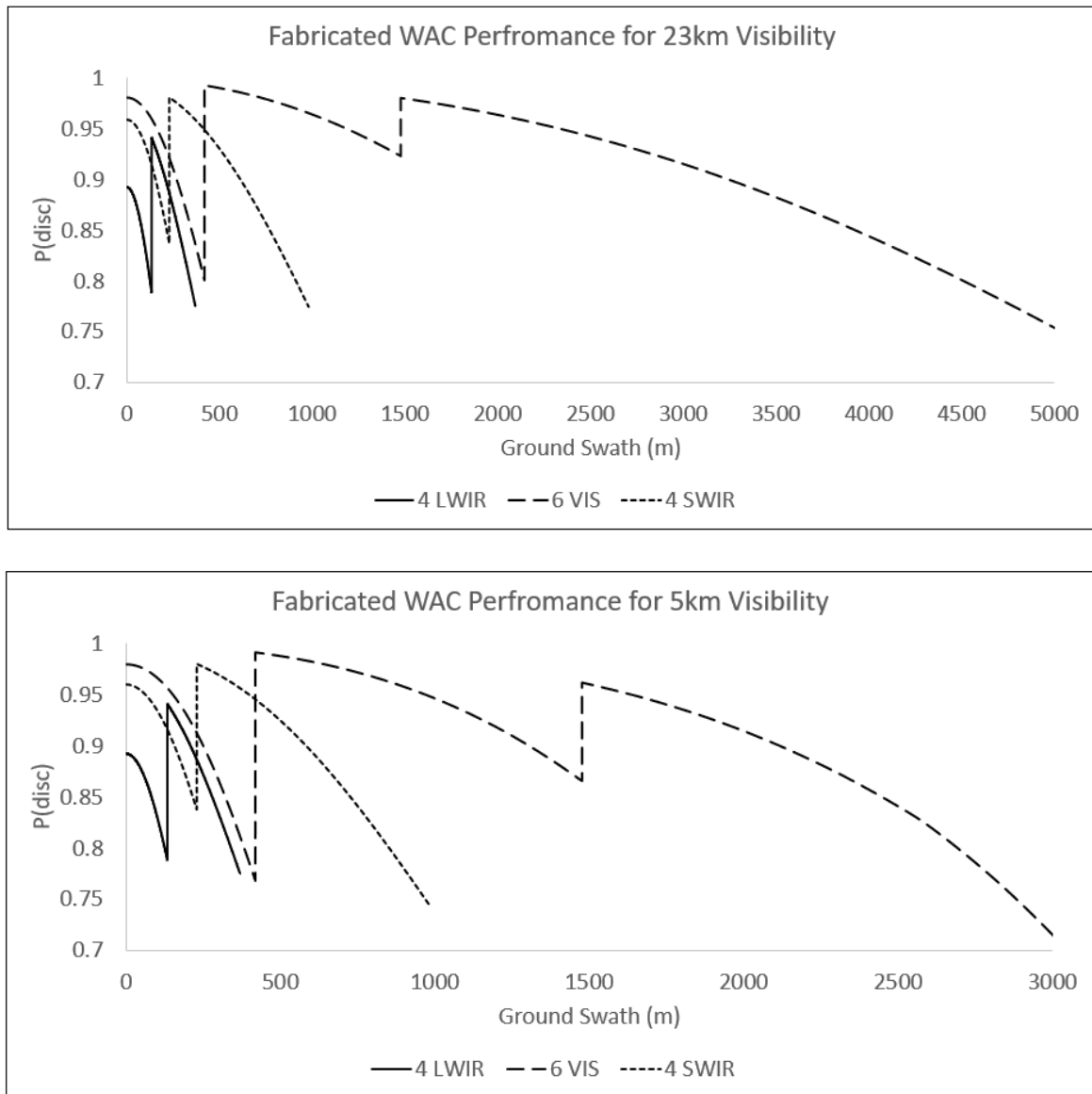
Figure 5.5: Modeled probability of discrimination curves associated with the fabricated WAC systems for both 23km and 5km cases.

5.7) WAC Testing

The three systems fabricated for WAC data collection were flown with targets at known distances. A data collection was performed in Memphis, TN with the University of Memphis in July 2022. The site was Agricenter International, a field crop research center in Shelby County, Tennessee. The targets used for this study were a Chevy Colorado, a Honda Odyssey, and a New Holland T5 Series Tractor (Figure 5.6). All vehicles had a characteristic dimension of roughly 3.1m. The three camera systems were flown on a DJI Matrice V200 at the designed altitude of 121m (400ft).

Figure 5.6: High Resolution imagery of the truck (left), van (middle) and tractor (right) used for the target set.

Automated flight paths were created so the target would appear in the FOV of each sensor two times with known ranges for many frames. The first distance was aligned to the middle of the FOV and corresponded to a high probability of discrimination (P(disc)), generally greater than 90%. The second distance placed the target at the far edge of the FOV to test the calculated GSD limits of each sensor for a P(disc) of around 80%. The distance to the target set was moved slightly closer than the exact edge of the FOV in case the flight dynamics of the Matrice angled the sensors such the target was out of the FOV. Multiple passes were also flown to ensure the target was in the FOV of each sensor. When imaging, the angle of the cameras

results in imagery that is shaped as a keystone. An example of the 6-camera VIS WAC imagery projected onto the ground into its keystone shapes is seen in Figure 5.7. Due to line-of-sight limitations not all drone to target distances could reach the range for a P(disc) = 80%. The distances, probabilities and resulting GSDs are listed in Table 4.

Table 5.4: Ranges and probabilities associated with the Memphis tests run to image the target set at various distances.

Camera	FOV [deg]	Range 1 [m]	P(disc) 1 [%]	GSD 1 [cm]	Range 2 [m]	P(disc) 2 [%]	GSD 2 [cm]
VIS WFOV	73.8	200	90.6	12.2	400	74.4	21.8
VIS NFOV	11.5	700	98.2	7.0	1060	95.9	10.5
VIS NNFOV	5.4	3,000	91.1	13.8	5,000	74.2	22.3
SWIR WFOV	62.0	100	96.0	10.4	200	87.2	19.5
SWIR NFOV	21.0	400	95.4	11.8	800	84.4	22.9
LWIR WFOV	47.6	75	85.7	16.2	125	80.0	22.7
LWIR NFOV	24.1	225	88.9	16.8	350	79.2	24.3

.
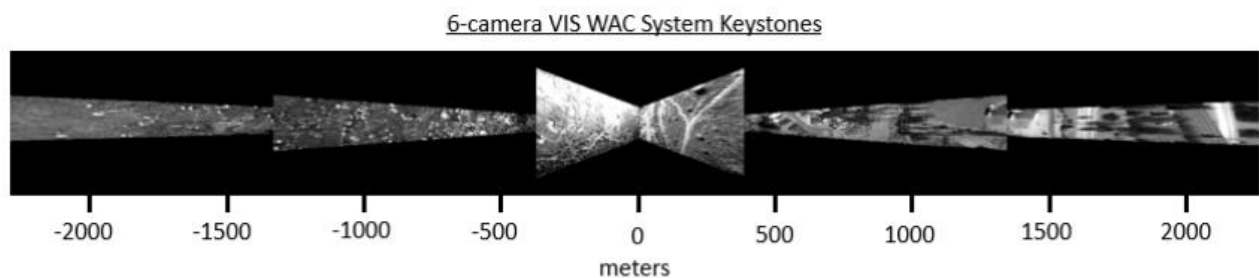
Figure 5.7. Example visible band image taken from an altitude of 120 meters. The placement of each pixel has been mapped to a point on the ground which results in these keystone effects.

5.8) WAC Results

The WAC optimization sensors are designed to have a P(rec) ≥ 80% for each FOV. The test plan in Table 5.4 was performed to test the P(disc) for each FOV of the three WAC sensor systems. In lieu of perception testing, the number of pixels expected to fall on the targets are

counted. The number of pixels, as determined by NVIPM for a given P(rec) and range, are compared to the number of pixels found on the target from the imagery. The number of pixels on target was found by a freeform ROI in ImageJ. This test ensures that the optimization design process and the addition of multiple FOV's in this method yields the expected results from NVIPM. The results of the field test show that the large number of pixels on target is achieved at long ranges by expanding the systems overall FOV with this multi-camera design method.

For each case, the number of pixels as specified for the P(rec) at each range matched. For the truck, there were regularly less pixels on target than expected. This was explained by the truck not having any "target" pixels above the bed of the truck. However, the "lack" of target pixels in that area is what allowed the identification of the truck from a van, making the pixel information in that area useful (Figure 5.8). Other fluctuations in the number of pixels were due to taking the characteristic dimension as the square root of the length times the height of the object and some of the vehicle orientations are not directly viewed at that angle.

Figure 5.8: Frames from different test sequences from the data collection that imaged the truck, van, and tractor in the 3 different bands being studied.

Table 5.5: A few cases chosen associated with the imagery in Figure 5.8 to show the number of pixels that imaged these target sets matched the expected number of pixels to fall on the targets.

System FL (mm)	Band	Range (m)	P(rec)	Model # of pixels	Truck # of pixels	Target 2 # of pixels
75	VIS	5,000	75.4%	182	144	183
4.5	VIS	297	89.9%	399	370	365
5.4	SWIR	197	89.9%	354	324	325
17.5	SWIR	748	85.7%	215	220	222
8.7	LWIR	125	84.4%	188	152	202

5.9) Conclusion

The optimization process for creating WAC systems was developed and tested for targeting systems. Using a GSD generated by NVIPM for a P(disc) $\geq$ 80% was a reasonable metric to set the performance of these systems. The *FoM* also provided direct comparison of different band systems under various atmospheric conditions. In this study it was assumed that all pixels were independent of each other when counted for the comparison of the modeled and measured number of pixels. With this assumption, the number of pixels expected to land on the target matched the number measured.

Future work will quantify the blur associated with these pixels from the dynamics of the drone platform. The movement of the pixel on the ground during the integration time of the camera will be studied and the performance will be compared to ideal conditions. We expect the narrow FOV sensor performance to suffer and for drone dynamics to effect imaging performance. The creation of the *FoM* is also to compare multi-camera systems to gimballed systems in the future. In this study, fixed optic and zoom optic gimbals will be considered. Other work includes using multiple frames of the same target set during flight to test super-resolution routines to enhance the performance of the system as well as using automatic target recognition algorithms to detect the targets during flight.

Chapter 6: Situational Awareness for Firefighters by Drone Based Imaging Systems

6.1) Overview

In recent decades, wildfires have become increasingly widespread and hazardous. Dryer, hotter weather combined with more frequent heat waves leave forest areas susceptible to sudden, intense, and fast-growing forest fires. To protect private property and mitigate the damage, Hot Shot fire fighters are deployed into these dangerous situations. Extensive satellite and aerial platforms possess optical techniques for monitoring wildfire risks and boundary tracking. sUAS (small unmanned aerial system) based EO/IR systems provide a solution for real-time, high resolution, targeted response to acquire information critical to the safety and efficacy of wildfire mitigation. Real-time imagery from a sUAS of the position of Hot Shots and the progression of the fire boundary would be easily obtained and offer a method of ensuring safe deployment. An ideal sensor system for situational awareness in this environment would be able to image the ambient terrain and firefighters with good contrast while also detecting fire signatures and imaging through the smoke. The longer wavelength infrared bands have demonstrated imaging through the smoke of forest fires. However, near the wildfire where the Hot Shots work, they also receive strong radiometric signal from the temperature of the smoke. The emitted signal of the smoke can obscure the line of sight similarly to the scattering effect of wildfire smoke in the visible spectrum. The reflective and emissive components of a wildfire scene are studied and compared in the visible (VIS, 0.4 – 0.7μm), shortwave infrared (SWIR, 1.0-1.7μm), extended SWIR (eSWIR, 2.0-2.5μm), and longwave infrared (LWIR, 8-14μm). Both a radiometric model and calibrated field measurements find a band that has the highest probability for a continuous line of sight for terrain, firefighters, and fire signatures in a wildfire scene.

6.2) Introduction

While wildfires are known to play a natural and even beneficial role in certain ecosystems, their increasing prevalence and range poses a threat to global climate, human settlements, natural ecosystems, and more. In recent decades, rising numbers of heat waves and drought-like conditions have dried out forested regions around the world [1]. This severe dryness is slowly increasing both the frequency and severity of forest fires [2,3]. Lightning strikes cause the most prevalent natural ignition of forest fires but unfortunately in the past 10 years, 87% of all wildfires were caused by human activity [4]. Satellite networks [5,6] and local remote sensing [7,8] wildfire monitoring systems inform firefighters to initiate a prompt response for wildfire intervention. When a blaze commences, boundary mapping and fire progression monitoring data is generally acquired by sensors mounted on space-based vehicles or sUAS. It has been shown that synthetic aperture radar (SAR) [9], visible to longwave infrared hyperspectral [10,11], and optical broadband sensors [12,13,14] can be effective in active fire perimeter mapping. Generally, these systems are lower resolution with around a 1-meter pixel size on the ground, called ground sample distance (GSD). These systems assist firefighters in identifying locations of interest for deployment.

Hotshots are a specialized firefighter who handles all phases of a fire, including ground support during the hottest part of the wildfire. They are vital to fighting fires to prevent blazes from progressing into specified areas and consuming more forest than is needed. A major concern for deployed firefighters is how to maintain safety while working in the field. Between 2000-2019 there were over 400 on-duty wildland firefighter fatalities [15]. A few mass events have recently claimed the lives of Hotshot teams [16]. The most recent mass casualty was the Yarnell Hill Fire, which claimed the lives of 19 Granite Mountain Hotshots in Arizona [17]. This

event has been analyzed and used for training purposes to understand how crews can be better prepared to prevent tragedy [18]. The biggest take-aways from this incident is that tracking crews, equipment, and the fire is vital to the safety and efficacy of firefighters.

One helpful safety measure is to have fire fighters wear sensors that monitor surrounding temperatures. Thermal Sensing Units, for example, can be worn by firefighters, alerting them when their environment becomes too hot [19]. This is helpful when firefighters are in close contact with fire, but fire progression can be too rapid and unpredictable for this measure to be effective in all situations. In such cases, collecting optical band imagery from an sUAS would allow teams to acquire highly responsive and detailed information about fire progression and firefighter location. This kind of information may allow firefighters to increase their situational awareness and survive otherwise deadly conditions.

6.3) Background

Broadband optical systems provide good resolution, small size, weight, and power (SWaP), and high frame rates. If optical methods are used for the monitoring of crews during a blaze, the system designed should be able to always locate the firefighters and detect key elements of the fire. By studying the performance of various imaging bands, a system can be developed to provide the best information possible to keep firefighters safe. Current deployed sUAS's are used to help identify hot signatures in the field and fly payloads such as the Zenmuse XT2. This gimbal system has both a VIS sensor for situational awareness and an LWIR sensor to detect the potential fire signatures in the field (Figure 6.1).

Figure 6.1: Overlapping VIS and LWIR aerial imagery demonstrating the current imagery obtained by the Zenmuse XT2 system. This imagery was provided by a Southwest Region Forestry service drone pilot. (LWIR imagery is white cold and black hot with an unknown color threshold)

Problems arise for a situational awareness that are clearly shown in this imagery. For the VIS system, the smoke scatters and adds reflected smoke signal radiance which obscures the terrain and any personnel withing the smoke cloud. The LWIR is an 8 bit-depth sensor resulting in poor contrast due to the large spread of blackbody equivalent (BBeq) temperatures throughout the scene. In addition, the smoke temperatures emit smoke signal radiance that obscures the LOS of the sensor to the ambient scene behind it. This is emphasized in Figure 6.2 with VIS and LWIR imagery taken with a Zenmuse XT2 flown on a DJI Matrice next to a blaze. The same phenomena are seen throughout forest service literature [20].
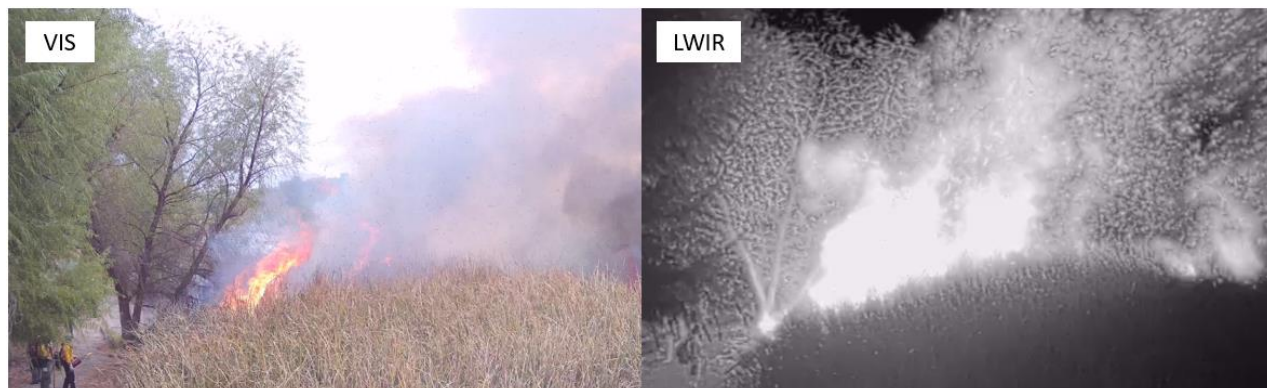
Figure 6.2: View of a controlled burn in the VIS on the left and LWIR on the right. The large smoke plume on the right-hand side of the LWIR image shows how the smoke directly around the fire has a bright radiometric signature in the LWIR.

The results of two studies help define the problems that will arise with EO/IR sensors for situational awareness in wildfires. First, a study that investigated the temperature of smoke as a function of height during an open field burn revealed that the temperature of the smoke above the fire can be as high as 600°C when 2 meters off the ground (Figure 6.3) [21]. For an average human height of 1.7m, the emitted signal from the smoke up to and above their head is very high. In the LWIR, the hot smoke signal would obscure any terrain or firefighter location data behind it. This would lead the sensor design to shorter wavelengths. As the wavelength decreases, as seen in the VIS band imagery in Figures 6.1 and 6.2, the transmission of signals through the smoke particles is attenuated substantially (Figure 6.3) [22].
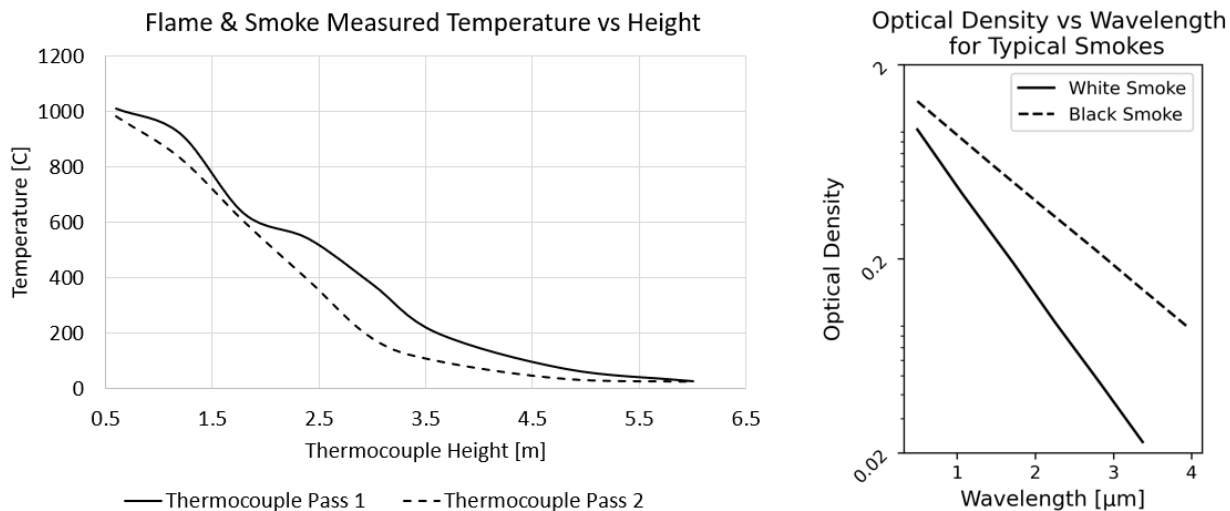
Figure 6.3: (Left) Reduced Data from Reference 21. Measured temperature of brush fire as a function of smoke height. In the paper there were 10 thermocouples spaced in height, sampling the temperature in the flames to 6m above the ground. (Right) Optical density of white and black smoke versus wavelength. Reduced Data from Reference 22.

The problems associated with these two bands lead to the investigation of other typical infrared imaging wavelengths. The shortwave infrared (SWIR, 1.0-1.7μm) and extended-shortwave infrared (eSWIR, 2.0-2.5μm) bands land in a middle ground of these reflective and emissive signal issues. As the wavelength increases from the visible band, the scattering and reflected smoke signal decrease dramatically. However, as the wavelength increases to the eSWIR band, even though the scattering effects are minimal, the emitted smoke signatures increase greatly. For this study, the near-infrared (NIR, 0.7-1.0μm) and mid-wave infrared (MWIR, 3.0-5.0μm) are excluded. The reasoning is that the NIR is mostly limited by scattering similarly to the VIS and the MWIR is excluded because it is limited by emitted smoke signal like the LWIR. This becomes apparent later in the paper.

6.4) Radiometric Signal Modeling

6.4.1) Definition of Terms

Traditionally the VIS, SWIR and eSWIR are mostly reflective bands that rely on solar illumination and object reflectivity for passive imaging. In the wildfire type environment, the high temperatures emit signals into these three bands. This means that not only the solar irradiance and scene reflectivities need to be considered but the temperatures of the terrain, firefighters, fire, and smokes emissive signal needs to be considered as well. To keep the reflective and emissive signals ordered, the first letter of the subscript is denoted as an *"r"* or an *"e."* As an example, for the total radiance from a human, the equation would be,

$$L_{Hum}(r,\lambda,\rho,T) = L_{rh}(r,\lambda,\rho) + L_{eh}(r,\lambda,T) \qquad \text{[W/cm}^2\text{-sr]} \qquad (6.1)$$

where $L_{Hum}(r,\lambda,\rho,T)$ is the total radiance as a function of range (r), wavelength (λ), reflectivity (ρ), and temperature (T, includes emissivity). $L_{rh}(r,\lambda,\rho)$ is the reflected solar radiance off a human and $L_{eh}(r,\lambda,T)$ is the emitted radiance from a human, where the subscript r denotes the reflective portion, the subscript e denotes the emissive portion, and the subscript h identifies the human.

6.4.2) Reflective Band Modeling

The source of light for reflective bands comes from spectral solar irradiance. Each object in the scene has a spectral reflectivity ($\rho_{surf}(\lambda)$) and a bidirectional reflectance distribution function (BRDF). For the terrain and human targets within the scene, the BRDF is typically Lambertian. The total reflected radiance from targets within the scene then becomes,

$$L_{rt}(r,\lambda) = \frac{E_{Solar}(\lambda) \cdot \rho_{surf}(\lambda)}{\pi} \qquad \text{[W/cm}^2\text{-sr]} \qquad (6.2)$$

Where $E_{Solar}(\lambda)$ is the solar irradiance and $L_{rt}(r, \lambda)$ is the reflected solar radiance from a general

target "t". Traditionally, as this signal propagates to the sensor in a scene with no smoke, the

atmospheric transmission decreases the target signal and atmospheric path radiance adds to the

total signal received. The design of this situational awareness system is for close range

applications (<1km). An assumption is made that the atmospheric transmission and path radiance

(excluding the smoke signal) will not impact the reflected radiance from the targets noticeably

and is excluded from this study.

The largest contribution to target signal degradation within the scene is from the smoke

and fire. The smoke impacts the target reflected radiance in two ways. Transmission through the

smoke reduces the signal behind it through scattering. At the same time, the smoke is illuminated

by the sun and adds reflected smoke radiance to the target's propagating signal similar to an

atmospheric path radiance. Both contributions depend on the number of particles, concentration,

and particle size. For this model, these dependencies are modeled as the extinction coefficient

and concentration length. The transmission equation is then,

$$\tau_{smk}(r,\lambda) = \exp(-\alpha(\lambda)CL(r)) \qquad \text{[unitless]} \qquad (6.3)$$

Where $\tau_{smk}(r,\lambda)$ is the spectral transmission through smoke, $\alpha(\lambda)$ is the extinction coefficient

and $CL(r)$ is the concentration length. This method is consistent in sensor performance modeling

software such as the Night Vision Integrated Performance Model (NVIPM).

The reflected smoke signal radiance ($L_{rs}(r,\lambda)$) is managed in a few separate ways. For

this paper $L_{rs}(r,\lambda)$ is related to $\tau_{smk}(r,\lambda)$. Both these terms will have the same $CL(r)$ at the

same time. However, $\alpha(\lambda)$ is slightly different for the $L_{rs}(r,\lambda)$ and $\tau_{smk}(r,\lambda)$ signals due to the

"illumination" conditions. For transmission, the target signals are propagating on-axis through

the smoke and scattered away. This is denoted as an illumination angle (θ) of $0°$. The $L_{rs}(r,\lambda)$ signal comes from off-axis reflected light from the sun. For the application of a downward facing sensor identifying terrain and people, this is a backscattered effect. A bidirectional scattering distribution function (BRSF) describes the change in the extinction coefficient based on θ. The scattering angle dependency on $\alpha_\theta(\lambda)$ for wood smoke has been previously studied [23,24]. Because of this $L_{rs}(r,\lambda)$ is modeled similarly to $1 = \tau + R + A$, where τ is transmission, R is reflection and A is absorption. White smoke seen in wildfires is mostly scattering dependent, so the absorption term is dropped. Rearranging these terms gives the equation,

$$L_{rs}(r,\lambda,\tau,\theta) = \frac{E_{Solar}(\lambda)\cdot(1-\exp([-\alpha_\theta(\lambda)\cdot CL(r)])\cdot\rho_{Smk}(\lambda)}{\pi} \qquad \text{[W/cm}^2\text{-sr]} \quad (6.4)$$

The only new term included is a "maximum reflectance" term of smoke, $\rho_{Smk}(\lambda)$. This term describes the maximum reflectivity of smoke as the concentration becomes thick enough that it resembles a solid object. This term is found experimentally through calibrated imagery when there is absolutely no transmission through the smoke. The total reflected radiance towards the aperture of the sensor is now,

$$L_{ap}(r,\lambda,\tau,\theta) = L_{rt}(r,\lambda)\cdot\tau_{Smk}(r,\lambda) + L_{rs}(r,\lambda,\tau,\theta) \qquad \text{[W/cm}^2\text{-sr]} \qquad (6.5)$$

Where $L_{ap}(r,\lambda,\tau,\theta)$ includes all reflected target and reflected smoke radiance terms that can enter the aperture of the sensor.

6.4.3) Emissive Band Modeling

The emissive terms are considered due to the high smoke temperatures providing emitted radiance to all the bands studied. Spectral emittance is given by Plank's radiation law,

$$M_e(T,\lambda) = \varepsilon(\lambda)\frac{c_1}{\lambda^5}\frac{1}{[e^{\frac{c_2}{\lambda T}}-1]} \qquad \text{[W/cm}^2\text{]} \qquad (6.6)$$

Where $M_e(T,\lambda)$ is emittance, c_1 and c_2 are physical constants of 3.7418 x 10^4 [W- μm^4/cm^2] and

1.4338 x 10^4 [μm-K] respectively, $\varepsilon(\lambda)$ is emissivity, and T is temperature. Continuing with the

Lambertian assumption applied to emitted light, the emitted target radiance becomes,

$$L_{et}(r,T,\lambda) = \frac{M_e(T,\lambda)}{\pi} \qquad \text{[W/cm}^2\text{-sr]} \qquad (6.7)$$

The same assumption about atmospheric path radiance is made here as it was above in the

reflective part of the model. It is also assumed that the smoke signal can be treated as a

blackbody source and calculated using the same methods as the targets above. This makes the

emitted radiance that can enter the aperture,

$$L_{ap}(r,T,\lambda) = L_{et}(r,T,\lambda)\cdot\tau_{Smk}(r,\lambda) + L_{es}(r,T,\lambda) \qquad \text{[W/cm}^2\text{-sr]} \quad (6.8)$$

6.4.4) Total Radiometric Model

The base terms for the reflective and emissive portions of the radiometric model are

defined. Since the temperature of the smoke is high enough, the traditionally reflective bands

(VIS, SWIR, eSWIR) now contain emissive signals. All the terms combined produce the

equation.

$$L_{ap}(r,T,\lambda) = [L_{rt}(r,\lambda) + L_{et}(r,T,\lambda)]\cdot\tau_{Smk}(r,\lambda) + L_{rs}(r,\lambda) + L_{es}(r,T,\lambda) \text{ [W/cm}^2\text{-sr]} \ (6.9)$$

This equation describes the total radiance coming from a scene that contains firefighters, terrain,

fire, and smoke. Moving forward, this equation helps define the ratio of signals in a scene and

how each band is affected by smoke concentration and temperature when imaging a target.

Figure 6.4 gives a visual representation of where these signals are and how they contribute to the overall scene.
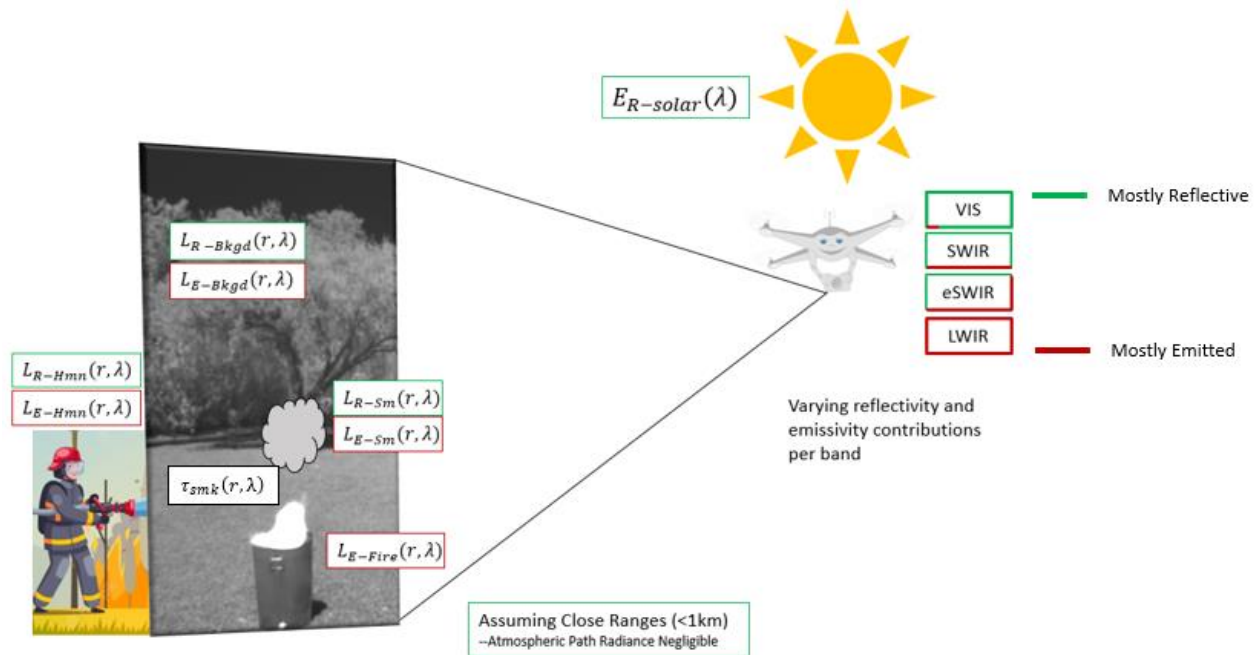
Figure 6.4: Drone measuring the different ambient scene and fire radiance. Each signal has a solar reflected radiance and produces an emitted radiance. These signals change with solar irradiance, reflectivity, emissivity, and temperature.

6.5) Reflective and Emissive Calibration Measurements

The goal of the situational awareness system is to view the ambient scene containing terrain and firefighters with good contrast while smoke and high emissive signals are present. The VIS, SWIR, eSWIR and LWIR sensor used in this study can be found in Table 6.1. For VIS, SWIR and eSWIR spectral solar irradiance is the ambient illumination source. Solar illumination can be measured through calibrated spectrometers, broadband pyranometers, or modeled through

atmospheric modeling software such as the MODTRAN (Moderate Resolution Atmospheric Transmission) [25].

The temperature at which emissive smoke signals can first be detected over low reflectance signals is different for the VIS, SWIR and eSWIR. This is an artifact of both Plank's radiation law giving higher emittance for longer wavelengths at lower temperatures and the ratio of solar irradiance in each band. For the same reasons, the hot smoke signal radiance will also exceed highly reflective target radiance at the longer wavelength and saturate the sensor before the shorter wavelengths. To find the perceivable temperatures that appear within the ambient scene dynamic range, a calibration between targets with known reflectivities and high-temperature blackbodies (HTBBs) is performed.

Vantablack, "gray" Spectralon, and "white" Spectralon with an Apogee NIST traceable pyranometer are used to calibrate the reflective portion of a scene to reflected solar radiance. The average reflectivities of each target, per band, are found in Table 6.1. The reflective targets are placed directly pointed at the sun with the sensors aimed at the reflective target's surfaces. The "white" Spectralon and Vantablack reflective targets are used to set the dynamic range of the ambient scene. Setting the dynamic range of each sensor with these targets captures all Lambertian signals within a scene for calibration. The integration times of each sensor are tuned so that the Vantablack is around 10% of the dynamic range of the sensor and the white Spectralon is around 90%.

Table 6.1: Specifications of the sensors used and the target reflectivities.

Value	VIS	SWIR	eSWIR	LWIR
Sensor Model	Allied Vision Alvium 1800 U-240	Allied Vision Alvium 1800 U-130	PhotonEtc Zephir 2.5	FLIR Boson 640
QE with Filters [um]	0.4-0.7	1.0-1.7	2.0-2.5	7.5-14
Format	1936 x 1216	1296 x 1032	320 x 256	640 x 512
Focal Length [mm]	12	16	25	18
Pixel Pitch [um]	3.45	5	30	12
NETD [mK]	-	-	-	<40
Calibration Target Reflectance				
Vantablack	0.00881	0.00975	0.0100	-
"Gray" Spectralon	0.490	0.556	0.596	-
"White" Spectralon	0.984	0.989	0.947	-

The calibrated pyranometer was placed in full sun to record the total solar irradiance during all measurements. To find the in-band reflected radiance, the measured total solar irradiance from the pyranometer scales the curve in Figure 6.4 for each measurement. The spectral QE of each sensor is then multiplied by the Lambertian reflectance of each reflective target to obtain calibrated solar reflected radiance scenes. The integral of this quantity produces the total in-band reflected radiance for each sensor. This is represented in equation 6.10.

$$L_{rt}(r,\lambda) = \int_{\lambda_1}^{\lambda_2} \frac{E_{Solar}(\lambda) \cdot QE(\lambda) \cdot \rho_{surf}(\lambda)}{\pi} \, d\lambda \qquad (6.10)$$

Where λ_1 is the lower cutoff wavelength of the sensor and λ_2 is the upper cutoff wavelength for each sensor. The solar reflected radiance is calculated for all three reflective targets.

The "ambient" emissive sources are four regular temperature blackbodies (RTBBs) from True Colors Infrared with emissivity's of 0.98. To model the smoke and fire emitted signals, two cavity HTBBs are used: one from CI Systems (Model SRS-2-32) and the other from Infrared Systems Development Corporation (Model IR-563/301). Each HTBB has an emissivity of 0.99

and an output aperture of one inch. All blackbodies were placed underneath the reflective target table to keep solar reflections to a minimum. The lower temperature blackbodies were set at 20°C, 35°C, 50°C, and 80°C. One HTBB was placed at 1000°C for all measurements and the other was stepped up in increments of 100°C from 100°C to 1000°C. The HTBB changing in temperature is used to simulate realistic smoke temperatures within a wildfire.

For each sensor measurement, the gain was set to 0 and 3 different integration times were used to image the HTBB at each temperature. Any non-linear histogram stretching in the sensor software's was disabled. All targets were set in each sensor's FOV with many pixels on each target (Figure 6.5). At each HTBB temperature, multiple frames were captured and averaged to minimize the noise of the sensors.
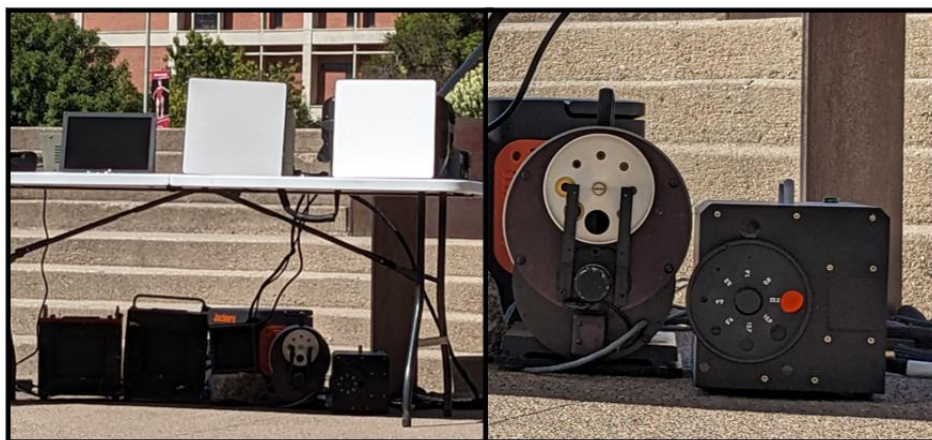
Figure 6.5: The reflective band targets can be seen on top of the table on the left-hand side and show the Vantablack, "gray" Spectralon and "white" Spectralon from left to right. Underneath the table the three ambient temperature blackbodies are seen followed by the two HTBBs. On the right-hand side of the figure, the HTBB at 1000°C is seen glowing red.

The reflective target set along with the pyranometer are used to calibrate the imagery to radiance. The target set produces a three-point gray level versus reflected radiance curve for each

band. With this curve each gray value in the image is converted into radiance for each band. For each integration time, the signals from the HTBB ranging from 100°C to 1000°C are recorded. The calibrated radiance measured within the scene was compared to the theoretical blackbody radiance produced by the HTBB at each temperature (Figure 6.6). In each band, the measured and calculated emitted radiance from the HTBB matched for each integration time.
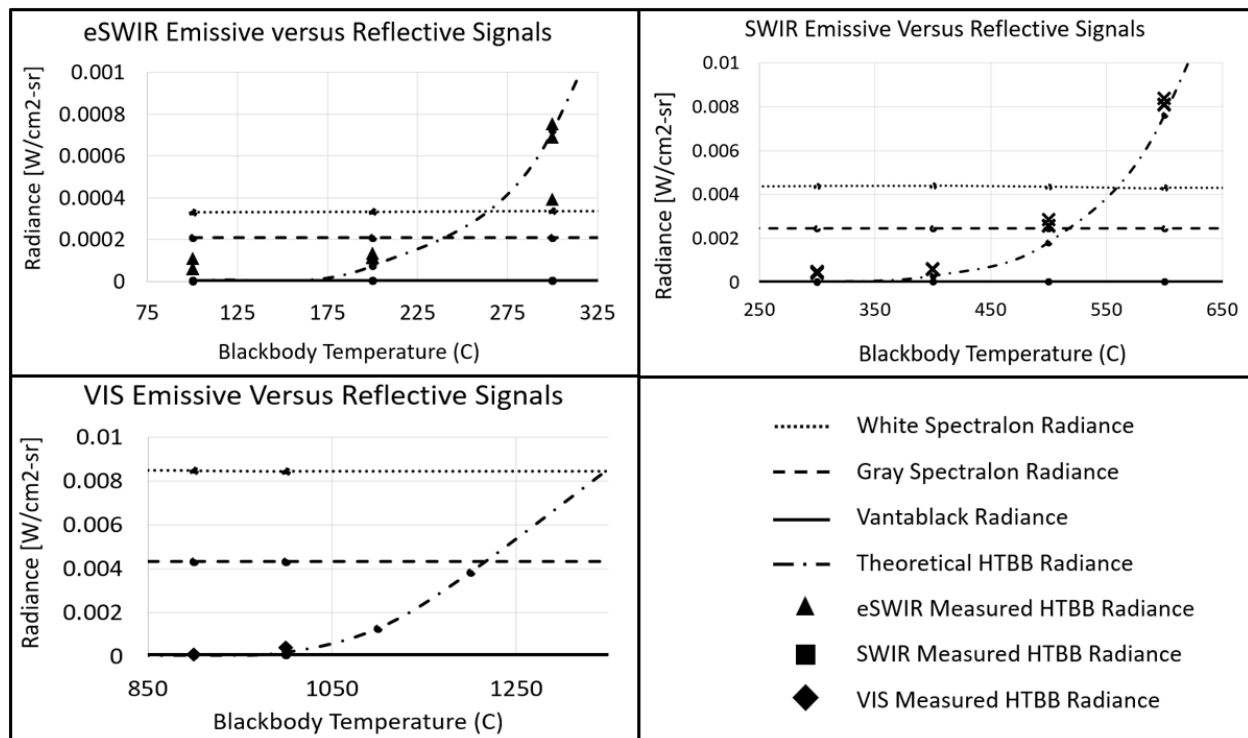
Figure 6.6: Calibrated reflective target radiance versus emitted HTBB radiance curves for various temperatures. Includes modeled blackbody radiance for each band as well.

With this calibration technique, the detectable blackbody equivalent temperatures (BBeq) in each band without black or white saturating are also found. The temperature at which the HTBB emitted signal is higher than the Vantablack reflected radiance is recorded as the first perceivable temperature. When the HTBB emitted signal is higher than the white Spectralon reflected radiance, the BBeq temperature that overtakes the ambient scene signals is also

recorded (Table 6.2). The BBeq temperatures higher than this value saturates soon after due to the dynamic range setting technique.

Table 6.2: HTBB temperature settings that produced emissive signals higher than the Vantablack target and the white Spectralon target. *The highest HTBB producible temperature is 1000°C so the VIS higher temperature is just theoretical.

Threshold	VIS	SWIR	eSWIR
Lower HTBB Temp [C]	900	300	100
Higher HTBB Temp [C]	1345*	560	265

As expected, for viewing an ambient scene, the longer wavelengths capture the lower HTBB temperature emitted radiance, and the shorter wavelengths perceive the higher HTBB temperatures. This calibration method combines both the emissive and reflected signals within a scene for each band. It is informative for the temperatures that would not be detected while viewing an ambient scene as well as the ones that would saturate and potentially obscure signals due to the emitted smoke signal radiance.

6.6) Smoke Contrast Radiometric Model

Understanding how each band is affected by the presence of hot smoke alone gives context to how the contrast is degraded by both smoke concentration and smoke temperature. This is why the HTBB calibration is necessary. The most important function of this situational awareness system is to maintain good contrast when heavy concentrations of hot smoke are between the FOV of the sensor and the firefighters. The sensor must have high transmission

through the smoke, low reflected smoke signal radiance and low emitted smoke signal radiance. The VIS, SWIR, eSWIR and LWIR are all accompanied by contrast reduction due to the smoke, but it occurs through different phenomena at different rates. As shown in figures 6.1 and 6.2, the VIS suffers from both transmission loss and high reflected smoke signal radiance. In those same instances, the LWIR suffers from emitted smoke signal radiance from the hot smoke.

Equation 6.9 is used to model different conditions of smoke concentration and smoke temperature to find the effects on the VIS, SWIR, eSWIR, and LWIR bands. For the reflective bands, the targets used to achieve a contrast of one are the measured reflected radiance from the Vantablack and the white Spectralon Calibration. For the LWIR sensor, a contrast of 1 is achieved from two normal blackbodies set at a temperature of 20°C and 60°C. The contrast of these calibration targets are used to obtain an idea of the contrast reduction that would hurt performance when monitoring firefighters and terrain in the field. The contrast equation used for this model is,

$$C = \frac{W-B}{W+B} \qquad\qquad \text{[unitless]} \qquad (6.11)$$

Where C is contrast, W corresponds to the white board reflected radiance or 60°C RTBB emitted radiance behind the simulated smoke signatures and B is the black board reflected radiance or the 20°C RTBB emitted radiance modeled.

The range of smoke temperatures studied are ambient scene temperatures of 20°C to the 1000°C temperature that fires typically burn [26]. The CL of smoke used ranges from 0 to 1 g/m^2 which for the VIS band, results in complete obscuration of a scene [27], which is typical near wildfire conditions. The on-axis spectral wood burning $\alpha_\theta(\lambda)$ used is taken from references 23 and the off-axis BRSF is calculated from reference 24. A total solar irradiance of 1kW/m^2 is used

to calculate the reflected target radiance from each reflective target, and equations 6.6 and 6.7 are used to calculate both the target and emitted smoke signal radiance. Figure 6.7 shows the contrast dependency between smoke concentration and smoke temperature for uniform smoke and temperature in front of the contrast targets.
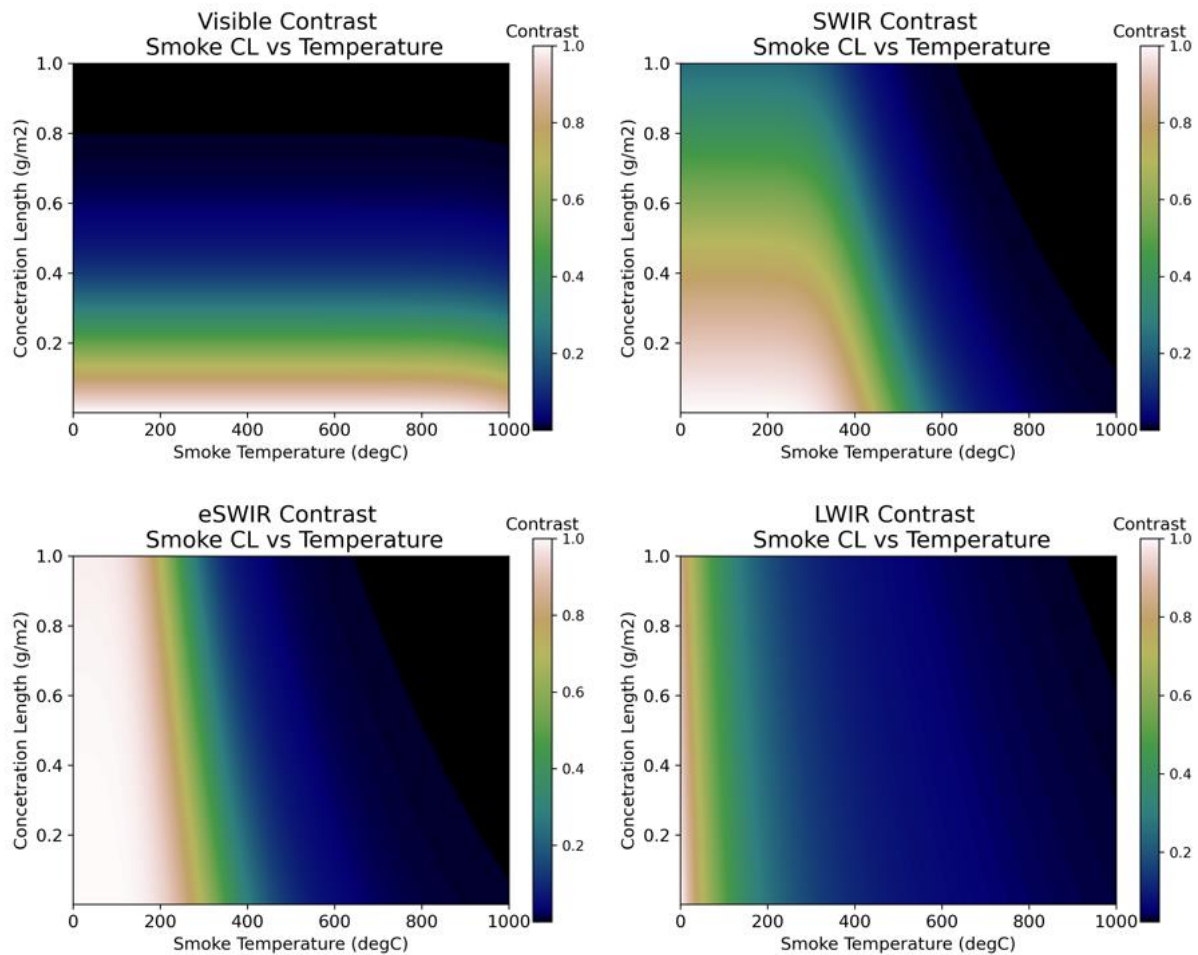
Figure 6.7: The y-axis varies concentration length, and the x-axis varies the smoke temperature. For each of these conditions contrast in each band is calculated as a heat map.

The results of the contrast modeling show what is expected of the VIS and LWIR bands based on previous imagery. The VIS bands contrast is mostly dependent on the concentration of smoke present in the scene and does not degrade with temperature substantially. This result is understandable from the calibration results where only temperatures above 900°C would be detected by the sensor. These temperatures only occur at the hottest point of the fire. The LWIR is the opposite where the concentration of smoke doesn't affect transmission much due to the much longer wavelength but, even at low temperatures, the LWIR's contrast is reduced due to the strong emitted smoke signal radiance. Similarly, the eSWIR band is mostly dependent on temperature but very heavy concentrations of smoke could affect the contrast as well. The SWIR band has smaller dependency on both smoke concentration and smoke temperature than the other bands. For heavy and hot smoke present between the sensor and the firefighters, the SWIR band has the best opportunity for good contrast in both conditions. Only in extreme conditions of concentration and near the hottest points of the fire at the ground would be contrast be reduced.

6.7) Dynamic Range Modeling

The situational awareness imaging system during a forest fire needs to have good contrast of the ambient scene and receive good radiometric signal from the fire. As shown in the calibration section, when setting a sensor's dynamic range to view the light provided by solar irradiance, the emissive smoke radiance can saturate the sensor even at low temperatures. To find the saturation temperatures for the specific sensors used in this study, the total radiance from equation 6.9 is converted to electrons. To do this, the a few more quantities need to be calculated. First is the projected area of the pixel that will be imaging the scene. This is given by,

$$A_{det} = \frac{\pi R^2 IFOV^2}{4} \qquad \text{[cm}^2\text{]} \qquad (6.12)$$

Where A_{det} is the projected area of a pixel, R is the range to the target, and $IFOV$ is the angular subtense of a single detector. The second quantity needed is the sensors solid angle,

$$\Omega_{sensor} = \frac{\pi D^2}{4R^2} \qquad \text{[sr]} \qquad (6.13)$$

To convert the total radiance to power, first the results from equation 6.9 are multiplied by the projected pixel area to object the intensity I.

$$I(T,\lambda) = L_{ap}(r,T,\lambda) \cdot A_{det} \qquad \text{[W/sr]} \qquad (6.14)$$

The intensity is multiplied by the sensor's solid angle to obtain the total power that is projected through the system onto a single pixel.

$$P_{det}(T,\lambda) = I(T,\lambda) \cdot \Omega_{sensor} = \frac{L_{ap}(r,T,\lambda) \cdot A_{det} \cdot D^2}{4R^2} \qquad \text{[W]} \quad (6.15)$$

The total power that is received by a detector can now be converted to electrons that are generated from the reflective and emissive components in a scene.

$$N = \frac{t_{int}}{hc} \int_{\lambda_1}^{\lambda_2} P_{det}(\lambda) \cdot QE(\lambda) \cdot \lambda \cdot d\lambda \qquad \text{[e-]} \quad (6.16)$$

Where μ is the number of electrons, t_{int} is the integration time of the sensor, h is plank's constant, c is the speed of flight, λ is wavelength, $P_{det}(\lambda)$ is the spectral power calculated from equation 6.15 and $QE(\lambda)$ is the spectral quantum efficiency of the sensor. By knowing the well capacity of the sensor and calculating the number of electrons generated from various signals, the %WF can now be calculated by equation 14.

$$\%WF = \frac{N}{N_{sat}} \qquad \text{[Unitless]} \quad (6.17)$$

Based on the integration time from equation 6.16, the point at which various emissive and reflective can black and white saturate the sensor can be found.

In this case, black saturation is defined when there are not enough electrons to generate a signal high enough to be above 10% well fill and white saturation is defined as when the well fill is above 90%. For the eSWIR band, as seen in figure 7, even low temperatures can saturate the sensor for the longer integration times. The signal modeled for the black saturation condition is the reflected radiance from the Vantablack target for a total solar irradiance of 1 kW/m^2 day. The signal modeled for the white saturation condition is the reflected radiance from the white Spectralon target. Alongside this, the emitted radiance from blackbody sources is modeled from ambient scene temperatures to typical wildfire temperatures of 1000°C. Figure 6.8 shows the black saturation, white saturation, temperature saturation and resulting spread of integration times that the eSWIR sensor could operate at.

Figure 8: Modeled percent Well Fill for the eSWIR band. The bottom right corner shows the range of integration times and temperatures that can be perceived while viewing an ambient scene.

The upper left plot shows the %WF for a range of integration times and temperatures. The absence of data means that the lower 10% and upper 90% well fill saturation was exceeded and the data was not included in the plot. The upper right plot shows that for typical solar illumination, an integration time of 456μs will cause the white Spectralon signal to saturate the sensor. The lower left plot shows that an integration time of 160μs will cause the Vantablack signal to black saturate. When confining the dynamic range for good contrast within ambient

illumination, these integration times then bound what temperatures can be measured as well. The lower right plot shows when the dynamic range is set this way, that the highest temperature that can be measured within the 90% cut off region is 240°C. The maximum temperature for complete saturation points for 100% well fill is 300°C. For the eSWIR, this low saturation temperature means that even the lower smoke temperatures will emit enough signal to saturate the sensors FOV and degrade the contrast of the firefighters and terrain behind it.

The SWIR sensor has a lot more flexibility when it comes to both integration time and smoke temperatures that can be measured (Figure 6.9). The lower integration time cut off in this case is 509μs, and the white saturation integration time was much higher than 2,000μs. While the SWIR can't measure as low as temperatures as the eSWIR sensor, the saturation temperature is much higher at 725°C. This gives the SWIR sensor a much better chance to have a good dynamic range of the reflective scene and not lose contrast of the targets of interest due to the emitted smoke signal radiance.
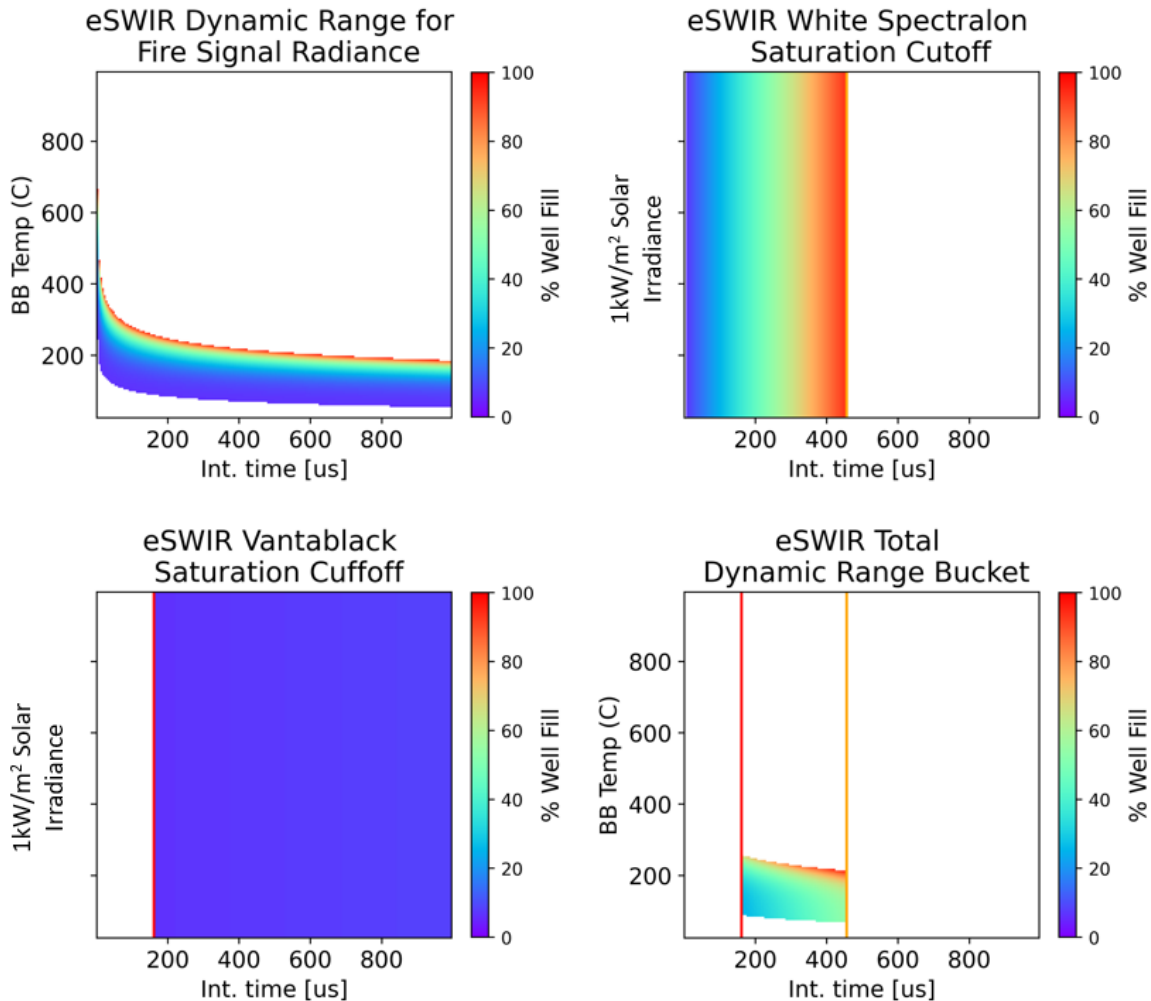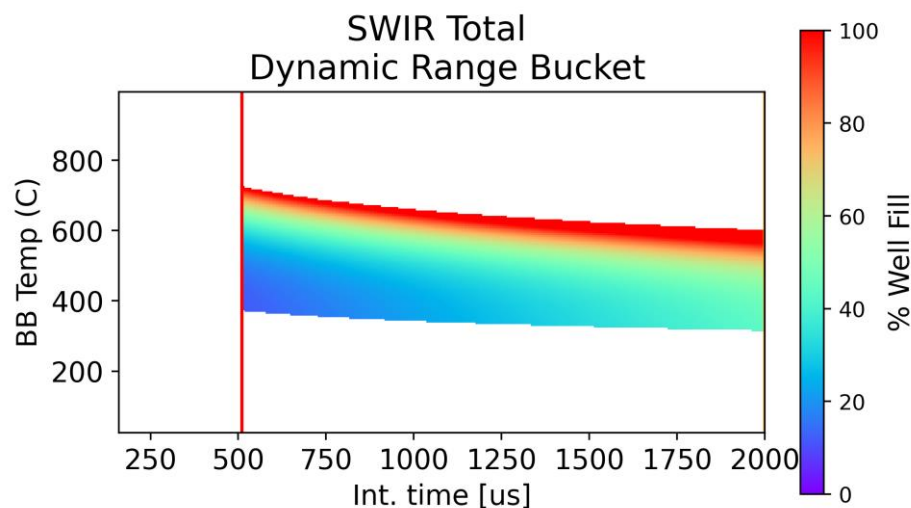

Figure 9: Modeled percent Well Fill for the SWIR band. The bottom right corner shows the range of integration times and temperatures that can be perceived while viewing an ambient scene.

6.8) Fire & Smoke Data Collection

To evaluate the modeled contrast findings, a field test was performed to measure the contrast degradation due to the presence of smoke. The measurements performed resemble the calibration study described above with more equipment. The same sensors in Table 1 were used. The three reflective targets, two RTBBs, two HTBBs, and pyranometer were all used to calibrate the scene in the same manner as before. The two RTBBs were set at 20°C and 60°C and the two HTBBs were set at 275°C and 550°C to calibrate various emissive portions of the scene for all bands. The calibration targets were placed in front of the fire to avoid any smoke contaminating their signals. Again, there were many pixels on the calibration boards to avoid noisy measurements.

In the middle of the scene, a contained fire was created with a combination of hardwood soaked in water and fresh brush cuttings. These materials were used to simulate the heavy smoke and intense heat produced in wildfire situations. To channel the smoke, ash, and heat into a column above the fire, a metal container was used to direct the fire byproducts (Figure 6.10). To measure the temperature of the fire and smoke, two DATAQ thermocouples were placed one and two meters above the ground. Lastly, to calculate the contrast reduction due to smoke, more calibration targets were placed in the FOV of the sensors, behind the metal container. A large white and black target with known reflectance and two RTBBs were placed in line with the smoke column. The two RTBBs were also set at 20°C and 60°C to produce the same signal as the emissive calibration RTBBs. The reduction in contrast due to transmission, reflected, and emitted smoke signal radiance was measured with this set up (Figure 6.10).
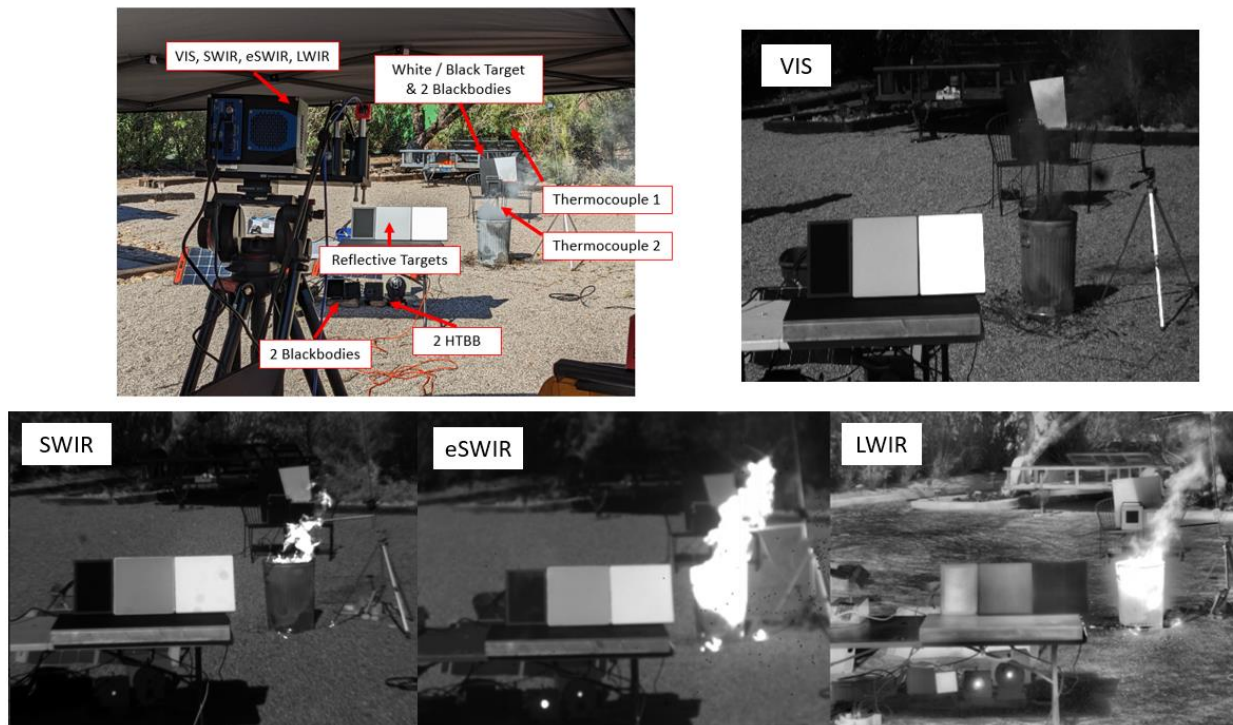
Figure 6.10: (Top Left) Commented color image to view the sensors orientation of the scene with calibration targets, fire, thermocouples, and the smoke measurements targets behind the fire. (Top Right) Time synced VIS imagery of smoke obscuring the contrast board. (Bottom) SWIR, eSWIR and LWIR imagery of the same scene. *(LWIR is CLAHE enhanced for figure).

During the data collection, the VIS, SWIR, eSWIR, and LWIR images were synchronized in time to measure the smoke's effect on contrast for the same concentrations and temperatures. 1150 time-synced frames were obtained for analysis. The data collection day had clear skies and minimal wind. The sensors were facing north so the sun was illuminating the scene from behind the sensors. Just as before, the calibrated pyranometer data was used to convert the gray levels in the reflective band scenes to radiance. In the same manner, the calibration RTBBs and HTBBs were used to create a system intensity transfer function curve (SITF) to convert the LWIR gray levels to emitted radiance values. With all band values now in total measured radiance, the

contrast of the white and black target and the two RTBBs behind the smoke for all 1150 frames was calculated.

6.9) Smoke Contrast Measurement Results

The contrast of the targets behind the metal container in this study are used to measure the reduction in contrast in a real forest fire. Adequate contrast is needed to keep line of sight on the forest firefighters and terrain to provide enhanced situational awareness while out in the field. The contrast is calculated from the high and low calibrated radiance signals that the sensors receive from the targets behind the smoke. The average raw signals from the calibration reflective targets, calibration RTBBs, smoke covered reflective targets, and smoke covered RTBBs are found in Figure 6.11.
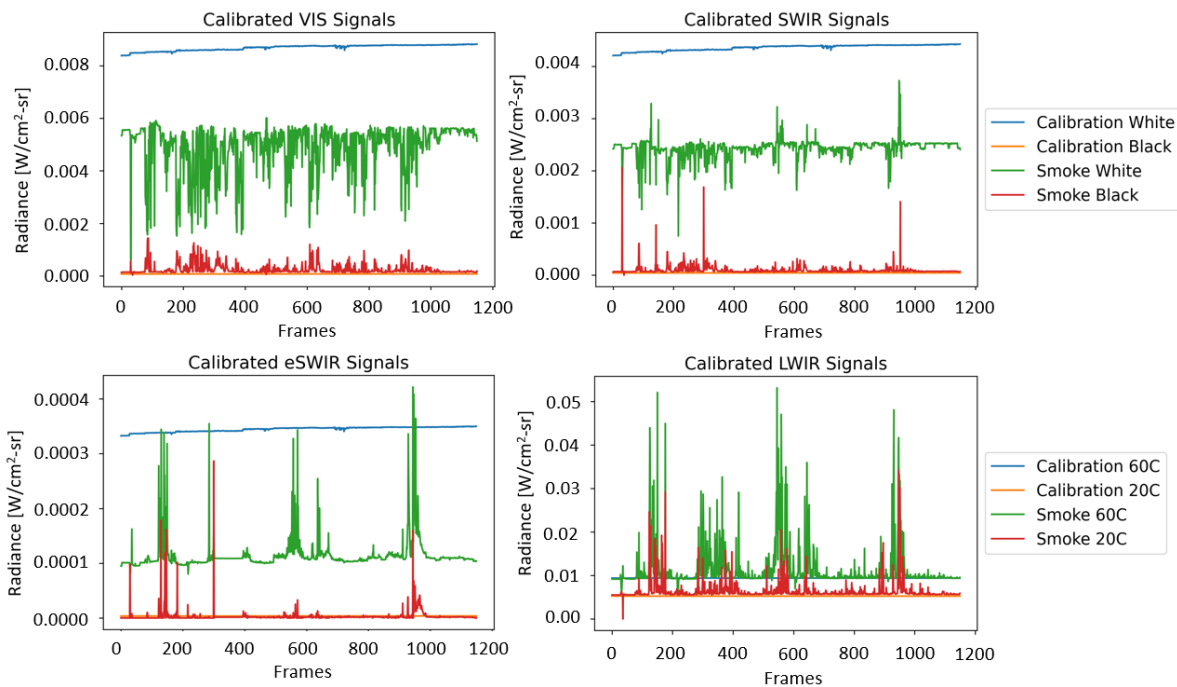
Figure 6.11: Measured radiance from the calibration and smoke covered targets for each band during the entire data collection.

The raw signals start to support the findings of the smoke contrast model. In the VIS, the decreased white signal shows that the transmission of the white board through the smoke decreases the signal and the increased black board signal is produced from the reflected smoke signal radiance. For the LWIR, both the average signal from the RTBBs behind the smoke columns increasing shows the added emitted smoke signal radiance from the hot smoke temperatures. The eSWIR can be seen to have a dependency similar to the LWIR, where both the black and white board average signals are increasing. Some instances of the white signal decreasing are seen in the eSWIR. This supports the findings of the model that show the eSWIR being more directly affected by the smoke temperature than concentration. A visual of this is also seen in Figure 8. Lastly, the SWIR is seen to fluctuate with both increasing and decreasing signals. As the contrast model predicted, the SWIRs imagery is affected by both smoke concentration and temperature but less for both phenomena.

To calculate contrast, three different calculations are performed. This is to account for the spatial non-uniformity that the smoke presents over the target boards. The first method calculates the contrast of the average radiance's values between the white and black board for the reflective bands and the low and high RTBBs. This is calculated using equation 6.11 above, where W corresponds to the white board or high RTBB behind the smoke column and B is the black board or the low RTBB for the LWIR. The W and B average radiances are found by an ROI drawn over their respective targets.

The second method calculates the contrast for every pixel contained in the ROI on the smoke covered white board or high RTBB and the smoke covered black board or low RTBB. This method considers the spatial non-uniformity of the smoke signals covering the board. This is calculated by,

$$C_{px} = \frac{W_m - B_n}{W_m + B_n} \qquad \text{[Unitless]} \qquad (6.18)$$

Where *m* represents the pixel number on the smoke covered white board or high RTBB and the *n* is the pixel number of the smoke covered black board or low RTBB. By studying the effect of all of the pixels within the ROI, the increased number of data points ensure the spatial non-uniformity effect of the smoke is measured in terms of contrast.

The last contrast calculation method is similar to the Speckle contrast equation [28]. This equation considers the random spatial variation of the constructive and destructive interference pattern of coherent light. Similarly, for non-uniform smoke it navigates the spatially varying contrast within the ROIs. This contrast equation is given by,

$$C_{Spk} = \frac{\sigma_{C_{avg}}}{<C_{avg}>} \qquad \text{[Unitless]} \quad (6.19)$$

Where $\sigma_{C_{avg}}$ is the standard deviation of the contrast found in equation 6.11 and $< C_{avg} >$ is the mean of the contrast found in equation 6.11. This new contrast ratio is calculated for each frame.

The effect of the smoke concentration and temperature on contrast is calculated for all three methods for all bands. The standard deviation (STD) of all frames is calculated for each of the contrast methods. The average STD for all frames using the three different methods is shown in Figure 6.12. The STD is used to compare the different bands because it describes both how often and how intensely the contrast is reduced. Alongside this, the number of times the contrast dipped below a threshold limit for each of the bands is counted to show which imager was affected the most often. These two methods show the bands that are least affected by the presence of high concentrations of hot smoke. Alongside the smoke covered board, the contrast

of the calibration Vantablack and White Spectralon is shown. The average STD for these frames

is approximately 0 because the signal doesn't change due to smoke.
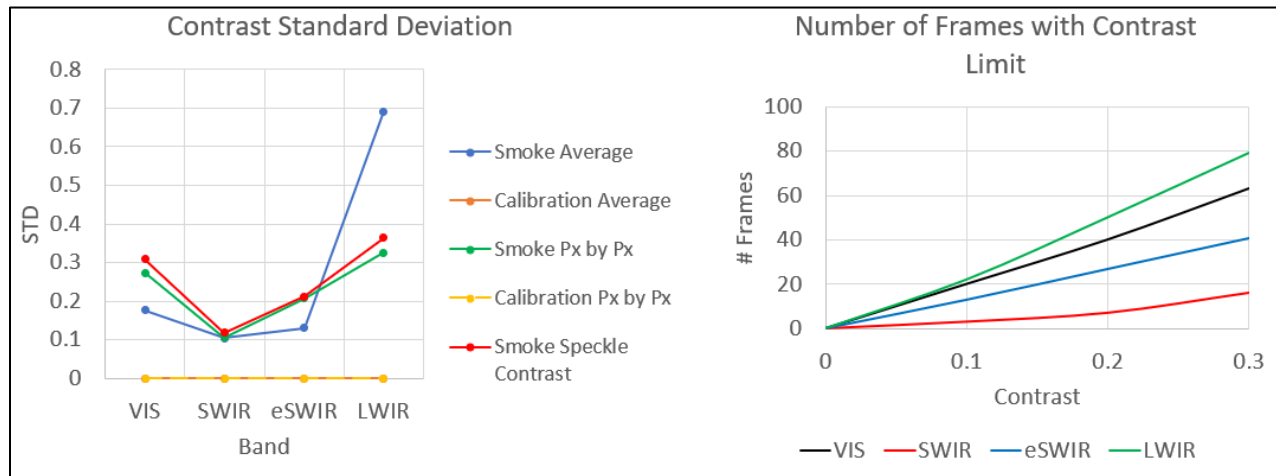
Figure 6.12: Standard Deviation calculated from the three methods above (Left). The smoke board through the three

methods are compared. The number of frames in each band for the most degrading contrast thresholds (Right).

6.10) Discussion

The analysis of the calibrated imagery shows that the SWIR band maintains better

contrast than the other bands. The SWIR has the lowest standard deviation of the four bands

studied for all three contrast calculations. The SWIR also has the lowest number of frames that

fall below the low contrast thresholds. In the raw data from Figure 6.11, it is apparent that both

the smoke covered black and white targets deviate from the mean value the least. Based on these

contrast results, the best band to visualize the hot spots of the fire, terrain and maintain line of

sight on the forest firefighters would be the SWIR.

The experimental data supports the results of the radiometric contrast model as well. The

SWIR's wavelength is long enough to have lower transmission degradation compared to VIS and

a short enough wavelength that isn't hindered by the emitted smoke signal radiance like the eSWIR and LWIR. This is a product of the rapidly decreasing smoke temperature as it rises as seen in Figure 3. Since the eSWIR and LWIR are sensitive to the lower temperatures, the colder smoke at higher altitudes still emits enough signal to reduce the contrast in each band. This is supported by and demonstrated in Figure 6.8.

Followed by SWIR, the eSWIR has the next lowest effect from the presence of smoke. While the longer wavelength helps dramatically from the transmission side, the emitted signal from the low smoke temperatures very much takes over the scene. Its sensitivity to the lower smoke temperatures is also seen in the calibration section results. From the calibration study, any temperature around 265°C or above would saturate the sensor and all signals would be saturated. The VIS band in this case would be the next choice followed by the LWIR. A note about these two bands is that the mass of smoke (as seen in wildfires) may not have been enough to see more effects in the VIS, but since it the VIS still cannot view the concerning lower temperatures in forest fires, it is disregarded.

To emphasize the results for both the radiometric model and the calibrated smoke contrast imagery, an image of a Gazebo during a controlled burn is shown in Figure 13. Aerial imagery from VIS, SWIR and LWIR sensors flown on a DJI Matrice are shown. The time-synced imagery was taken during one of the most intense moments of a controlled burn in Tucson. AZ. Unfortunately, the eSWIR sensor is too heavy to fly on any drones so its imagery did not get taken. However, the image highlights the results in a real-world application of the situational awareness system in an extreme setting.
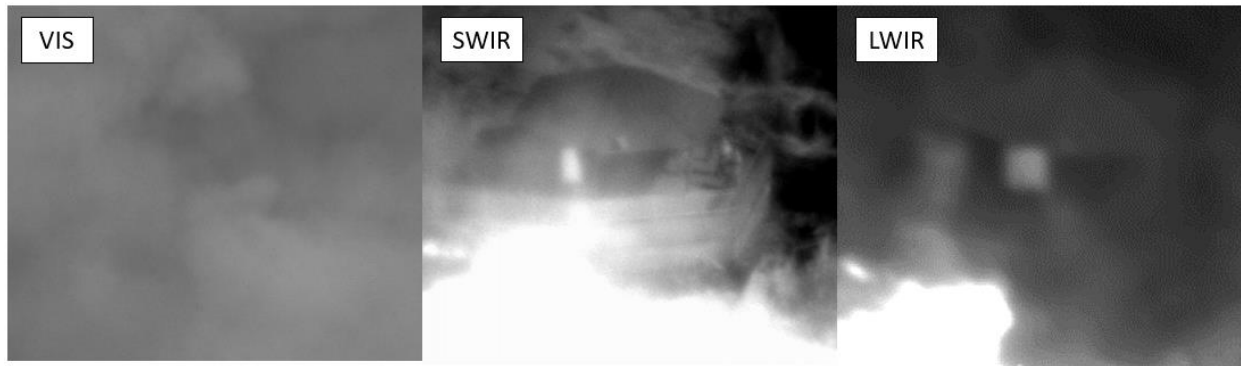
Figure 6.13: Imagery of a controlled burn taken from a DJI Matrice. The VIS, SWIR and LWIR imagery are time synced. The digital crop is over the same space containing the gazebo. The controlled burn was performed by the Tucson Fire Department.

As shown in the imagery, the concentration of the smoke is too high in the VIS to see any detail of the scene. Any firefighters within this scene would be lost in the smoke and there is no fire boundary information in the band. Their position would be completely lost, and no real time location imagery could be relayed. In the LWIR band, the gazebo details start to appear, but the smoke path radiance is still obscuring the view. Alongside that, the dynamic range of the uncooled microbolometer is vastly stretched due to the large range in temperatures. The contrast is also degraded in this manner. The SWIR band has a maintains good contrast in the presence of the heavy smoke concentration and strong emitted smoke signal radiance. Even with both effects clearly, the detail of the gazebo, fence, and even firefighters on the ledge can be seen in the SWIR. The boundary of the fire just below the fence is also easily noticeable and that information could be relayed to the forest firefighters in the area if it started to encroach on them too quickly. The SWIR band gives great contrast for situational awareness in these extreme conditions.

6.11) Conclusion

The contrast of a scene when smoke was present is studied for the VIS, SWIR, eSWIR and LWIR bands. Maintaining good contrast of a scene during a wildfire setting is important for situational awareness. The ability to view firefighters, terrain and the fire boundary in extreme conditions is needed to create a reliable imaging system designed to help keep forest firefighters safe. A radiometric model, high-temperature calibration technique and smoke contrast field experiment were used to compare the performance of each band. Radiometrically calibrated scenes measured the standard deviation of contrast for each band to show which ones were more dependable during close encounters with fire and smoke.

For imagers focused on viewing the ambient scene for situational awareness, it is found that SWIR maintains the highest contrast out of all the bands. The SWIR contrast deviated the least when high concentrations of hot smoke were present. The VIS band, as expected, was highly affected by the transmission of the signal through smoke. The LWIR and eSWIR band contrast were both degraded mostly due to the emitted smoke signal radiance coming from the lower smoke temperatures rising above the flames. Due to their ability to detect lower blackbody equivalent temperatures, targets became obscured more often in the eSWIR and LWIR than the SWIR even with their longer wavelengths helping with transmission from scattering. The SWIR, however, can still detect the boundaries of fire, but isn't as sensitive to the lower smoke temperatures obscuring the view of forest firefighters in the field.

Chapter 7: General Discussion

7.1) Overview

The previous chapters highlight how the theoretical design of imagers and their integration onto aerial platforms leads to successful imaging systems. When flying sensors, all factors such as sensor design, available illumination, degrading environmental factors, and the platform itself must be carefully considered. The camera system's spectral range, sensitivity, and resolution should be chosen to match the available light, required contrast, and target size to optimize the performance for the imaging task at hand. These considerations become particularly crucial during flight, where airborne dynamics can induce blur. Leveraging specific wavebands for imaging tasks can significantly enhance system performance. Without the limitation of SWaP, any band can be accommodated onto an sUAS. However, a direct comparison of the VIS, NIR, SWIR, eSWIR, MWIR, and LWIR cannot determine the most advantageous band for the aerial imaging task.

7.2) Urban and Rural Mapping

As shown in chapter 3, a sensor's spectral range measuring a scene can greatly impact the performance of the sensor system. Equivalent reflectivity is a valid metric to compare the four reflective bands together, as seen throughout this dissertation. Integration times required to view a typical solar irradiance scene for mapping purposes have essentially no emitted light in each of the reflective bands (Table 2.1). This means that the imagers only receive reflected radiance provided by the solar illumination of that day. The reason that solar irradiance or photons per second in each band were not used to compare the bands is due to the substantial differences in

the available light (Table 2.1), which would skew the results of the variance and power spectral densities (PSDs) comparison. Since the VIS band would have a much larger range of reflected radiance in a scene, the variance would seem much larger in that band than in the others.

Equivalent Reflectivity is an intrinsic property to each material present in the scene. The reflectivity of objects can vary greatly between the different bands. As shown in equation 2.7, equivalent reflectivity is a normalized comparison for the reflective bands between 0 and 1, proving the emitted signal does not contribute to the scene. The contrast of the reflective band imagery relies solely on the reflective properties of materials. By using equivalent reflectivity, it effectively normalizes the scenes in each band to a physical comparable quantity that puts each scene on the same scale, reducing the bias of the ratio of light available from solar illumination.

Both the variance of the equivalent reflectivity within a scene and the 1D PSDs show that the eSWIR has the highest contrast within urban and rural imagery. For a mapping system, the eSWIR reflective properties of the materials within a scene give it an inherent advantage and more contrast. Coupled with the eSWIR's ability to penetrate degraded visual environments more effectively, the extra cost of the imager may be warranted for higher performance. The next option would be a NIR imager that also has good contrast for mapping purposes. The reason that NIR might have more contrast could be coupled with its sensitivity to water present within the scene. The NIR would provide a much cheaper option and lower SWaP over eSWIR as well. The SWIR and VIS bands start to approach uniform high reflectivity and low reflectivity respectively. This is seen especially in Figures 3.6 – 3.8. The foliage of the rural scenes has little variation within the two bands. The decreased variation in equivalent reflectivity differences corresponds to decreased contrast between objects, making it more difficult to identify objects within a scene for mapping. For targeting, however, a target with a large reflectivity difference

from the uniform type of background in the VIS and SWIR would stand out easily with the low background clutter. Both human-aided and automated target recognition routines do not need to be as rigorous to find the objects of interest within the scene.

7.3) Nighttime Wire Detection

Typically, the emissive side of equation 2.7 dominates the MWIR and LWIR imagery. However, as seen in chapter 4, the high reflectivity of a metal surface in these two bands causes a large variation in a high-voltage wire's signal. For the MWIR and LWIR, the wire is now reflecting the cold sky path radiance when looking down and the warm ground background when looking up at the wire. The mathematical model derived in chapter 4 produced high-voltage line signatures that incorporated the warm ground, varying sky path radiance, reflectivity, emissivity, and BRDF and matches calibrated wire measurements. With the knowledge that the theoretical model matches calibrated measurements, the use of a passive high-voltage wire detection system can be modeled in any atmosphere around the globe.

The large distribution of reflected blackbody equivalent temperatures based on the sensor's viewing angle of the wire poses some solutions and problems. For strict aviation geometries, a MWIR or LWIR sensor that looks down at the wire will be able to maintain good contrast because of the cold wire temperatures against the warm earth background. Problems occur when the rotorcraft goes in for landing or begins to take-off. As the altitude of the aircraft approaches the same altitude of the high-voltage line, the wire starts reflecting more of the warm ground until at some point the contrast between the wire and its background goes to zero. Unfortunately, the angle that does not have any contrast with the wire is approximately when the

sensor is looking at the horizon. The reason is due to the rapidly increasing sky path radiance as the sensor's angle moves towards the horizon. This is a dangerous altitude to fly at for these reasons but is necessary for most rotorcrafts for landing or picking up troops. For a single MWIR or LWIR sensor, this poses problems for a passive high voltage wire detection system.

Luckily the MWIR and LWIR bands have zero contrast at two different angles. The low SWaP of both these sensors could allow for two to be flown at the same time. Another option would be to use a dual-color focal plane. The technology has advanced for these two bands where both bands can be imaged onto the same sensor. By viewing the scene in each band, the wire contrast could be maintained in one band while the other has no contrast. Then the image could switch back to the other band when it knows that the zero-contrast angle is coming. This would help the pilot view the wire at all times either passively or actively to aid in one of the deadliest crashes that still occurs today.

7.4) Wide Area Coverage

The SWaP of all sensor bands has lowered so much that multiple camera systems can be flown at the same time. Using multiple sensors to expand a system's overall FOV maintains high resolution over large distances. This method has proven to work in the targeting case over very large FOV single sensors. A direct comparison of multi-camera to gimballed sensors still needs to be performed. However, the lack of moving components helps to minimize the opportunity for parts breaking and the staring multi-camera array can capture at high frame rates without moving the gimbal around and losing some information about a scene. The staring multi-camera array systems provide the opportunity for further computational techniques to increase resolution as

well instead of using the processing power control the gimbal and stitch the imagery from the gimbal together.

The modified TTP approach proved successful for designing targeting based multi-camera systems. The resolution constraining each sensor's FOV from the TTP metric provided high performance throughout the entire large multi-camera FOV ground swath. This design approach considers the unique performance of each waveband imager and designs multi-camera systems for any of the bands described above. The figure of merit produced can be used effectively to compare the performance of multi-camera systems in good and degraded visual environments. This novel quantitative approach can be used in other design processes to aid in band comparison trade studies. The next step in quantifying the performance for the multi-camera systems is to use the figure of merit to show the effects of platform dynamics during flight. The difference between integration time and time constant for the different imagers needs to be considered when designing these systems for targeting applications.

This design method is not only applicable to targeting but can be reused for other multi-system design approaches. For mapping, to decrease the time of flight for the drone and maintain good resolution over a large area, the multi-camera FOV expansion approached can be used. For wire detection, many narrow FOV sensors could be used to increase the range at which a wire can first be detected with an overall large FOV. For any applications the increased FOV with high resolution can be easily obtained with the low SWaP of current sensors available.

7.5) Wildfire Situational Awareness

As seen in chapters 3-5, the effect of reflectivity and emissivity play a huge role in system performance. Normally the reflective and emissive band designs and radiometry involved focus on their typical sources. In a scene that has a huge variation of physical temperatures, this is no longer the case. The VIS, SWIR, and eSWIR sensor design now needs to consider the emissive effects of fire and smoke. The temperatures and smoke concentration experienced in a wildfire environment highly effect the contrast needed for situational awareness to keep forest firefighters safe.

The typical design technique of increasing wavelength to decrease scattering from particles present in the atmosphere cannot be used. The effect of blackbody radiation in the longer wavelengths takes over and the decreases contrast from the smokes emitted light. The radiometric model and calibrated measurements show that a middle ground has the best opportunity to maintain line of sight between an airborne sensor and the firefighters in the field. The SWIR can image the terrain, personnel, roads, and fire boundary to increase situational awareness and help the efficacy of wildfire mitigation.

The radiometric model that contains both the reflective and emissive components of a scene produced results that the SWIR band is able to maintain good contrast for both high concentrations of smoke and high temperature smoke signal radiance. The LWIR and eSWIR contrast reduced rapidly with the emissive smoke signal and little due to the smoke concentrations expected in wildfire situations. As expected, the VIS band is mainly dependent on the concentration of smoke with little dependency on smoke temperature. The radiometric model contrast results were supported by the calibrated fire and smoke contrast measurements performed where SWIR contrast was affected the least. The wavelength of the SWIR band

allows for the imager to see the fire boundary but not be limited by the decreasing smoke temperature as it rises.

High resolution is needed while covering a large area and the wide area coverage multi-camera system design approach can be utilized. A system created for forest firefighters in this manner could be SWIR only, or a multi-spectral approach. The SWIR is needed to maintain the line of sight of the Hot Shots but other wavelengths for a multi-camera design offer other information. The VIS could be used to track the smoke direct in real time. This helps predict the unexpected weather changes that are typically the deadly part of wildfire mitigation. Since the SIWR cannot detect temperatures below 300°C while viewing an ambient scene, an LWIR detector could be added to relay colder fire signatures to the firefighters.

Chapter 8: Conclusion

The integration of infrared systems on aerial platforms enhances the effectiveness of both technologies. As infrared cameras technology becomes lower in SWaP, and as sUAS improve flight longevity and payload capacity, previous limitations hindering their integration are no longer a concern. The novel applications from these advancements open a new era in sensor design. Ground-based techniques traditionally used for designing infrared systems area adapted to suit the unique geometries of aerial platforms. This dissertation demonstrates that mapping, pilotage, targeting, and situational awareness systems can be successfully developed using these modified design approaches. It is shown in this dissertation that mapping, pilotage, targeting, and situational awareness systems can be designed with these novel modified design approaches. The radiometric models produced accurately represent various scenarios and match calibrated measurement results.

By considering all signals within a scene, both in theory and through field testing, sensor systems with high performance can be achieved. Leveraging spectral differences in the infrared bands enables the creation of more effective targeting and mapping systems. High background clutter provides valuable information for mapping algorithms to identify objects and aid user orientation, while low background clutter improves targeting performance by reducing false alarms. Additionally, combining different infrared bands can enhance imager performance. The combination of typical infrared bands can increase the contrast of high voltage wire detection over single band imagers.

Typical sources of reflective and emissive bands and their modeling may not apply under altered illumination conditions. In wildfire environments, maintaining good contrast is crucial for

providing forest firefighters with situational awareness to ensure their safety. The VIS band becomes easily obscured by smoke concentration and the LWIR contrast decreases due to the emission of the hot smoke, despite its longer wavelength compared to smoke particles. In this case, the SWIR band provides the utility of imaging the fire boundary, firefighter locations and terrain with minimal contrast loss.

For mapping, targeting, pilotage, or situational awareness, high resolution plays a pivotal role in system performance. To expand the FOV without sacrificing resolution, multi-camera system expands the capabilities of typical single sensors systems. The multiple sensors varying FOVs maintain resolution even as range increases, ensuring robust performance across diverse operational scenarios.

References

References for Chapter 1

1. Lockheed Martin. "Arrowhead (M-TADS/PNVS)." Retrieved January 29, 2024, from https://www.lockheedmartin.com/en-us/products/apache-sensors.html.

2. Rogalski, A. "History of Infrared Detectors." Opto-electronics Review, vol. 20, no. 3, 2012, pp. 279-308. Web.

3. Sony. "SWIR image sensor." White Paper. Accessed April 2, 2023, from https://www.sony-semicon.com/files/62/flyer_industry/IMX990_991_Flyer_en.pdf.

4. Shafer, T., et al. "High Operating Temperature (HOT) Midwave Infrared (MWIR) 6 μm Pitch Camera Core Performance and Maturity." Proceedings of SPIE, vol. 12107, 2022, pp. 121070V-21070V-15. Web.

5. Yuan, H., et al. "Recent Progress in Extended Wavelength InGaAs Photodetectors and Comparison with SWIR HgCdTe Photodetectors." Proceedings of SPIE, vol. 11129, 2019, pp. 111290E-11290E-10. Web.

6. Wiley, L., et al. "Target discrimination in the extended shortwave infrared band (2 to 2.5μm) compared with visible, near-infrared, and SWIR in degraded visual environments." Opt. Eng., vol. 61, no. 11, 2022, article 113103.

7. MacDougal, M., et al. "Thermoelectrically-cooled extended-SWIR FPAs using unipolar barrier detectors." Proceedings of SPIE, vol. 10624, 2018, article 1062402.

8. Borengasser, Marcus, et al. Hyperspectral Remote Sensing: Principles and Applications. CRC Press, 2007.

9. Driggers, R., et al. Introduction to Infrared and Electro-Optical Systems, Second Edition. 2nd ed., Artech House, 2012.

10. Vollmerhausen, R.H., and Bui, T. "Using a targeting metric to predict the utility of an EO imager as a pilotage aid." Proceedings of SPIE, vol. 6207, 2006, article 62070C.

11. Jordan, S., et al. "Comparison of scene contrast temperature in mid-wave infrared and long-wave infrared." Opt. Eng., vol. 62, no. 11, 2023, article 113107.

12. Hodgkin, V.A., and Driggers, R.G. 3rd Generation Thermal Imager Sensor Performance. 2006.

13. WHIO Staff. "Pilot Dead After Helicopter Crashes While Spraying Crops in Clark County; NTSB Investigating." Cox Media Group, 2023. Accessed January 29, 2024.

14. Casiano, L. "Army Helicopter Crashes Into Power Lines in Washington State, Makes 'Hard Landing'." Fox News, September 29, 2023. Accessed January 29, 2024.

15. Vollmerhausen, R.H., et al. "New Metric for Predicting Target Acquisition Performance." Optical Engineering, vol. 43, no. 11, 2004, pp. 2806-2818.

16. Vizgaitis, J. "Third generation infrared optics." Proceedings of SPIE, vol. 6940, 2008, article 69400S.

17. Wiley, L., et al. "Comparison of reflective band (Vis, NIR, SWIR, eSWIR) performance in daytime reduced illumination conditions." Appl. Opt., vol. 62, 2023, pp. 8316-8326.

18. Mohsin, B., et al. "An Innovative System to Enhance Situational Awareness in Disaster Response." Journal of Homeland Security and Emergency Management, vol. 13, no. 3, 2016, pp. 301-327.

19. Nadal-Serrano, J.M., and Lopez-Vallejo, M. "A Time-Resolved Monte Carlo Smoke Model for Use at Optical and Infrared Frequencies." Fire Safety Journal, vol. 71, 2015, pp. 299-309.

20. Driggers, R.G., Hodgkin, V., and Vollmerhausen, R. "What Good Is SWIR? Passive Day Comparison of VIS, NIR, and SWIR." Proceedings of SPIE, vol. 8706, 2013, article 87060L-87060L,15.

References for Chapter 2

1. Berk, A., et al. "MODTRAN6: a major upgrade of the MODTRAN radiative transfer code." Proceedings of SPIE, vol. 9088, 2014, article 90880H. doi:10.1117/12.2050433.

2. Nichols, J., R. Driggers, and M. Friedman. Introduction to Infrared and Electro-Optical Systems, Second Edition. 2nd ed., Artech House, 2012.

3. Pinson, L. Electro-Optics. New York City, NY: Wiley, 1985.

4. Driggers, R., et al. "Burmese python target reflectivity compared to natural Florida foliage background reflectivity." Appl. Opt., vol. 58, 2019, pp. D98-D104.

5. Georgiev, G.T., and J.J. Butler. "Progress in BRDF calibration measurements in the SWIR." Proceedings of SPIE, vol. 7452, 2009, article 745205. doi:10.1117/12.827356.

6. Höfer, S., B. Jan, and M. Heizmann. "Infrared deflectometry for the inspection of diffusely specular surfaces." Advanced Optical Technologies, vol. 5, no. 5-6, 2016, pp. 377-387. doi:10.1515/aot-2016-0051.

7. Li, N., et al. "Removal of reflections in LWIR image with polarization characteristics." Opt. Express, vol. 26, 2018, pp. 16488-16504.

8. Adler-Golden, S.M., et al. "Long-wave infrared surface reflectance spectra retrieved from Telops Hyper-Cam imagery." Proceedings of SPIE, vol. 9088, 2014, article 90880U. doi:10.1117/12.2050446.

9. Vollmerhausen, R.H., and T. Bui. "Using a targeting metric to predict the utility of an EO imager as a pilotage aid." Infrared Imaging Systems: Design, Analysis, Modeling, and Testing XVII. Proceedings of SPIE, vol. 6207, 2006.

10. Michael, P.R., D.E. Johnston, and W. Moreno. "A conversion guide: solar irradiance and lux illuminance." Journal of Measurements in Engineering, vol. 8, no. 4, 2020, pp. 153–166. doi:10.21595/jme.2020.21667.

11. Haefner, D.P. "MTF measurements, identifying bias, and estimating uncertainty." Proceedings of SPIE, vol. 10625, 2018, article 1062506. doi:10.1117/12.2303974.

12. Teaney, B.P., and D.P. Haefner. "Evaluating the performance of an IR imaging system: a tutorial." Proceedings of SPIE, vol. 10625, 2018, article 106250K. doi:10.1117/12.2303975.

13. Claxton, C.D., and R.C. Staunton. "Measurement of the point-spread function of a noisy imaging system." J. Opt. Soc. Am. A, vol. 25, 2008, pp. 159-170.

14. Gaskill, J.D. Linear Systems, Fourier Transforms, and Optics. New York: Wiley, 1978.

15. Vollmerhausen, Richard H, Eddie Jacobs, and Ronald G Driggers. "New Metric for Predicting Target Acquisition Performance." *Optical Engineering* 43.11 (2004): 2806-2818. Print.

16. Barten, P.G.J. "Evaluation of the effect of noise on subjective image quality." Proceedings of SPIE, vol. 1453, 1991. doi:10.1117/12.44340.

17. Preece, B., et al. "Improved noise model for the US Army sensor performance metric." Proceedings of SPIE, vol. 8014, 2011.

18. Wiley, L., et al. "Target discrimination in the extended shortwave infrared band (2 to 2.5μm) compared with visible, near-infrared, and SWIR in degraded visual

environments." Opt. Eng., vol. 61, no. 11, 2022, article 113103.

doi:10.1117/1.OE.61.11.113103.

19. Driggers, R.G., et al. "What good is SWIR? Passive day comparison of VIS, NIR, and

SWIR." Proceedings of SPIE, vol. 8706, 2013, article 87060L. doi:10.1117/12.2016467.

20. Modeling & Simulation Division. Night Vision Thermal Imaging Systems Performance

Model User's Manual & Reference Guide. U.S Army Night Vision and Electronic

Sensors Directorate, 2001.

21. Suo-Anttila, J., et al. "An Evaluation of Actual and Simulated Smoke Properties." Fire

and Materials, vol. 29, no. 2, 2005, pp. 91-107.

22. United States. Army Materiel Systems Analysis Activity, Joint Technical Coordinating

Group for Munitions Effectiveness, Smoke and Aerosol Working Group. Smoke and

Natural Aerosol parameters (SNAP) Manual. U.S. Army Materiel Systems Analysis

Activity, 1985.

References for Chapter 3

1. Dupuis, Julia R., et al. "High speed VNIR/SWIR HSI sensor for vegetation trait

mapping." Proc. SPIE 10986, Algorithms, Technologies, and Applications for

Multispectral and Hyperspectral Imagery XXV, 14 May 2019, article 109861F.

doi:10.1117/12.2518114.

2. Roberts, J., et al. "Mobile Terrestrial Photogrammetry for Street Tree Mapping and

Measurements." Forests, vol. 10, no. 8, 2019, article 701. doi:10.3390/f10080701.

3. Hewitt, Jennifer, et al. "Sensor optimization of camera direction for time-limited search performance." Proc. SPIE 12106, Infrared Imaging Systems: Design, Analysis, Modeling, and Testing XXXIII, 27 May 2022, article 1210604. doi:10.1117/12.2618124.

4. Kirsch, M., et al. "Integration of Terrestrial and Drone-Borne Hyperspectral and Photogrammetric Sensing Methods for Exploration Mapping and Mining Monitoring." Remote Sensing, vol. 10, no. 9, 2018, article 1366. doi:10.3390/rs10091366.

5. Wiley, Lindsey, et al. "Target discrimination in the extended SWIR (eSWIR) band (2-2.5μm) compared to Vis, NIR, and SWIR in degraded visual environments." Proc. SPIE 12106, Infrared Imaging Systems: Design, Analysis, Modeling, and Testing XXXIII, 27 May 2022, article 1210606. doi:10.1117/12.2618566.

6. Mares, J., et al. "Vehicle self-localization in GPS-denied zones by multi-band imaging and analysis of prominent scene features." Proc. SPIE 12534, Infrared Technology and Applications XLIX, 13 June 2023, article 125341P. doi:10.1117/12.2663660.

7. Irwin, A., et al. "Vehicle testbed for multispectral imaging and vision-based geolocation." Proc. SPIE 12534, Infrared Technology and Applications XLIX, 13 June 2023, article 125341O. doi:10.1117/12.2663734.

8. Huntington, Jonathan F. "The Role of Remote Sensing in Finding Hydrothermal Mineral Deposits on Earth." Ciba Foundation Symposium 202 - Evolution of Hydrothermal Ecosystems on Earth (And Mars?), John Wiley & Sons, 2007, pp. 214-235.

9. Vollmerhausen, Richard H., Eddie Jacobs, and Ronald G. Driggers. "New Metric for Predicting Target Acquisition Performance." Optical Engineering, vol. 43, no. 11, 2004, pp. 2806-2818.

10. Driggers, Ronald G., et al. "What good is SWIR? Passive day comparison of VIS, NIR, and SWIR." Proc. SPIE 8706, Infrared Imaging Systems: Design, Analysis, Modeling, and Testing XXIV, 10 June 2013, article 87060L. doi:10.1117/12.2016467.

11. McIntosh, B., et al. "Infrared Target Detection in Cluttered Environments by Maximization of a Target to Clutter Ratio (TCR) Metric Using a Convolutional Neural Network." IEEE Transactions on Aerospace and Electronic Systems, vol. 57, no. 1, Feb. 2021, pp. 485-496. doi:10.1109/TAES.2020.3024391.

12. Qin, Y., and B. Li. "Effective Infrared Small Target Detection Utilizing a Novel Local Contrast Method." IEEE Geoscience and Remote Sensing Letters, vol. 13, no. 12, Dec. 2016, pp. 1890-1894. doi:10.1109/LGRS.2016.2616416.

13. Stotts, Larry B., and Lawrence E. Hoff. "Statistical detection of resolved targets in background clutter using optical/infrared imagery." Appl. Opt., vol. 53, 2014, pp. 5042-5052.

14. Akasheh, O.Z., et al. "Detailed mapping of riparian vegetation in the middle Rio Grande River using high resolution multi-spectral airborne remote sensing." Journal of Arid Environments, vol. 72, no. 9, 2008, pp. 1734-1744. Doi

15. Han, Zonghao, et al. "Aerial Visible-to-Infrared Image Translation: Dataset, Evaluation, and Baseline." Journal of Remote Sensing, vol. 3, 2023, pp. 0096. DOI: 10.34133/remotesensing.0096.

16. McCrea, R. "The Yarnell Hill Fire: A Review of Lessons Learned." International Association of Wildland Fire, June 2014. Accessed 22 Mar. 2023. Web. https://www.iawfonline.org/article/the-yarnell-hill-fire-a-review-of-lessons-learned/.

17. Driggers, Ronald G., et al. Introduction to Infrared and Electro-Optical Systems. Artech House, 2012. ProQuest Ebook Central, https://ebookcentral.proquest.com/lib/uaz/detail.action?docID=1118871.

18. Haefner, David P. "MTF measurements, identifying bias, and estimating uncertainty." Proceedings of SPIE, vol. 10625, 26 April 2018, pp. 1062506. DOI: 10.1117/12.2303974.

19. Holst, Gerald C. "Imaging System Performance Based upon Fλ/d." Optical Engineering, vol. 46, no. 10, 2007, pp. 103204. Web.

20. Schmidt, Luke M., et al. "Reflectivity Characterization of Various Black and White Materials." 12188, 2022, pp. 121884W-121884W-7. Web.

21. Wiley, Lindsey, et al. "Target Discrimination in the Extended Shortwave Infrared Band (2 to 2.5μm) Compared with Visible, Near-infrared, and SWIR in Degraded Visual Environments." Optical Engineering, vol. 61, no. 11, 2022, pp. 113103. Web.

References for Chapter 4.

1. Nagaraj, Vengalattore T. "Safety Study of Wire Strike Devices Installed on Civil and Military Helicopters." Google Books, Office of Aviation Research and Development, Federal Aviation Administration, Sept. 2008.

2. Chandrasekaran, R., et al. "Helicopter wire strike protection and prevention devices: review, challenges, and recommendations." Aero. Sci. Technol., vol. 98, 2020, p. 16.

3. King, Donald F., et al. "3rd-generation MW/LWIR sensor engine for advanced tactical systems." Proc. SPIE 6940, Infrared Technology and Applications XXXIV, 22 April 2008, article 69402R.

4. Goldberg, Arnold C., et al. "Dual-band QWIP MWIR/LWIR focal plane array test results." Proc. SPIE 4028, Infrared Detectors and Focal Plane Arrays VI, 17 July 2000.

5. Vollmerhausen, Richard H. "Design criteria for helicopter night pilotage sensors." Proc. SPIE 2075, Passive Sensors, 29 January 1992, article 20750Q. doi:10.1117/12.2300254.

6. Rogalski, Antoni, and K. Chrzanowski. "Infrared Devices And Techniques (Revision)." Metrology and Measurement Systems, vol. 21, 2014, pp. 10-2478/mms-2014-0057.

7. John M. Evans LLC. "Standards of Visual Acuity." Intelligent Systems Division, National Institute for Standards and Technology, June 15, 2006, https://www.nist.gov/system/files/documents/el/isd/ks/Visual_Acuity_Standards_1.pdf.

8. Barten, Peter G. J. Contrast Sensitivity of the Human Eye and Its Effects on Image Quality. Bellingham, Wash.: SPIE Optical Engineering, 1999.

9. Vollmerhausen, Richard H., and Trang Bui. "Using a targeting metric to predict the utility of an EO imager as a pilotage aid." Proc. SPIE 6207, Infrared Imaging Systems: Design, Analysis, Modeling, and Testing XVII, 15 May 2006, article 62070C. doi:10.1117/12.668436.

10. Jalil, Bushra, et al. "Fault Detection in Power Equipment via an Unmanned Aerial System Using Multi Modal Data." Sensors (Basel, Switzerland), vol. 19, no. 13, 2019, article 3014.

11. Jakob, Wenzel, et al. Physically Based Rendering: From Theory to Implementation. Netherlands, Elsevier Science, 2016, Federal Aviation Administration, Sept. 2008.

12. Zeljković, Milan, et al. "THE DETERMINATION OF THE EMISSIVITY OF ALUMINUM ALLOY AW 6082 USING INFRARED THERMOGRAPHY." Journal of Production Engineering, vol. 18, 2015, pp. 23-26.

13. Crow, Mariesa L., and Nirup Shetty. "Electric Power Measurements and Variables." Encyclopedia of Energy, edited by Cutler J. Cleveland, Elsevier, 2004, pp. 245-254. DOI:10.1016/B0-12-176480-X/00507-6.

References for Chapter 5.

1. Teledyne Lumenera. "Using a Single Versus Multiple Cameras in Aerial Imaging." White Paper, 2022. https://www.lumenera.com/media/wysiwyg/documents/casestudies/Using_Single_vs_Multi_Cameras_in_Aerial_Imaging-White_Paper.pdf. Accessed 27 Feb. 2023.

2. Huang, S., Teo, R.S.H., Leong, W.W.L. "Multi-Camera Networks for Coverage Control of Drones." Drones, vol. 6, 2022, p. 67. https://doi.org/10.3390/drones6030067.

3. Revello, C., Driggers, R., Brady, D., & Renshaw, K. "Large area coverage using drone mounted multi-camera systems." In G. C. Holst & D. P. Haefner (Eds.), Infrared Imaging Systems: Design, Analysis, Modeling, and Testing XXXIII (Proceedings of SPIE - The International Society for Optical Engineering; Vol. 12106), 2022, article 1210608. SPIE. https://doi.org/10.1117/12.2618708. Accessed 27 Feb. 2023.

4. Vollmerhausen, R., & Jacobs, E. "The Targeting and Task Performance (TTP) Metric: A New Model for Predicting Target Acquisition Performance." Center for Night Vision and Electro-Optics, Fort Belvoir, VA.

5. Driggers, R.G., Friedman, M.H., & Nichols, J.M. Introduction to Infrared and Electro-Optical Systems, 2nd ed., Artech House, 2012, Chapter 3, Section 3.8.

6. Maver, L.A., Erdman, C.D., & Riehl, K. "Imagery Interpretability Rating Scales." Itek Optical Systems, Lexington, MA, 16 Jan. 1998.

7. Johnson, J. "Analysis of Image Forming Systems." Image Intensifier Symposium, Warfare Electrical Engineering Department, U.S. Army Research and Development Laboratories, Ft. Belvoir, VA, 1958, pp. 244–273.

References for Chapter 6.

1. United States Environmental Protection Agency. "Climate Change Indicators: Wildfires." Accessed 19 Mar. 2023. https://www.epa.gov/climate-indicators/climate-change-indicators-wildfires.

2. MacCarthy, J., Tyukavina, S., Weisse, M., & Harris, N. "New Data Confirms: Forest Fires Are Getting Worse." World Resources Institute, 17 Aug. 2022. Accessed 19 Mar. 2023. https://www.wri.org/insights/global-trends-forest-fires.

3. Hoover, K., & Hanson, L. "Wildfire Statistics." Congressional Research Service, IF10244 – Version 66, 1 Mar. 2023. Accessed 19 Mar. 2023. https://sgp.fas.org/crs/misc/IF10244.pdf.

4. National Interagency Fire Center. "Wildfire Investigation: Coming Wildfire Causes." Accessed 19 Mar. 2023. https://www.nifc.gov/fire-information/fire-prevention-education-mitigation/wildfire-investigation.

5. Vaisala. "Vaisala's National Lightning Detection Network® (NLDN®)." Ref. B212165EN-C. Accessed 21 Mar. 2023. https://www.vaisala.com/sites/default/files/documents/WEA-MET-ProductSpotlight-NLDN-B212165EN-B.pdf.

6. Yanan, Z., Stock, M., Lapierre, J., & DiGangi, E. "Upgrades of the Earth Networks Total Lightning Network in 2021." Remote Sensing (Basel, Switzerland), vol. 14, no. 9, 2022, p. 2209. https://www.mdpi.com/2072-4292/14/9/2209.

7. Wang, A., & Lee, J. "NASA Data on Plant 'Sweating' Cloud Help Predict Wildfire Severity." Jet Propulsion Laboratory, California Institute of Technology, 4 Aug. 2022. Accessed 22 Mar. 2023. https://www.jpl.nasa.gov/news/nasa-data-on-plant-sweating-could-help-predict-wildfire-severity.

8. Pfell, R. "Wildland Firefighters Use Satellites, Infrared to Track Smoke, Lightning Strikes." Government Technology, Mail Tribune, Medford OR, 19 Jul. 2015. Accessed 21 Mar. 2023. https://www.govtech.com/em/disaster/wildland-firefighters-use-satellites-infrared-to-track-smoke-lightning-strikes.html.

9. Ban, Y., Zhang, P., & Nascetti, A. "Near Real-Time Wildfire Progression Monitoring with Sentinel-1 SAR Time Series and Deep Learning." Sci Rep, vol. 10, 2020, p. 1322. https://doi.org/10.1038/s41598-019-56967-x.

10. Jang, E., Kang, Y., Im, J., Lee, D-W., Yoon, J., & Kim, S-K. "Detection and Monitoring of Forest Fires Using Himawari-8 Geostationary Satellite Data in South Korea." Remote Sensing, vol. 11, no. 3, 2019, p. 271. https://doi.org/10.3390/rs11030271.

11. Schmidt, C., Hoffman, J., Prins, E., & Linstrom, S. "GOES-R Advanced Baseline Imager (ABI) Algorithm Theoretical Basis Document For Fire / Hot Spot Characterization." NOAA NESDIS, Center for Satellite Applications and Research, 30 Jul. 2012. Accessed 23 Mar. 2023. https://www.star.nesdis.noaa.gov/goesr/docs/ATBD/Fire.pdf.

12. Namburu, A., Prabha, S., Senthilkumar, M., Sumathi, R., & Elsayed, T. "Forest Fire Identification in UAV Imagery Using X-MobileNet." Electronics (Basel), vol. 12, no. 3, 2023, p. 733.

13. Akhloufi, M.A., Couturier, A., & Castro, N.A. "Unmanned Aerial Vehicles for Wildland Fires: Sensing, Perception, Cooperation and Assistance." Drones, vol. 5, no. 1, 2021, p. 15. https://doi.org/10.3390/drones5010015.

14. Avitt, A. "Mechanized Birds: Wildland Firefighting with Drone Intelligence." Forest Service, U.S. Department of Agriculture, 3 Oct. 2022. Accessed 23 Mar. 2023. https://www.fs.usda.gov/features/mechanized-birds-wildland-firefighting-drone-intelligence.

15. National Institute for Occupational Safety and Health. "Fighting Wildfires." Centers for Disease Control and Prevention, 7 Apr. 2022. Accessed 22 Mar. 2023. https://www.cdc.gov/niosh/topics/firefighting/default.html#print.

16. Forest Service. "Hotshots, These handcrews can really take the heat!" U.S. Department of Agriculture. Accessed 22 Mar. 2023. https://www.fs.usda.gov/science-technology/fire/people/hotshots.

17. Corrado, B. "8 Years Later, Arizona remembers 19 Granite Mountain Hotshots who died in Yarnell Hill Fire." Hox 10 Phoenix, 30 Jun. 2021. Accessed 22 Mar. 2023. https://www.fox10phoenix.com/news/gov-ducey-honors-19-granite-mountain-hotshots-who-died-in-yarnell-hill-fire-memorial-officially-dedicated.

18. McCrea, R. "The Yarnell Hill Fire: A Review of Lessons Learned." International Association of Wildland Fire, Jun. 2014. Accessed 22 Mar. 2023. https://www.iawfonline.org/article/the-yarnell-hill-fire-a-review-of-lessons-learned/.

19. Deshmukh, A., Casali, J., Lancaster, J., Bryner, N., & McLane, R. "Thermal Exposure Sensor for Fire Fighters: Laboratory-scale Performance Experiments." 2016. NIST Technical Note, 1803. https://www.govinfo.gov/content/pkg/GOVPUB-C13-1cbe443b67d4cd00b84fe731c259f62e/pdf/GOVPUB-C13-1cbe443b67d4cd00b84fe731c259f62e.pdf.

20. WO-FAM-Operations. "Fire Imaging Technologies for Wildland Fire Operations, User Guide." USDA Forest Service, 12 Feb. 2020. Accessed 24 Mar. 2023. https://fsapps.nwcg.gov/nirops/docs/upload/Fire_Imaging_Technologies_Users_G

21. Santoni, P. A., Simeoni, A., Rossi, J. L., Bosseur, F., Morandini, F., Silvani, X., Balbi, J. H., Cancellieri, D., & Rossi, L. "Instrumentation of Wildland Fire: Characterization of a Fire Spreading Through a Mediterranean Shrub." Fire Safety Journal, vol. 41, no. 3, 2006, pp. 171-184. ISSN 0379-7112. DOI: https://doi.org/10.1016/j.firesaf.2005.11.010.

22. Driggers, R., Hodgkin, V., & Vollmerhausen, R. "What Good Is SWIR? Passive Day Comparison of VIS, NIR, and SWIR." Proceedings of SPIE, vol. 8706, 2013, pp. 87060L-87060L-15. Web.

23. Thunderhead Engineering Consultants. "Smoke Visibility and Obscuration." PyroSim Version 2020.1 Tutorial. Accessed 23 Jan. 2024. https://support.thunderheadeng.com/tutorials/pyrosim/smoke-visibility-obscuration/.

24. Weinert, D., Cleary, T., Mulholland, G., & Beever, P. "Light Scattering Characteristics and Size Distribution of Smoke and Nuisance Aerosols." Building and Fire Research Laboratory, National Institute of Standards and Technology (NIST). Accessed 27 Mar. 2023.

25. Berk, A., Conforti, P., Kennett, R., Perkins, T., Hawes, F., & van den Bosch, J. "MODTRAN6: A Major Upgrade of the MODTRAN Radiative Transfer Code." Proceedings of SPIE, vol. 9088, 2014, pp. 90880H. DOI: 10.1117/12.2050433.

26. Gabbert, B. "At What Temperature Does a Forest Fire Burn?" Wildfire Today, University of Utah, 26 Feb. 2011. Accessed 27 Mar. 2023. https://wildfiretoday.com/2011/02/26/at-what-temperature-does-a-forest-fire-burn/.

27. United States. Army Materiel Systems Analysis Activity, Joint Technical Coordinating Group for Munitions Effectiveness. "Smoke and Natural Aerosol Parameters (SNAP) Manual." U.S. Army Materiel Systems Analysis Activity, 1985.

28. Goodman, Joseph W., and Society of Photo-optical Instrumentation Engineers, Publisher. Speckle Phenomena in Optics: Theory and Applications. 2nd ed., 2020, SPIE Press Monograph; PM312. Web.

References for Chapter 7.

1. Knipling, Edward B. "Physical and Physiological Basis for the Reflectance of Visible and Near-Infrared Radiation from Vegetation." Remote Sensing of Environment, vol. 1, no. 3, 1970, pp. 155-159. Print.